Laser-induced strain as a functional tool in solids and nanostructures

Dissertation zur Erlangung des Doktorgrades an der Fakultät für Mathematik, Informatik und Naturwissenschaften Fachbereich Physik der Universität Hamburg

vorgelegt von
Roman Bauer

Hamburg
2023

Gutachter/innen der Dissertation:	Dr. Peter Gaal Prof. Dr. Robert Blick
Zusammensetzung der Prüfungskommission:	Prof. Dr. Daniela Pfannkuche Prof. Dr. Hans Peter Oepen Dr. Peter Gaal Prof. Dr. Robert Blick PD Dr. habil. Guido Meier
Vorsitzende/r der Prüfungskommission:	Prof. Dr. Daniela Pfannkuche
Datum der Disputation:	20.09.2023
Vorsitzender des Fach-Promotionsausschusses PHYSIK:	Prof. Dr. Günter H. W. Sigl
Leiter des Fachbereichs PHYSIK:	Prof. Dr. Wolfgang J. Parak
Dekan der Fakultät MIN:	Prof. Dr.-Ing. Norbert Ritter

Abstract

This thesis investigates applications of laser induced strain for creation, precise control and probing of surface deformations and their further applications. The applications include shortening and gating of X-ray pulses at synchrotron facilities, independent control of induced transient thermal grating and standing surface acoustic waves, measurement of periodic surface displacements with sub-angstrom precision, as well as an investigation of laser induced magnetization precession in thin ferromagnetic films. A prerequisite for developing strain-driven applications is the ability to generate and control localized lattice strain on short time- and lengthscales. This prerequisite is developed in this thesis.

The main tool for generating strain on short time- and lengthscales are ultrashort laser pulses capable of launching strain waves by means of a rapid expansion due to a sudden temperature rise. Periodic surface deformations are generated using the Transient Grating technique, which deploys overlapping laser beams, resulting in an interference pattern on the sample surface. It is used to generate surface deformations with 1.5 µm period and up to 5 nm surface excursion and control the deformations on sub nanosecond timescales using the Transient Grating technique.

This thesis is based on the research that resulted or contributed to the following publications: The experimental deployment and test of a new improved design of a laser-driven multilayered Bragg-switch at ESRF ID09. It allowed shortening of X-ray pulses from 100 ps to 10 ps with a repetition rate higher than 1 MHz and a low thermal background. The new experimental setup utilizing multiple subsequent transient grating excitation with an independent temporal and spatial phase control, opening a possibility for an independent control of periodic transient thermal surface deformations and induced surface acoustic waves. It was successfully deployed and tested at ESRF ID09 as well. The method based on mathematical modelling of periodic surface displacements and diffraction theory, allowing precise measurements of an absolute amplitude of periodic surface displacements. A study of excitation mechanisms of the magnetization precession in ferromagnetic thin films, which led to the exclusion of pure thermal excitation by means of a change of temperature dependent anisotropy contributions.

Zusammenfassung

Die vorliegende Arbeit beschäftigt sich mit der Frage nach Anwendungen der laserinduzierten Oberflächenverformungen als multifunktionale Werkzeuge in der Festkörperphysik. Die untersuchten Anwendungen beinhalten Verkürzung und Selektion der von Synchrotronquellen erzeugten Röntgenpulsen, unabhängige Kontrolle von induzierten Wärmegittern und stehenden akustischen Oberflächenwellen. Weitere Anwendungen sind das Verfahren zur Messung der Amplitude von periodischen Oberflächenverformungen mit einer Präzision besser als ein Ångström und Untersuchung von Anregungsmechanismus der Präzision der Magnetisierung in dünnen Filmen. Die Voraussetzung für die Entwicklung von solchen Werkzeugen ist eine Möglichkeit, die lokalisierten Oberflächenverformungen des Kristallgitters auf kurzen Zeit- und Längenskalen zu generieren und kontrollieren.

Das Hauptwerkzeug für die Erzeugung von Oberflächenverformungen eines Kristallgitters auf kurzen Zeit- und Längenskalen sind die ultrakurzen Laserpulse, die in der Lage sind, akustische Oberflächenwellen durch eine schnelle Expansion eines Kristallgitters zu erzeugen. Die periodischen Oberflächenverformungen können durch die Transient Grating (TG) Methode, bei der zwei Laserstrahlen an der Oberfläche eines Festkörpers interferieren, erzeugt werden. Mit der TG Methode wurden Oberflächenverformungen mit der Periode von 1,5 μm und einer Extrusion der Oberfläche von 5 nm erzeugt und auf Zeitskalen unterhalb einer Nanosekunde manipuliert.

Diese Arbeit ist das Ergebnis folgender Forschungsarbeit: ein experimenteller Aufbau und Test von neuartigen mehrschichtigen Bragg-Schaltern an ESRF ID09. Sie erlauben Röntgenpulse von 100 ps auf 10 ps mit einer Wiederholrate von über 1 MHz und einem geringen Wärmehintergrund zu verkürzen. Ein neuer experimenteller Aufbau, der mehrere nacheinander folgende TG-Anregungen verwendet, um eine unabhängige Kontrolle von akustischen Oberflächenwellen und dem statischen Wärmegitter zu ermöglichen. Dieser Aufbau war ebenfalls an ESRF ID09 getestet. Ein Verfahren, welches ein mathematisches Modell der periodischen Oberflächenverformungen und die Beugungstheorie verwendet, und dabei eine Messung der absoluten Amplitude der angeregten Oberflächenverformungen erlaubt. Eine Untersuchung der Anregungsmechanismen der ferromagnetischen Präzision in dünnen Pt/Co/Pt Filmen, welche eine Anregung allein durch die Änderung der Temperatur der Oberfläche ausschließt.

Publications included in this thesis

(I) Demonstration of a picosecond Bragg switch for hard X-rays in a synchrotron-based pump–probe experiment
M. Sander, R. Bauer, V. Kabanova, M. Levantino, M. Wulff, D. Pfuetzenreuter, J. Schwarzkopf, P. Gaal. Journal of Synchrotron Radiation, 26(4), 1253–1259. (2019)

(II) Quantitative disentanglement of coherent and incoherent laser-induced surface deformations by time-resolved x-ray reflectivity
M. Sander, J.E. Pudell, M. Herzog, M. Bargheer, R. Bauer, V. Besse, V. Temnov, and P. Gaal, Appl. Phys. Lett. 111, 261903 (2017)

(III) Full Spatiotemporal Control of Laser-Excited Periodic Surface Deformations
J.E. Pudell, M. Sander, R. Bauer, M. Bargheer, M. Herzog, P. Gaal. Phys. Rev. Applied, 12, 024036. (2019)

(IV) A new concept for temporal gating of synchrotron X-ray pulses D. Schmidt, R. Bauer, S. Chung, D. Novikov, M. Sander, J.E. Pudell, M. Herzog, D. Pfuetzenreuter, J. Schwarzkopf, R. Chernikov, P. Gaal. Journal of synchrotron radiation, 28 (Pt 2), 375–382. (2021)

(V) Strain induced magnetization precession in Pt/Co/Pt multilayers
R. Bauer, J. Wagner, H.P. Oepen, and P. Gaal. In preparation.

Declaration of contribution

List of the contributions to the listed publications.

(I) I participated in preparation of the experimental setup at ESRF ID09, acquisition of the experimental data, creation of simulations with UDKM toolbox, evaluation of the experimental data and discussions of the results. I contributed to writing and proofreading of the final manuscript.

(II) I participated in preparation of the experimental setup at ESRF ID09, acquisition of the experimental data, creation of simulations with UDKM toolbox, evaluation of the experimental data and discussions of the results. I contributed to writing and proofreading of the final manuscript.

(III) I participated in preparation of the experimental setup at ESRF ID09, acquisition of the experimental data, creation of simulations with UDKM toolbox, evaluation of the experimental data and discussions of the results. I contributed to writing and proofreading of the final manuscript.

(IV) I participated in development of concepts leading to the experiment and discussions of the results. I contributed to writing and proofreading of the final manuscript.

(V) I developed a mathematical model and applied it for the evaluation of the experimental data. I participated in creation of simulations for the experiment data and discussions of the results. I wrote the first draft of the manuscript and contributed to writing and proofreading of the final version.

Contents

Chapter 1

Introduction

Strain in solids and nanostructures can be used as a powerful tool for dynamic control and measurement of a wide variety of different material properties. Depending on the material, it can induce electric and magnetic fields, and even trigger phase transitions [1–7]. Moreover, its application extend beyond the solid itself as it can be used to shape diffracted and reflected X-rays, filter RF signals, switch laser pulses, drive optomechanical devices [8–12]. This thesis contains an investigation of strain applications as a tool for measurement and control of surface displacement in solids and nanostructures, application of periodic surface displacement as a tool for manipulation of X-rays at synchrotron facilities. Investigation of laser-induced excitation of ferromagnetic resonance by means of heat and acoustic waves. It attempts to answer important questions about new limits of current strain applications and expand them by an introduction of new experimental methods and theoretical analysis.

Shortening of X-ray pulses at synchrotron facilities was achieved before using a structure consisting of a single layer on top of the substrate [13]. The layer was pumped by ultra-short laser pulses, causing the change of the diffraction efficiency on timescales of picoseconds. This effect can be used to switch X-ray pulses on and off, thus shortening the pulse duration. However, heat accumulation in the pumped layer does not allow a fast return to its initial state after it was switched on and off, hence lowering the efficiency and repeatability. New multilayer structures discussed in this thesis can avoid this problem by having separate layers that serve as a laser pulse absorption medium and an X-ray diffraction layer. Their structure, application, efficiency, repeatability rate and other limitation are discussed in this thesis based on experimental data collected at ESRF.

Transient grating technique discussed in Chapter 2 is a widely used tool for creation of periodic surface displacements [14]. However, measurement of an absolute amplitude of such displacement is not a trivial task, since its typical values

are below one nanometer. An analytical method that allows to measure such surface displacements with a sub-angstrom precision and decompose it in acoustic and thermal components is presented in this thesis.

The ability to control standing surface acoustic waves by mixing, amplifying or extinguishing them through multiple subsequent excitations has been used to study a variety of physical effects. Standing acoustic waves generated by means of laser-induced transient grating excitations are always accompanied by a thermal transient grating due to the heat absorption. This thermal transient grating is often an undesired effect that interferes with the measurement by contributing to the measured signal. This thesis includes an experimental setup that achieves a full independent control of acoustic and thermal surface displacements, which was successfully deployed at ESRF ID09.

An application of strain or heat to ferromagnetic thin layers can induce a magnetization precession. Strain can directly affect the energy of the system through the magnetoelastic coupling. Increasing the temperature of a ferromagnetic thin layer changes anisotropy constants that have strong temperature dependence and determine magnetization orientation. A part of this thesis is focussed on an investigation of excitation mechanisms of the magnetization precession in Pt/Co multilayer structures.

The thesis is structured in the following way. Chapter 2 introduces experimental and theoretical methods and concepts necessary for understanding of physics used in this thesis. First, it covers laser-induced transient gratings as an important tool of dynamic strain and thermal surface displacement generation. It describes an implementation of the experimental setup used to generate transient gratings, as well as the spatial and the temporal shape of surface displacements generated by a transient grating excitation. Second, the diffraction at phase gratings is described with focus on grating shapes and parameters used in this thesis. It is an essential concept for both generation of transient gratings in an experiment setup and probing periodic surface displacements as a result of transient grating excitation. Third, magnetization dynamics and the magnetoelastic coupling. It allows an excitation and manipulation of magnetization dynamics by means of an introduction stain and heat to the sample surface.

Chapter 3 contains selected application of strain as a tool for exciting and controlling X-ray reflection and diffraction, creation and measurement of periodic surface displacements and investigation of magnetization dynamics, based on the papers included in this thesis. The following applications are discussed: Shortening and selection of X-ray pulses generated at synchrotron facilities by means of strain in-

duced in multilayered structures, from which X-rays are either reflected or diffracted. Excitation and control of both temporal and spatial parameters of periodic surface displacements in solids. Independent control of standing surface acoustic waves and thermal surface displacement. Measurement of the absolute amplitude of surface displacements with sub-angstrom precision. Investigation of strain and heat as excitation mechanisms of magnetization precession and its dynamics in Co/Pt multilayered structures.

Results described in Chapter 3 are summarized and briefly discussed in Chapter 4. Papers included in this thesis can be found and the end of the thesis as an attachment.

Chapter 2

Theoretical and experimental concepts

This chapter contains theoretical and experimental concepts necessary to understand methods of the applications of strain as a functional tool in solids and nanostructures presented in Chapter 3. A general overview of surface acoustic waves (SAW), in particular Rayleigh waves and surface-skimming longitudinal waves (SSLW) is given in Section 2.1. Rayleigh SAW and SSLW are launched when solids are excited with high-intensity ultrashort laser pulses in transient grating configuration. Section 2.2 contains a detailed description of laser-induced transient grating spectroscopy, its parameters and description of an experimental setup used in such measurements. Elements of the theory of diffraction at gratings and crystal lattice are summarized in 2.3. Their understanding is necessary for understanding of theoretical methods presented in Section 3.2.

2.1 Surface Acoustic Waves

Surface acoustic waves (SAW) are elastic waves propagating along the surface of the material. In this thesis, the term surface acoustic wave is reserved for a special type of surface acoustic waves, so-called Rayleigh surface acoustic waves. Rayleigh waves are a superposition of longitudinal pressure waves known as primary waves (P-waves) and vertical shear waves (SV-waves). In general, Rayleigh waves are dispersionless in homogeneous materials but not in materials with additional layers, e.g., coated samples. The characteristic depth above which most of a Rayleigh waves energy is contained corresponds approximately to the wavelength of the Rayleigh wave itself, with its maximum at the material surface [15, 16]. The velocity of Rayleigh waves is smaller than of respective P- and SV-waves.

Rayleigh waves can be described by a general wave equation using potential $\Phi(x, y, z, t)$ and vector potential $\mathbf{\Psi}(x, y, z, t)$ [17]:

$$\begin{aligned} \partial_t^2 \Phi(x, y, z, t) &= \alpha^2 \nabla^2 \Phi(x, y, z, t) \\ \partial_t^2 \mathbf{\Psi}(x, y, z, t) &= \beta^2 \nabla^2 \mathbf{\Psi}(x, y, z, t) \end{aligned} \tag{2.1}$$

where α and β are the velocities of the P-wave and S-wave, respectively.
These equations must satisfy a boundary condition for absence of the stress at the free surface: $\sigma_{zz} = 0$ and $\sigma_{xz} = 0$ at z = 0. In general, the displacement can be calculated from the potentials using the following expression:

$$\mathbf{u}(x, y, z, t) = \nabla \Phi(x, y, z, t) + \nabla \times \mathbf{\Psi}(x, y, z, t) \tag{2.2}$$

Using the potentials and applying the boundary conditions, the displacement for a Rayleigh wave that is travelling along the x-direction in a homogeneous material can be given explicitly as

$$\begin{aligned} u_x(x, z, t) &= A(z) \sin(kx - \omega t) \\ u_z(x, z, t) &= B(z) \cos(kx - \omega t) \end{aligned} \tag{2.3}$$

where the double exponential functions A(z) and B(z) represent a decreasing amplitude of the wave at the depth z of the material. Eq. 2.3 implies that particles in a Rayleigh wave move on elliptical paths in the opposite direction of the Rayleigh wave propagation direction.

Figure 2.1 shows a Rayleigh wave with the wavelength of 7 μm propagating in the positive direction along the x-axis. The Rayleigh wave particles, shown as the red dots, follow elliptical paths rotating counterclockwise near the surface and changing their rotation direction to clockwise below approximately 2 μm depth. The amplitude of the wave decays exponentially with the depth. Near the surface, the vertical displacement $u_z(x, 0, 0)$ is approximately 49% bigger then the horizontal displacement $u_x(x, 0, 0)$.

Surface skimming longitudinal waves are dispersive waves that propagate above a critical angle into material from its surface following an excitation of the medium. Thus, an exponential decay of their amplitude with the time is usually observed in reflective pump probe experiments [18].

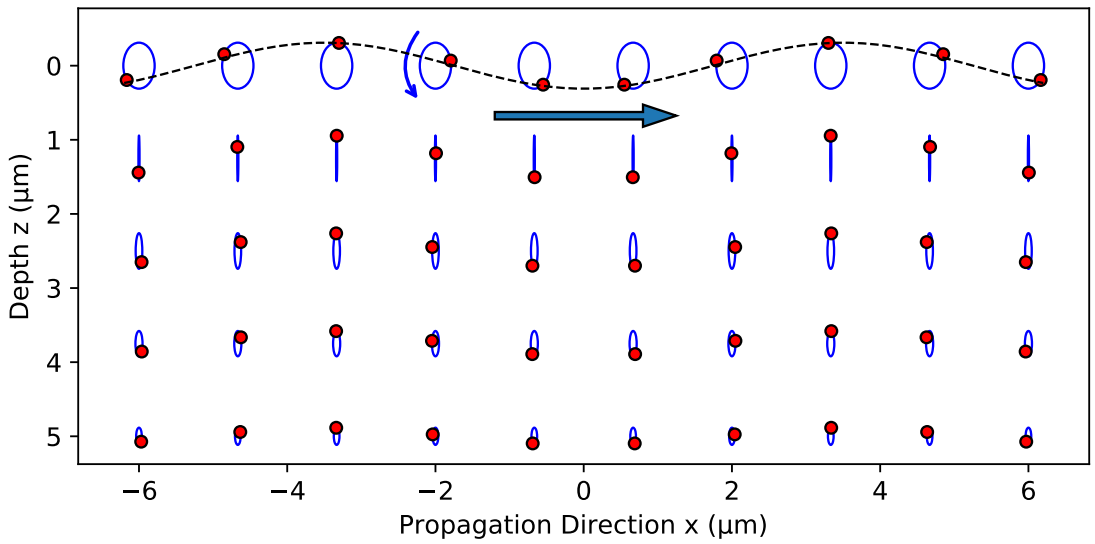

Figure 2.1: Propagation of a Rayleigh wave. The wave is propagating along the positive direction of the x-axis and has a wavelength of 7 μm. The red dots represent Rayleigh wave particles that are moving on elliptical paths. The direction of the rotation changes at a certain depth that depends on the wavelength of the wave. The amplitude of the wave decays exponentially with the depth. The displacements were calculated for a case of the equal Lamé coefficients λ and μ.

2.2 Transient Grating Spectroscopy

2.2.1 Overview

Transient Grating technique is an experimental setup configuration that allows non-destructive measurements of a big variety of material properties, such as directional dependent sound velocities, temporal heat-induced and strain-induced surface displacement, control of coherent phonon excitations and properties of strain induced magnetic excitations [19–26]. The laser-induced transient grating excitation is achieved by overlapping two tilted laser beams that interfere on the surface of the sample [27], as depicted in Figure 2.3. This leads to a sinusoidal intensity distribution, which is modulated by a transverse beam profile. The energy of the exciting pulses is absorbed by the electrons and then transferred to the lattice within a few picoseconds due to electron-phonon scattering. The full cascade of energy transfer from laser excitation to strain generation is not discussed in this thesis because investigated strain propagation and heat diffusion phenomena occur on smaller timescales.

Excitations with different wavelengths, fluence and temporal pulse width can trigger different processes within the sample. The wavelength of the exciting pulse determines the penetration depth and is responsible for the longitudinal energy distribution within the sample [18]. A TG excitation with nanosecond long pulses creates a transient sinusoidal surface displacement that lasts on the timescales of tens to hundreds of nanoseconds, depending on the fluence. Such surface displacement is a result of the material expansion due to the temperature change and depends on heat capacity and expansion coefficient of the material. The decay time of its amplitude depends on in-plane and out-of-plane thermal conductivity coefficients [28]. The heat from repeated excitations can accumulate if the time between excitations is not enough for it to completely dissipate. This creates an additional surface displacement and can have an effect on the shape of the induced grating. For most cases, the heat induced surface displacement $u_{th}(x,t)$ can be described as

$$u_{th}(x,t) = \frac{u_0}{2} e^{-\alpha_x q_\parallel^2 t}(1 + \sin(q_\parallel x - \phi_x)) \tag{2.4}$$

where α_x is the in-plane thermal diffusivity, ϕ_x the spatial phase shift and $q_\parallel = \frac{2\pi}{\Lambda}$ with Λ being the grating period.

Ultrashort laser pulses with fluences of a few mJ/cm^2 can in addition to creation of a thermal grating also excite acoustic waves with amplitudes high enough to be measured experimentally. Such excitations manifest in additional surface displacement on top of the thermal displacement. This measurable displacement is a result of acoustic waves such as surface acoustic waves (SAW), surface skimming longitudinal waves (SSLW) and others. These waves are launched at the same times from different points of the induced grating, and their overlap results in a standing wave with a spatial period Λ. Their oscillation period T depends on the sound velocity of their respective mode c and can be calculated as $T = \Lambda/c$. The surface displacement caused by a standing surface wave can be described as

$$u_{\mathrm{ac}}(x,t) = \frac{u_0}{2} \sin(q_\parallel x - \phi_x) \cos(\omega t - \phi_t) \tag{2.5}$$

where u_0 is the peak-to-peak amplitude of the displacement and ϕ_t the temporal phase shift. The total amplitude of the surface displacement $u(x,t)$ is the sum of displacements cause by thermal expansion and acoustic wave $u(x,t) = u_{th}(x,t) + u_{\mathrm{ac}}(x,t)$. The observed decay rate of the amplitude of an induced standing acoustic wave can differ a lot, depending on the type of the wave. In reflective measurements, the SSLW is usually observed for a few hundred picoseconds, depending on its speed and how far the reflected probe beam propagates inside of the sample.

In transmission measurements, it can be observed for much longer time until it dissipates its energy. A SAW can be observed for hundreds of nanoseconds with no significant change of amplitude.

Figure 2.2 (top) shows results obtained from a reflective pump probe experiments on gold-coated AlN sample. The sample was excited by 150 fs laser pulses in TG geometry with transient grating period of $\Lambda = 2.6$ µm. The data was fitted using Eq. 2.4 for a double exponential thermal decay and Eq. 2.5 for SAW and SSLW. A double exponential decay is usually observed in optically and X-ray probed transient grating experiments [29]. Two different decay constants can be attributed to the in- and out of plane decay of the thermal grating. The individual components of measured signal extracted from the fit are shown in Fig. 2.2 (middle). The contribution of the thermal grating to the measured signal is shown in red. The thermal decay rates obtained from the fit are 450 ps and 1.37 ns. The Rayleigh SAW is shown in blue and SSLW in green. The frequencies of the SAW and SSLW are 4.08 GHz and 6.91 GHz, respectively. The dip at approximately 20 ps stems from the overlap of the Rayleigh SAW and the SSLW. This is a typical feature seen in TG experiments. However, it cannot be observed in synchrotron-based time resolved X-ray reflectivity (TR-XRR) experiments show in [29,30] due to the limited temporal resolution. This model does not provide a perfect fit due to several reasons. First, the detector is not sensitive to the sign of the surface displacement along the surface normal unless there is an offset present. Thus, when the thermal grating has decayed below the amplitude of the acoustic mode, the detector rectifies the transient signal, resulting in homodyne detection of the signal. Homodyne and heterodyne detection in TR-XRR measurements is shown in [29]. This can contribute to the second harmonic of the SAW seen in Fig. 2.2 (bottom), which shows an FFT of the difference between the data and the fit. Second, the FFT shows an additional oscillation with 11 GHz frequency not described by the model. This frequency is the sum of 4.08 GHz SAW and 6.91 GHz SSLW frequencies.

Different probing techniques allow measurement of different material properties and ability to differentiate between them. For example, probing with X-ray under small angle is sensitive to the surface displacement, while probing with visible light, measures thermally and elastically induced change of the refractive index in addition to surface displacement.

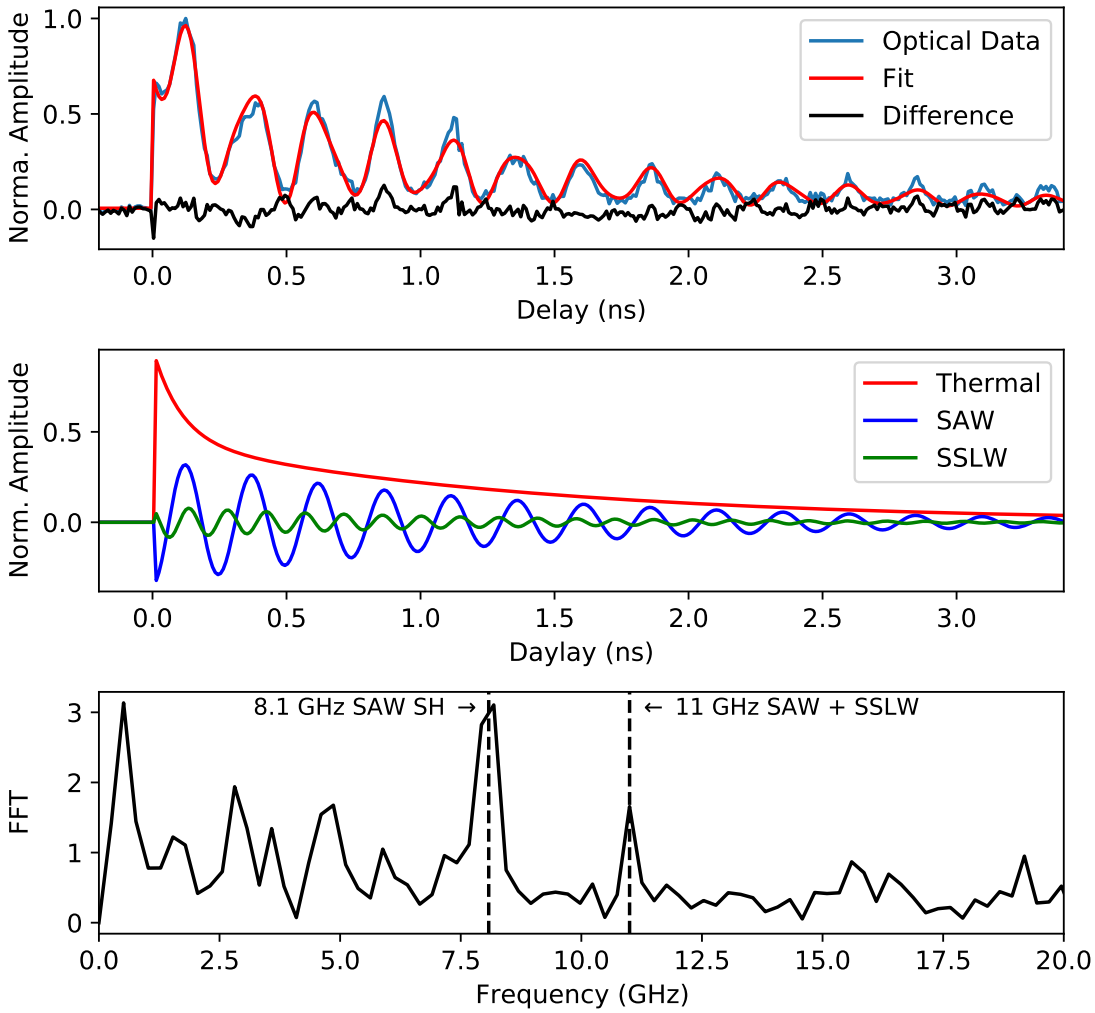

Figure 2.2: Transient grating excitation of gold-coated AlN sample. The period of the transient grating is 2.6 µm. The sample was pumped with 800 nm and probed with 400 nm laser pulses with 150 fs pulse width. (top) Measured optical data and the respective fitted curve based on Eq. 2.4 and 2.5. The difference between the measured data and the fitted curve is shown in black. (middle) Decomposition of the excitation signal in single components. The double exponential decay is shown in red, the SAW (4.08 GHz) is shown in blue and SSLW (6.91 GHz) in green. (bottom) FFT of the data and fit difference shows presence of the second harmonic of the SAW (8.1 GHz) as well as sum of SAW and SSLW frequencies (11 GHz).

2.2.2 Implementation of experimental setup for TG spectroscopy

Creation of laser induced transient grating requires spatial and temporal overlap of two laser pulses at the sample surface. One of the ways to achieve this, is to split incoming laser beam with help of a diffraction grating and use a system of lenses to guide both beams to the same spot on the sample surface. A schematic implementation of such setup is depicted in Figure 2.3.

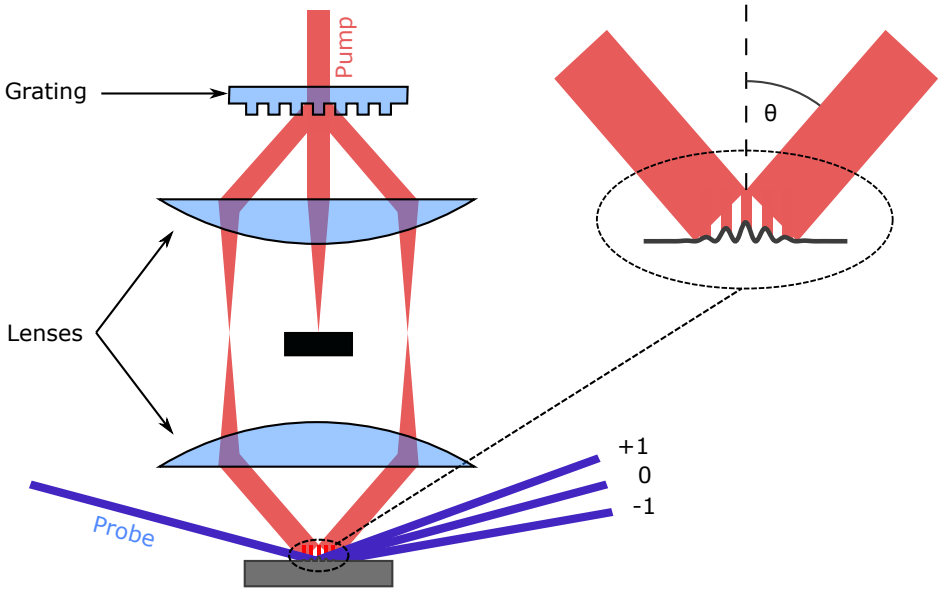

Figure 2.3: Laser Induced Transient Grating setup. The pump beam is split by a diffraction grating and subsequently collected by an imaging system consisting of two cylindrical lenses. First and minus first orders of the diffracted beam are redirected to the same spot on the sample where they interfere, resulting in a sinusoidal thermal grating modulated by the transverse beam shape. The sample surface with the induced grating is probed by either X-ray or laser beam.

A laser beam passes through an optical phase grating and is split into multiple diffraction order beams. The phase grating is optimized to provide maximum intensity in +1st and -1st first orders. The beams of +1st and -1st first orders are collected and refocused on the sample surface by a pair of cylindrical lenses in 4f geometry. The 0th and higher orders of the diffraction, as well as the reflection, are blocked. In this geometry, each individual beam is not focussed on the sample surface by itself, but its size is affected by the magnification of the lens system. This means that for a unitary magnification of the imaging system, the spot size on the surface is the same as the initial beam radius. In the region where the overlapping beams cross, an area with periodic intensity modulation is created.

Such configuration has multiple advantages over other implementations. First,

it is very stable since it does not have a sharp focussing plane and is not sensitive to the distance between the sample and imaging system as long as the sample stays inside the interference region. However, the spot size will change if the sample is moved along the optical axis. Second, it guarantees a temporal overlap of both beams, as the optical path of both beams passing through a lens is always the same. Third, the wavefronts of both beams are perpendicular to the sample surface, which is a result of properties of a phase grating.

This experimental setup can be expanded and modified for different experiments. To achieve a higher fluence, an additional cylindrical lens rotated by 90° relative to the other two lenses can be placed at the focal distance from the sample, making the overlap more narrow. Multiple excitation pulses can be used to excite the sample at the same time or with a required delay. This can be achieved by passing the incoming beam through a Michelson interferometer. A variable arm length of the interferometer provides a variable delay between both pulses. A precision of a few femtoseconds can be achieved by placing one of the interferometer mirror on an optical delay stage with a micrometer resolution. Further, the spatial phase of the induced grating can be controlled using two quarter-wave plates placed into +1st and -1st order diffraction beams parallel or perpendicular to their polarization.

2.2.3 Characteristic parameters of TG setup

The projected grating can be characterized by its intensity distribution, grating period, spatial shape, temporal shape, wavelength, and phase. The wavelength, spatial and temporal shapes are given by the properties of the laser beam used in the experiment.

The intensity distribution on the sample surface $I(\mathbf{r})$ is given by

$$\begin{aligned} I(\mathbf{r}) &= |\mathbf{E_1} \exp(i\mathbf{k_1} \cdot \mathbf{r}) + \mathbf{E_2} \exp(i\mathbf{k_2} \cdot \mathbf{r})|^2 \\ &= |\mathbf{E_1}|^2 + |\mathbf{E_2}|^2 + 2|\mathbf{E_1} \cdot \mathbf{E_2}| \cos((\mathbf{k_1} - \mathbf{k_2}) \cdot \mathbf{r}) \end{aligned} \tag{2.6}$$

where $\mathbf{E_1}, \mathbf{E_2}$ are electric fields or first and minus first orders and $\mathbf{k_1}, \mathbf{k_2}$ their respective wave vectors. The intensity $I(\mathbf{r})$ is periodic and reaches its maximum when $\cos((\mathbf{k_1} - \mathbf{k_2}) \cdot \mathbf{r}) = 1$. Both beams of the first order of diffraction with wave vectors, $\mathbf{k_1}$ and $\mathbf{k_2}$ have the same perpendicular components with respect to the sample plane. Their parallel components have the same magnitude but opposite signs, leading to

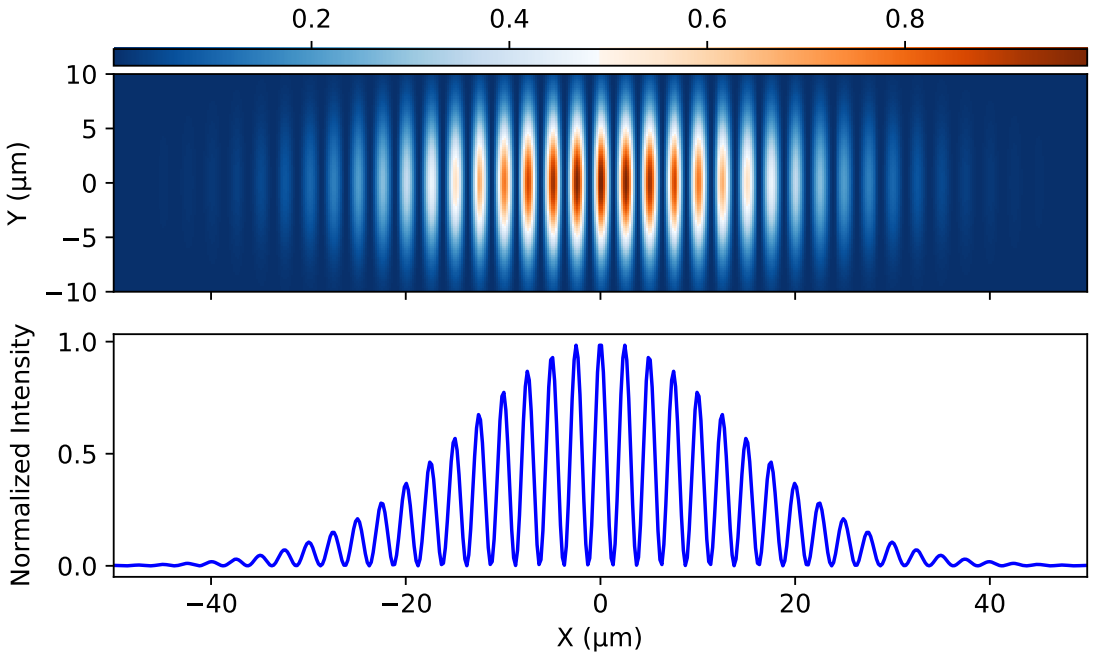

Figure 2.4: Calculated intensity distribution of two overlapping Gaussian beams on the sample surface. The beam size is 20 µm x 6 µm and grating period 2 µm. The interference of two beams creates an intensity grating with grating period depending on the wavelength and incidence angle.

$$\mathbf{k_1} - \mathbf{k_2} = \begin{pmatrix} k_\perp \\ k_\parallel \end{pmatrix} - \begin{pmatrix} k_\perp \\ -k_\parallel \end{pmatrix} = \begin{pmatrix} 0 \\ 2k_\parallel \end{pmatrix} \tag{2.7}$$

where $k_\parallel = k \sin\theta$ with θ being the angle between surface normal and pump beam. Using periodicity condition $\mathbf{k} \cdot \mathbf{r} = 2k\Lambda \sin\theta = 2\pi$ yields the period of the induced grating

$$\Lambda = \frac{\lambda}{2 \sin\theta} = \frac{d}{2M} \tag{2.8}$$

where d is the period of the phase grating used to split the pump beam, $M = f_1/f_2$ the magnification of the imaging system and λ the wavelength of the used laser beam [31]. The result is in contrast to the geometrical imaging theory where the period of the projected grating would be the same as the period of the diffraction grating assuming $M = 1$ and the induced grating sharp in image plane only. The right part equation Eq. 2.8 uses parameters of the experimental setup described in Section 2.2.2. It can be seen that such setup configuration eliminates the wavelength and the incidence angles from the equation, making its implementation suitable for multiple wavelength.

From Eq. 2.6 we can see that the maximum intensity in the induced grating is four time the intensity in the single pump beam and the minimum is zero. The calculated intensity distribution of the induced transient grating in shown in Fig. 2.4. (The Gaussian transverse beam shape is assumed.) The period of the induced grating can be controlled by tilting the diffraction grating, changing the magnification or selecting phase grating with difference period [32].

2.3 Diffraction

2.3.1 Diffraction at an optical phase grating

The diffraction of electromagnetic waves is best described by solving Maxwell equations with appropriate boundary conditions. Although such description is precise in the classical limit, it requires solving partial differential equations, which in most cases cannot be done analytically. For most applications, an exact solution is not required, and the problem can be simplifiedin multiple ways. First, the amplitude of the electromagnetic field can be treated as a scalar field, thus neglecting the information about the polarization of the diffracted wave. Second, the diffraction pattern is described by a sum of spherical waves emitted from every point of the grating surface as a response to a given input field:

$$A(x,y) = \frac{1}{\lambda i} \iint \frac{A(x',y')}{r} e^{ikr} \cos\theta dx' dy' \tag{2.9}$$

$A(x',y')$ is the amplitude of an incoming wave at the point (x',y') of the grating surface and θ is the angle between the incoming wave and the surface normal. This equation is known as Rayleigh–Sommerfeld diffraction integral. Figure 2.5 shows the coordinate system with relationship between $\mathbf{r} = (x,y,z)$ and $\mathbf{r}' = (x',y',z')$. A detailed description of the Rayleigh–Sommerfeld diffraction theory, its derivation and computation methods can be found in [33–37].

The integral in the Eq. 2.9 gives a precise solution for many diffraction problems but is still hard to calculate because of $r = \sqrt{(x-x')^2 + (y-y')^2 + z^2}$ containing a root expression in the phase term. Therefore, further simplifications can be done assuming that the distance between the grating and the imaging plane is much larger than the grating period.

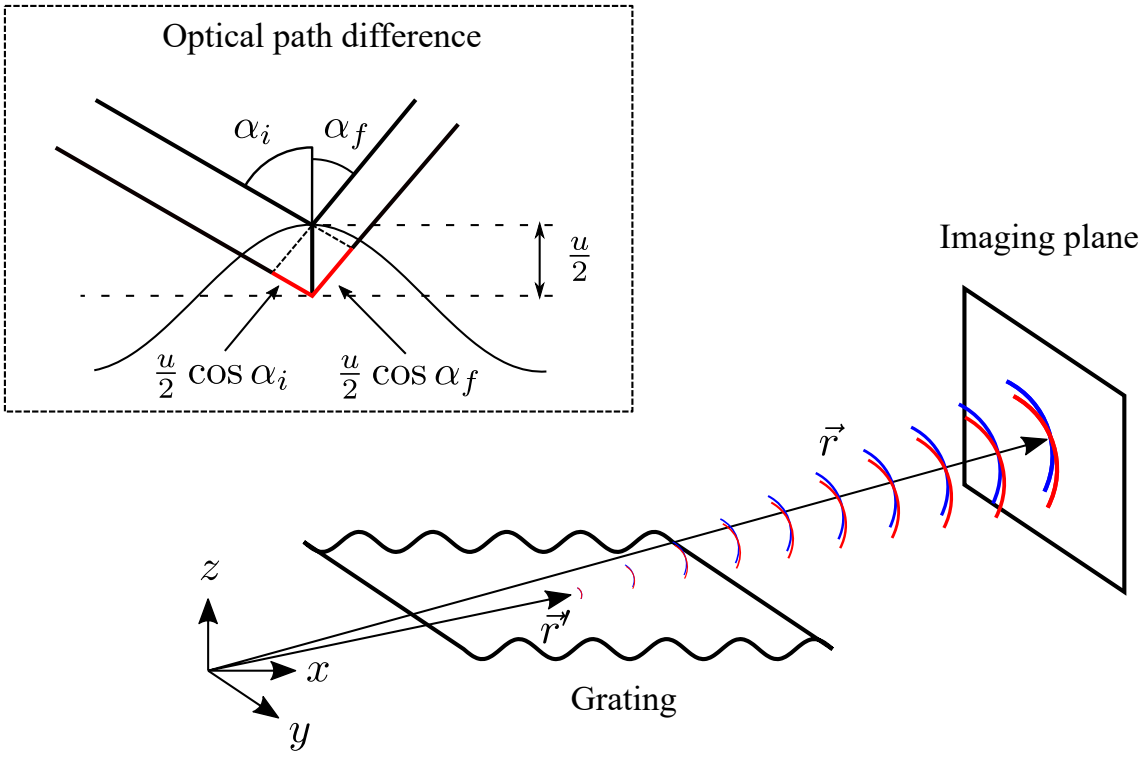

Figure 2.5: Diffraction at sinusoidal phase grating. The coordinate system is chosen in a such way that the grating grooves are parallel to the y-axis. The vector $\mathbf{r}' = (x', y', z')$ points to the point on the grating and $\mathbf{r} = (x, y, z)$ to the point on the imaging plane. The optical path difference (OPD) is shown on the top-left with the incidence angle α_i and the diffraction angle α_f. The total OPD is $\frac{u}{2}(\cos\alpha_i + \cos\alpha_f)$ for u being the peak-to-peak grating amplitude.

$$r = z\sqrt{\left(\frac{x-x'}{z}\right)^2 + \left(\frac{y-y'}{z}\right)^2 + 1} \approx \frac{(x-x')^2 + (y-y')^2}{2z} + z \tag{2.10}$$

$$\approx \frac{x^2+y^2}{2z} - \frac{xx'+yy'}{z} + z \tag{2.11}$$

In the approximation done in Eq. 2.10 the radius r is expanded up to the first term of the Taylor series. This is known as Fresnel (near-field) approximation. It can be further simplified by neglecting x'^2 and y'^2 terms if they are much smaller than z. This additional approximation, shown in Eq. 2.11, is known as Fraunhofer (far-field) approximations. Plugging Eq. 2.11 in Eq. 2.9 leads to the Fraunhofer diffraction integral

$$A(x,y) \propto \iint A(x',y')e^{-2\pi i(f_x x' + f_y y')}dx'dy' \tag{2.12}$$

which is proportional to the Fourier transform of the complex incoming field amplitude with $f_x = \frac{x}{\lambda z}$ and $f_y = \frac{y}{\lambda z}$, where λ is the wavelength of the beam.

The analysis of a sinusoidal grating in Fraunhofer approximation is described by in detail by Goodman [33] and expanded in [38–40]. The complex amplitude of the input field is given as

$$A(x', y') \propto e^{i\Delta\phi \sin(2\pi x'/\Lambda)} = \sum_{n=-\infty}^{\infty} J_n(\Delta\phi)\, e^{2\pi i n x'/\Lambda} \tag{2.13}$$

where A does not depend on y due to the chosen geometry depicted in Fig. 2.5. The J_n are Bessel functions of the first kind, and $\Delta\phi$ is the phase difference. Plugging the expression given in the Eq. 2.13 into Eq. 2.12 leads to

$$A(x, y) \propto \int \sum_{n=-\infty}^{\infty} J_n(\Delta\phi)\, e^{2\pi i (n/\Lambda - f_x)x'} dx' = \sum_{n=-\infty}^{\infty} J_n(\Delta\phi)\, \delta(n/\Lambda - f_x) \tag{2.14}$$

where δ is the delta function. This means that $\frac{n}{\Lambda} - f_x = 0 \Rightarrow \frac{x}{z} = \frac{n\lambda}{\Lambda}$, resulting in a pattern with discrete amplitude maxima given by the index n.

The phase difference $\Delta\phi$ for the diffraction at a grating with an arbitrary incidence angle was derived by Harvey and Pfisterer [38]. For the peak-to-peak grating amplitude u the phase difference can be written as a function of the incidence angle α_i and the diffraction angle α_f

$$\Delta\phi = \frac{2\pi}{\lambda}\mathrm{OPD} = \frac{\pi u}{\lambda}(\cos\alpha_i + \cos\alpha_f) \tag{2.15}$$

The optical path difference (OPD) is shown in Fig. 2.5 in red.

The intensity of the beam is the square of its complex amplitude $I(x, y) = |A(x, y)|^2$ and the efficiency in the n-th order can be written as

$$\eta_n = \frac{K}{\cos\alpha_n} |J_n(\Delta\phi)|^2 \tag{2.16}$$

with K being the renormalization factor [38]. The renormalization factor K is given by [41, 42]

$$K = \frac{1}{\sum_{\text{Prop. Orders}} \eta_n} \tag{2.17}$$

The maximum efficiency expected from Eq. 2.16 is the maximum of the square of the Bessel function $\max(|J_1(x)|^2) \approx 33\%$. However, this prediction is only valid for the paraxial approximation, which is equivalent to the Fraunhofer approxima-

tion. Non-scalar diffraction theories and rigorous EM theory predict much higher diffraction efficiencies for $\lambda/\Lambda > 0.1$ [43–45]. Harvey et al. states that diffraction efficiencies up to 100 % can be achieved in +1th order of the sinusoidal grating by choosing the grating period and tilt angle so that only +1th order appears and subsequently varying the grating amplitude to shift intensity from 0th to 1st order. [46]

The diffraction can also be described using the momentum conservation law as

$$\mathbf{k_d} = \mathbf{k_i} + \mathbf{Q} \tag{2.18}$$

where $\mathbf{k_i}$ and $\mathbf{k_d}$ are incident and diffracted light wave vectors. $\mathbf{Q}$ is the momentum supplied by the grating with $|\mathbf{Q}| = \frac{2\pi}{\Lambda}$ where Λ is the grating period. Diffraction at the grating is an elastic scattering process where the wavelength of scattered photons is not changed $|\mathbf{k_d}| = |\mathbf{k_i}|$ and no energy is transferred between scattered photons and the grating.

2.3.2 Diffraction at crystal lattice

Diffraction at crystal lattice is nothing else than the diffraction at grating as described in 2.3.1, meaning that Eq. 2.9 - 2.12 can be used in the same manner as before. However, unlike the sinusoidal phase grating described in 2.3.1, the lattice is a discrete grating with each atom type having its own specific cross section.

The crystal lattice can be defined by its periodicity and every point of the lattice can be described as a lattice vector

$$\mathbf{R} = n_1\mathbf{a_1} + n_2\mathbf{a_2} + n_3\mathbf{a_3} \quad (n_1, n_2, n_3 \in \mathbb{Z}) \tag{2.19}$$

where $\{\mathbf{a_i}\}$ is a set of primitive vectors spanning the lattice. Using periodicity of the electron density in crystal $n(\mathbf{r}) = n(\mathbf{r} + \mathbf{R})$ and performing the Discrete Fourier Transform

$$n(\mathbf{r} + \mathbf{R}) = \sum \tilde{n} e^{i\mathbf{G}\cdot(\mathbf{r}+\mathbf{R})} = \sum \tilde{n} e^{i\mathbf{G}\cdot\mathbf{r}} e^{i\mathbf{G}\cdot\mathbf{R}} = n(\mathbf{R}) = \sum \tilde{n} e^{i\mathbf{G}\cdot\mathbf{r}} \tag{2.20}$$

we can obtain the periodicity condition $e^{i\mathbf{G}\cdot\mathbf{R}} = 1$ or $\mathbf{G}\cdot\mathbf{R} = 2\pi n \quad (n \in \mathbb{Z})$. The vector

$$\mathbf{G} = h_1\mathbf{b_1} + h_2\mathbf{b_2} + h_3\mathbf{b_3} \quad (h_1, h_2, h_3 \in \mathbb{Z}) \tag{2.21}$$

is called reciprocal space vector, and the set of vectors $\{\mathbf{b_i}\}$ constitute the basis of the reciprocal space.

The X-ray diffraction at the crystal lattice follows very similar principles as the

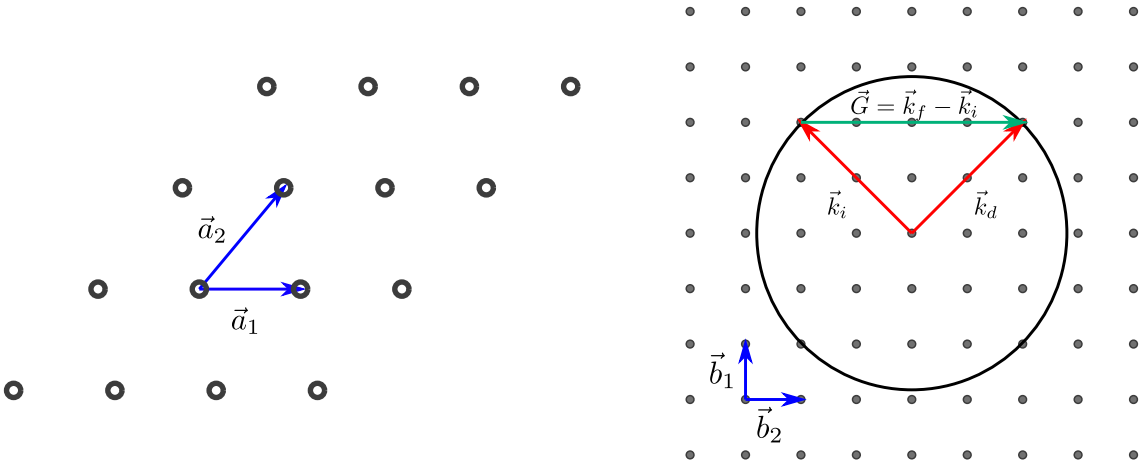

Figure 2.6: (left) Schematic depiction of two-dimensional periodic crystal lattice with basis vectors a_1 and a_2. (right) The Ewald sphere in reciprocal space. In a perfect crystal, the diffraction is only possible if the momentum transfer between photons and lattice correspond exactly to the reciprocal space vector.

diffraction at the grating described in 2.3.1. For the diffracted X-ray photons holds the momentum conversation in the form

$$\mathbf{k_d} = \mathbf{k_i} + \mathbf{Q} = \mathbf{k_i} + \mathbf{G} \tag{2.22}$$

with $|\mathbf{k_d}| = |\mathbf{k_i}|$ where $\mathbf{G}$ is the reciprocal lattice vector defined in Equation 2.21. Figure 2.6 shows on the left an example of crystal lattice with its basis vectors and on the right the Ewald sphere. The Ewald sphere represents all possible diffraction peaks at the points where it intersects with the reciprocal lattice.

The intensity of diffraction reflex $I(\mathbf{G})$ on the number of elementary cells N and the structure factor S:

$$I(\mathbf{G}) \propto |NS(\mathbf{G})|^2 \tag{2.23}$$

where the structure factor is the Fourier transform of the electron density of the elementary cell

$$S(\mathbf{G}) = \int n(\mathbf{r}) e^{-i\mathbf{G}\cdot\mathbf{r}} dV \tag{2.24}$$

More detailed description lattice structure and diffraction at crystal lattice can be found in [47, 48]

2.4 Magnetic anisotropy and magnetization dynamics

2.4.1 Magnetic anisotropy

The magnetic anisotropy in solids arise mainly from two sources: the magnetic dipole and the spin-orbit interactions [49]. The long range dipole-dipole interactions are responsible for the anisotropy contribution that depends on the shape of the solid and is called the shape anisotropy. The spin-obit interaction couples the intrinsic magnetic moments of electrons to the crystal axes. This type of the anisotropy is called the magnetocrystalline anisotropy.

Shape anisotropy

The shape anisotropy can be calculated from the expression for the energy density of the magnetic field:

$$K_{shape} = \frac{E}{V} = -\frac{\mu_0}{2} \int \mathbf{H_d} \cdot \mathbf{M} dV \tag{2.25}$$

where μ_0 is the vacuum permeability, $\mathbf{M}$ is the magnetization and $\mathbf{H_d}$ the demagnetizing field. In general, it is not trivial to calculate the demagnetizing field as it depends on the shape of the object. The integral in Eq. 2.25 can be still evaluated for special cases such as highly symmetrical structures (e.g. sphere, cube, cylinder) or thin films. For the important case of infinite ultra thin films, it collapses into a simple expression:

$$K_{shape}(T) = \frac{\mu_0}{2} M_s(T)^2 \tag{2.26}$$

where $K_{shape}(T)$ is a function of the saturation magnetization $M_s(T)$, which in turn depends on the temperature T.

Magnetocrystalline anisotropy

The magnetocrystalline anisotropy is a result of the spin-obit interaction and its coupling to the crystal axes. Its value depends on the projection of the magnetization vector onto the crystal axes and can be calculated by developing the free energy density in Taylor series [50, 51]:

$$f(T) = b_0 + \sum_i b_i \alpha_i + \sum_{ij} b_{ij} \alpha_i \alpha_j + \sum_{ijk} b_{ijk} \alpha_i \alpha_j \alpha_k + \sum_{ijkl} b_{ijkj} \alpha_i \alpha_j \alpha_k \alpha_l ... \quad (2.27)$$

where α_i are the directional cosines of the magnetization orientation. They are projections of the normalized magnetization vector on the crystal axes and can be written as $\alpha_i = \hat{\mathbf{e}}_\mathbf{i} \cdot \mathbf{M}/M_s$ (see Fig. 3.9). Due to the energy symmetry with respect to the orientation of magnetization, only components with even number of indices are different from zero.

For systems with cubic symmetries, the expression above can be reduced to

$$f(T) = K_0(T) + K_1(T)(\alpha_1^2\alpha_2^2 + \alpha_2^2\alpha_3^2 + \alpha_3^2\alpha_1^2) + K_2(T)\alpha_1^2\alpha_2^2\alpha_3^2 ... \quad (2.28)$$

where $K_0(T)$ is the linear combination of the second order expansion coefficients b_{ij} and $K_1(T)$ a linear combination of the fourth order expansion coefficients b_{ijkl}. Since the first summand does not depend on the direction of the magnetization, the K_0 term can be neglected when describing magnetization dynamics. For many systems K_2 is much smaller than K_1 and can be neglected in the first approximation.

For systems with the uniaxial symmetry, the contribution of the uniaxial magnetocrystalline anisotropy to the free energy density can be written as

$$f(T) = -K_1(T)\cos^2\vartheta = K_1(T) + K_1(T)\sin^2\vartheta \quad (2.29)$$

where ϑ is the angle between the symmetry axis and the magnetization vector as described in spherical coordinates (φ, ϑ).

For thin films, $K_1(T)$ depends strongly on the thickness of the film and can be decomposed into two parts: the volume anisotropy and the surface/interface anisotropy.

$$K_1(T) = K_{1,V}(T) + \frac{2K_{1,S}(T)}{d} \quad (2.30)$$

where $K_{1,V}(T)$ is the magnetocrystalline volume anisotropy, $K_{1,S}(T)$ the surface anisotropy and d is the thickness of the film. This decomposition is valid only up to the certain thickness d that depends on the particular system [52, 53].

The total stationary uniaxial contribution to the free energy density can be written as

$$f(T) = K_{1,eff}(T)\sin^2\vartheta = \left[K_{1,V}(T) + \frac{2K_{1,S}(T)}{d} - \frac{\mu_0}{2}M_s(T)^2\right]\sin^2\vartheta \qquad (2.31)$$

In thermodynamic equilibrium, the free energy density f in the Eq. 2.31 is at its minimum. The positive contributions from the volume and the surface anisotropy increase the free energy density and the negative contribution of the shape anisotropy decreases it. Which means that the volume and the surface anisotropies try to decrease the angle ϑ and rotate the magnetization out of the plane, while the shape anisotropy tries to increase ϑ and keep the magnetization in the plane. The direction of the easy axis of the magnetization is then decided by which part of the free energy contribution is bigger; in other words, it depends on the sign of $K_{1,eff}(T)$.

2.4.2 Temperature dependence of anisotropy and magnetoelastic constants

All anisotropy and magnetoelastic constants are functions of the temperature. The temperature dependence of the shape anisotropy $K_{shape}(T)$ comes from the temperature dependence of the saturation magnetization $M_s(T)$ (See Eq. 2.26). An expression for the temperature dependence of the saturation magnetization $M_s(T)$ of ferromagnets over a wide range of temperatures was proposed by Kuz'min [54].

$$M_s(T) = M_s(0)\left[1 - s\left(\frac{T}{T_C}\right)^{3/2} - (1-s)\left(\frac{T}{T_C}\right)^{p}\right]^{1/3} \qquad (2.32)$$

$M_s(0)$ is the saturation magnetization at $T = 0$, T_C is the Curie temperature, s and p are the material specific parameters.

The temperature dependence of the magnetocrystalline volume and surface anisotropy was first described for by Akulov [51] and later for the magnetoelastic constants by Callen and Callen [55]. In general, they depend on some power n of the saturation magnetization:

$$\frac{K(T)}{K(0)} = \left(\frac{M_s(T)}{M_s(0)}\right)^n, \quad \frac{B_{1,2}(T)}{B_{1,2}(0)} = \left(\frac{M_s(T)}{M_s(0)}\right)^n \qquad (2.33)$$

with $n = l(l+1)/2$ for the magnetocrystalline anisotropy. Experiments show that for thin structured films, the power n can differ from that prediction, but the overall structure of the equations seems to be preserved.

A polycrystalline structure with a random grain orientation can macroscopically exhibit an uniaxial anisotropy as a result of the sum of the magnetizations of all

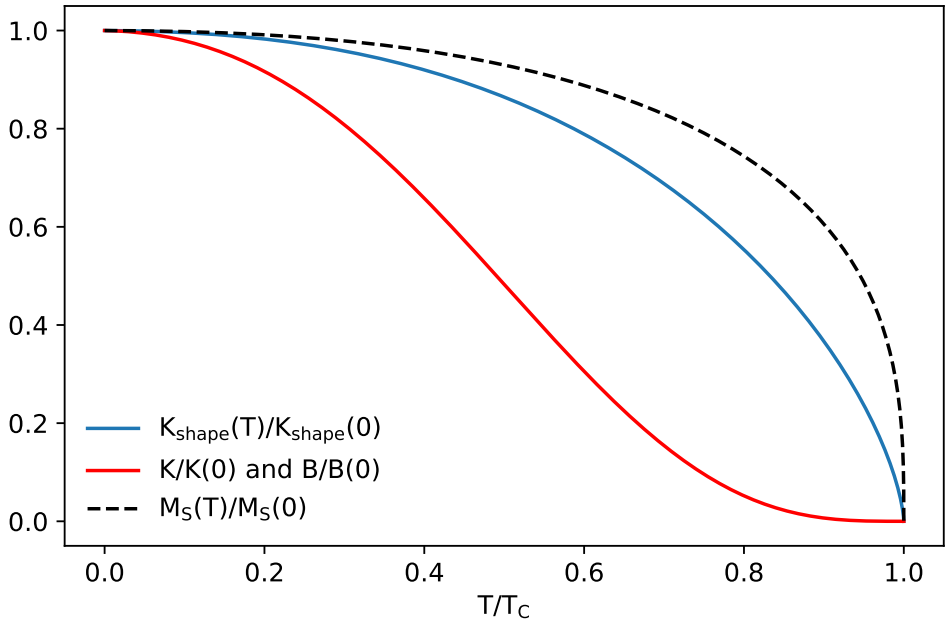

Figure 2.7: Temperature dependence of saturation magnetization, magnetocrystalline anisotropy and magnetoelastic constants for fcc Co. The shape anisotropy decreases at slower rate with rising temperature than magnetocrystalline anisotropy and magnetoelastic constants. The values used: $n = 10$, $p = 5/2$, $s = 0.11$.

grains, however each grain on its own can have e. g. a cubic symmetry meaning that in this case the value for n would be 10. The temperature dependence of the saturation magnetization, the shape, the magnetocrystalline anisotropy and the magnetoelastic constants for fcc Co is shown in Fig. 2.7. The magnetocrystalline anisotropy and the magnetoelastic constants decrease faster with an increasing temperature than the shape anisotropy due to $n > 2$. The Eq. 2.33 was initially derived with assumption of low temperatures but has been shown experimentally to be fairly precise for a wide range of temperatures [55].

2.4.3 Equations of motion of the magnetization vector

The time evolution of the magnetization vector $\mathbf{M}$ is described by the Landau–Lifshitz equation

$$\dot{\mathbf{M}} = -\gamma \mathbf{M} \times \mathbf{B}_{\text{eff}} - \frac{\alpha\gamma}{M_s} \mathbf{M} \times (\mathbf{M} \times \mathbf{B}_{\mathbf{eff}}) \tag{2.34}$$

where γ is the gyromagnetic ratio, α is the damping factor and $\mathbf{B}_{\mathbf{eff}}$ is the effective magnetic field [56]. The effective magnetic field can be calculated as the negative gradient of the free energy density with respect to the magnetization vector [57].

Substituting $\mathbf{B}_{\text{eff}} = -\nabla_M f$ in Eq. 2.34 and ignoring the damping term leads to the equation of motion of the magnetization vector in Cartesian coordinate system.

$$\dot{\mathbf{M}} = \gamma \mathbf{M} \times \nabla_M f \tag{2.35}$$

To obtain the torque components $\dot{\vartheta}$ and $\dot{\varphi}$ one has to calculate the time derivative of the magnetization vector $\mathbf{M} = M_s \hat{\boldsymbol{r}}$ and the gradient of the free energy density in spherical coordinates.

$$\dot{\mathbf{M}} = \frac{d}{dt}\left(M_s \hat{\boldsymbol{r}}\right) = \dot{M}_s \hat{\boldsymbol{r}} + M_s \dot{\vartheta} \hat{\boldsymbol{\vartheta}} + M_s \dot{\varphi} \sin\vartheta \hat{\boldsymbol{\varphi}} \tag{2.36}$$

$$\nabla_M f = \frac{\partial f}{\partial M_s} \hat{\boldsymbol{r}} + \frac{1}{M_s} \frac{\partial f}{\partial \vartheta} \hat{\boldsymbol{\vartheta}} + \frac{1}{M_s \sin\vartheta} \frac{\partial f}{\partial \varphi} \hat{\boldsymbol{\varphi}} \tag{2.37}$$

In spherical coordinates, the basis vectors $\hat{\boldsymbol{r}}$, $\hat{\boldsymbol{\vartheta}}$ and $\hat{\boldsymbol{\varphi}}$ are time-dependent. Using Eq. 2.36 and 2.37, the right-hand site of the Eq. 2.35 can be written as

$$\begin{aligned} \mathbf{M} \times \nabla_M f &= M_s \hat{\boldsymbol{r}} \times \left[\frac{\partial f}{\partial M_s} \hat{\boldsymbol{r}} + \frac{1}{M_s} \frac{\partial f}{\partial \vartheta} \hat{\boldsymbol{\vartheta}} + \frac{1}{M_s \sin\vartheta} \frac{\partial f}{\partial \varphi} \hat{\boldsymbol{\varphi}} \right] \\ &= \frac{\partial f}{\partial \vartheta} \hat{\boldsymbol{\varphi}} - \frac{1}{\sin\vartheta} \frac{\partial f}{\partial \varphi} \hat{\boldsymbol{\vartheta}} \end{aligned} \tag{2.38}$$

Comparing Eq. 2.36 and 2.38 and assuming that M_s does not depend on time yields the equations of motion of the magnetization vector in spherical coordinates:

$$\dot{\vartheta} = -\frac{\gamma}{M_s \sin\vartheta} \frac{\partial f}{\partial \varphi} \quad \text{and} \quad \dot{\varphi} = \frac{\gamma}{M_s \sin\vartheta} \frac{\partial f}{\partial \vartheta} \tag{2.39}$$

Since, the torque $\boldsymbol{\tau} = -\dot{\mathbf{M}}/\gamma$ is proportional to the change of the magnetization in time, $\dot{\vartheta}$ and $\dot{\varphi}$ are sometimes referred as torque components themselves.

2.4.4 Ferromagnetic resonance frequency

A method allowing to calculate the ferromagnetic resonance (FMR) frequency from a thermodynamic potential based on the equilibrium conditions was described by Smit and Beljers [58]. The ferromagnetic precession happens around extrema of the free energy density. Hence, the free energy density in the equations of motion of the magnetization vector (Eq. 2.39) can be developed around an equilibrium direction of the magnetization vector. For a small deviation from an equilibrium, the equations

of motions can then be written as

$$\begin{pmatrix} \dot{\vartheta} \\ \dot{\varphi} \end{pmatrix} = \frac{\gamma}{M_s \sin\vartheta} \begin{pmatrix} -f_{\vartheta\varphi} & -f_{\vartheta\vartheta} \\ f_{\varphi\varphi} & f_{\varphi\vartheta} \end{pmatrix} \begin{pmatrix} \vartheta \\ \varphi \end{pmatrix} \tag{2.40}$$

This system of linear differential equations can be solved by the ansatz $M_s(t) = M_s(0)e^{i\omega t}$. Plugging $M_s(t)$ in Eq. 2.40 and simplifying the result leads to a homogeneous system of linear equations

$$\begin{pmatrix} -f_{\vartheta\varphi} - \frac{i\omega M_s \sin\vartheta}{\gamma} & -f_{\vartheta\vartheta} \\ f_{\varphi\varphi} & f_{\varphi\vartheta} - \frac{i\omega M_s \sin\vartheta}{\gamma} \end{pmatrix} \begin{pmatrix} \vartheta \\ \varphi \end{pmatrix} = \begin{pmatrix} 0 \\ 0 \end{pmatrix} \tag{2.41}$$

that has non-trivial solutions only if the determinant of the matrix is zero:

$$\left(-f_{\vartheta\varphi} - \frac{i\omega M \sin\vartheta}{\gamma}\right)\left(f_{\varphi\vartheta} - \frac{i\omega M \sin\vartheta}{\gamma}\right) + f_{\vartheta\vartheta} f_{\varphi\varphi} = 0 \tag{2.42}$$

Solving for ω provides a formula for the ferromagnetic resonance frequency in spherical coordinates.

$$\omega = \frac{\gamma}{M \sin\vartheta} \sqrt{f_{\vartheta\vartheta} f_{\varphi\varphi} - f_{\vartheta\varphi}^2} \tag{2.43}$$

The Eq. 2.43 is not the most general formula for the ferromagnetic resonance frequency, as it can also be derived independent of a coordinate system, hence avoiding the singularity at $\vartheta = 0$. A symmetrical version of this equation in Cartesian coordinates was derived by Baselgia et al. [59].

2.4.5 Magnetoelastic coupling and free energy density of Pt/Co multilayers

The magnetocrystalline anisotropy discussed in Section 2.4.1 couples magnetic moments of the electrons to the crystal axes by means of the spin-orbit interaction. This coupling depends on the direction of the magnetization. Additionally, the exchange interaction, which does not depend on the direction of magnetization, leads to distance dependent energy contributions. This means that a change of magnetization can shift the minimum of the energy and create an additional strain in the material. This effect is known as magnetostriction. In return, applying strain to a crystal can lead to a change in the magnetic anisotropy. The shape anisotropy can also be affected by the strain due to its dependence on the shape of the crystal.

Pt/Co multilayer samples consist of fcc Co grains oriented with [111] axis parallel to the sample normal, while the other axes of the grains are randomly oriented in the film plane. It is schematically depicted in Fig. 2.8. An expression for the magnetoelastic energy density of a cubic system can be derived by expanding free energy density in similar fashion as the magnetic anisotropy in Eq. 2.28 [50].

$$f_{me}(T, \epsilon_1, \ldots, \epsilon_6) = B_1(T)(\epsilon_1\alpha_1^2 + \epsilon_2\alpha_2^2 + \epsilon_3\alpha_3^2) + B_2(T)(\epsilon_4\alpha_2\alpha_3 + \epsilon_5\alpha_1\alpha_3 + \epsilon_6\alpha_1\alpha_2) \tag{2.44}$$

where B_1, B_2 are magnetoelastic coupling constants and $\epsilon_1, \ldots, \epsilon_6$ are strain tensor components. Because of the symmetry of the strain tensor ϵ_{ij} its components are usually given in Voigt notation [60]:

$$\epsilon_{ij} = \begin{bmatrix} \epsilon_1 & \frac{1}{2}\epsilon_6 & \frac{1}{2}\epsilon_5 \\ \frac{1}{2}\epsilon_6 & \epsilon_2 & \frac{1}{2}\epsilon_4 \\ \frac{1}{2}\epsilon_5 & \frac{1}{2}\epsilon_4 & \epsilon_3 \end{bmatrix} \tag{2.45}$$

The shear strain components $\epsilon_4, \epsilon_5, \epsilon_6$ have an additional factor 2. The magnetoelastic coupling constants are temperature-dependent and can be different in thin films compared to the bulk materials [61].

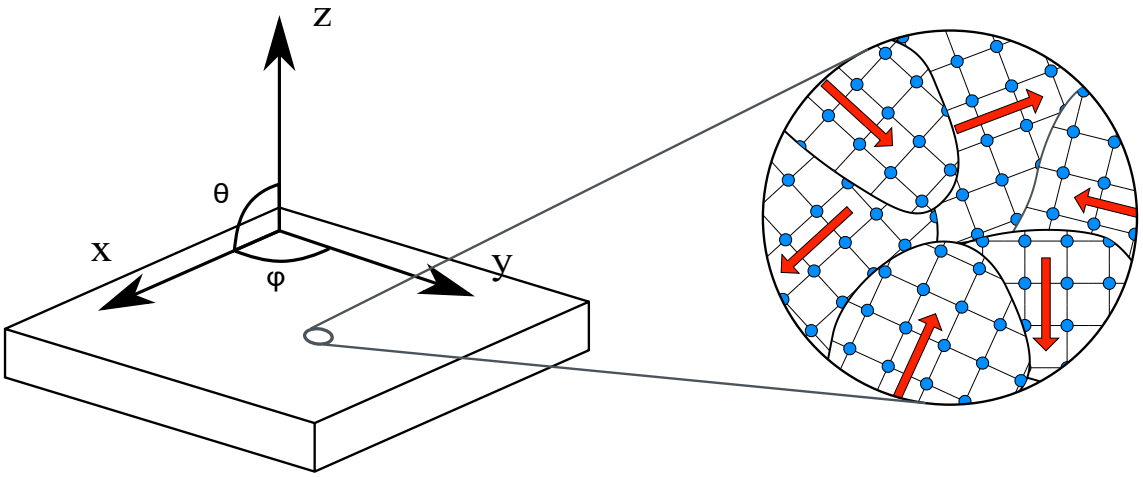

Figure 2.8: A Pt/Co multilayer structure with a random grain orientation in the sample plane. The [111] direction of the unit cell is parallel to the surface normal.

The total magnetoelastic contribution to the free energy density can be calculated by averaging over possible orientations of the grains in sample plane. However, since Eq. 2.44 is given with respect to the crystal axes rather than sample coordinate system, an additional transformation has to be performed to account for the [111]

orientation of the grains. Strain ϵ and magnetization $\mathbf{M}$ can be transformed from the sample coordinate system into the crystal coordinate system and rotated around the z-axis by an angle ψ using the following expressions:

$$\epsilon' = PR_z(\psi)\epsilon R_z^T(\psi)P^T, \qquad \mathbf{M}' = PR_z(\psi)\mathbf{M} \tag{2.46}$$

ϵ' and $\mathbf{M}'$ are strain and magnetization in crystal coordinate system. $R_z(\psi)$ is the rotation matrix around z-axis in sample coordinate system and P is the change of basis matrix that transforms the result into the crystal coordinate system.

$$P = \begin{pmatrix} -\frac{1}{\sqrt{2}} & -\frac{1}{\sqrt{6}} & \frac{1}{\sqrt{3}} \\ \frac{1}{\sqrt{2}} & -\frac{1}{\sqrt{6}} & \frac{1}{\sqrt{3}} \\ 0 & \sqrt{\frac{2}{3}} & \frac{1}{\sqrt{3}} \end{pmatrix}, \qquad R_z = \begin{pmatrix} \cos\psi & -\sin\psi & 0 \\ \sin\psi & \cos\psi & 0 \\ 0 & 0 & 1 \end{pmatrix} \tag{2.47}$$

Plugging results from the Eq. 2.46 in Eq. 2.44 and averaging over ψ yields an expression for the average magnetoelastic contribution to the free energy density $\bar{f}_{me}$:

$$\bar{f}_{me}(\vartheta, \varphi, \epsilon_1, \ldots, \epsilon_6) = \frac{1}{2\pi} \int_0^{2\pi} f_{me}(\vartheta, \varphi, \epsilon_1, \ldots, \epsilon_6, \psi) d\psi \tag{2.48}$$

The average of the free energy density still depends on the strain components $\epsilon_1, \ldots, \epsilon_6$ and magnetization orientation (ϑ, φ), but it does not depend on the grain orientation ψ.

Chapter 3

Strain as functional tool in thin films - selected applications

This chapter contains a selection of applications of laser-induced strain as a functional tool picked from research papers on which this thesis is based. The application of laser-induced strain as a mechanism for shortening of X-ray pulses at synchrotron facilities is described in Section 3.1. It is achieved by controlling the Bragg condition in a multilayer structure by pumping it with precisely timed ultrashort laser pulses. The method for time-resolved measurements of periodic surface displacement with sub-angstrom precision is presented in Section 3.2. It is based on the calculation of diffraction efficiency and modelling of laser-induced periodic surface displacements. Section 3.3 contains a concept and implementation of an experimental setup for a full temporal and spatial control of periodic surface displacements. It allows an independent control of laser-induced periodic surface displacements and its accompanying thermal grating. Laser-induced strain can induce magnetization precession in ferromagnetic materials. An analysis of heat and strain-based mechanisms for a strain-induced precession of magnetization in Pt/Co/Po multiplayer is summarized in Section 3.4.

3.1 Shortening of hard X-ray pulses at synchrotrons

Diffraction of X-rays from thin films structures opens a possibility to select and shape X-ray pulses utilizing an induced strain. Introducing strain to a diffraction layer on time-scales smaller than the pulse duration will modulate the intensity of the diffracted pulse by changing the Bragg condition. This happens because

for a given angle, the diffraction intensity depends on the lattice parameter, which in turn depends on the stain. A significant contrast between the intensity of a modulated and non-modulated X-ray pulse can be achieved in a proximity of the Bragg angle by an application of high amplitude strain waves. A strain pulse with a high amplitude and sharp rising edge can be induced by means of an excitation with a short laser pulse. For available laser systems, the pulse duration is usually much shorter than the X-ray pulse duration at synchrotron radiation facilities. The amplitude of such stain pulse is often limited only by material destruction threshold.

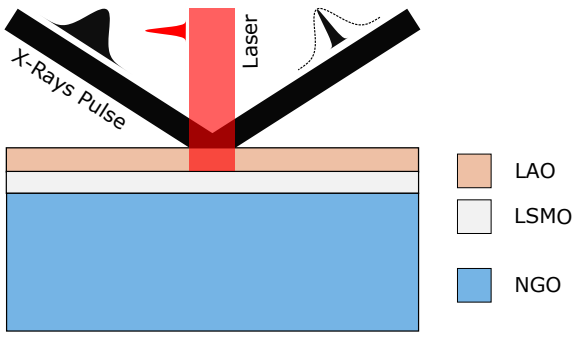

Figure 3.1: Structure of a multilayer device designed to reduce the X-ray pulse duration (PicoSwitch). The top layer is a dielectric LAO layer intended to diffract X-rays. The bottom layer is a metallic LSMO transducer layer designed to absorb laser pulses and launch a strain wave into the LAO layer. The NGO substrate is chosen to reduce a reflection of the sound wave at the LSMO-LAO interface. When the device is pumped by strong laser pulses, the strain waves in the LSMO layer propagate in the LAO layer, modulating the diffraction intensity of the X-ray pulses for a few picoseconds by modifying the lattice parameter.

Figure 3.1 shows a multilayer structure designed for reduction of X-ray pulse duration at synchrotron radiation facilities [62]. It consists of two functional layers on top of an NGO substrate. The upper dielectric LAO layer is transparent to the laser beam with the wavelength of 800 nm. The lower metallic LSMO layer is opaque and serves as a transducer. When the structure is pumped by a pulsed laser beam, laser pulses are absorbed by the LSMO layer, which gets rapidly heated and expands. The expansion wave in the LSMO layer leads to a compression wave in the LAO layer, propagating from the LSMO/LAO interface to the sample surface. Another compression wave propagates from the LSMO/NGO interface into the substrate, but is not of any particular interest. When the compression wave propagating in the LAO layer reaches the surface, it is reflected back as an expansion wave.

Figure 3.2 shows a simulation of the X-ray diffraction of the structure described

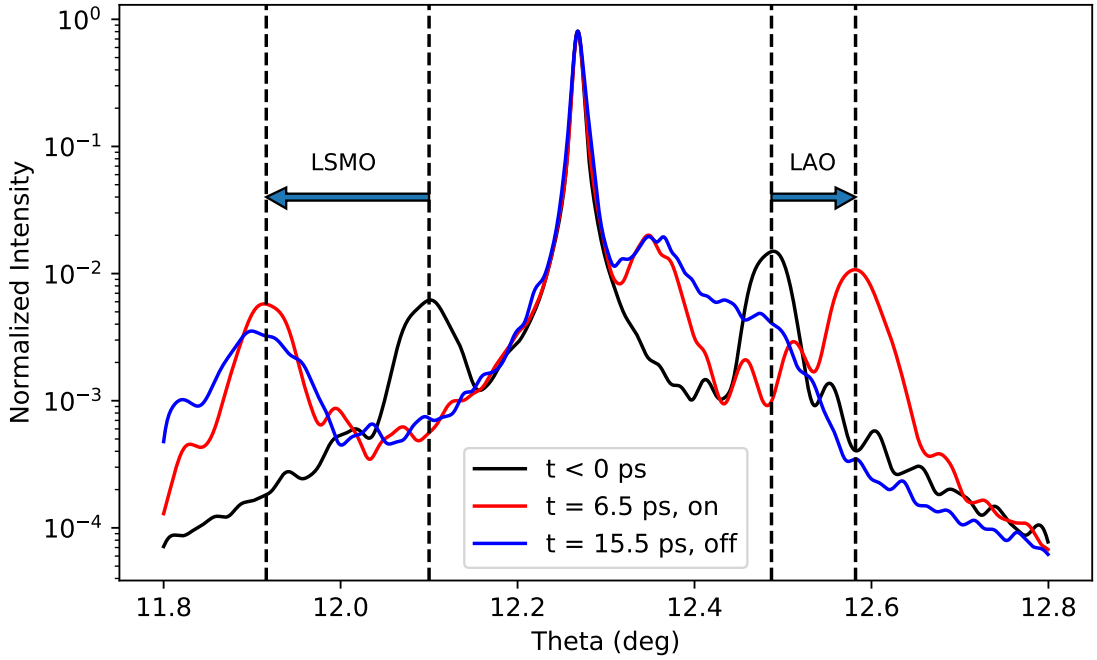

Figure 3.2: Simulation of X-ray diffraction from a LAO/LSMO/NGO multilayer structure. Parameters used in the simulation are: the X-ray beam energy of 14.85 keV, the laser pulse duration of 1 ps and the fluence of 30 mJ/cm^2. The LAO layer thickness is 101 nm and LSMO layer thickness 65 nm. The highest peak in the angle of 12.25° is the diffraction peak of the NGO substrate. The LSMO peak before the excitation with a laser pulse is at 12.1° and 6.5 ps after the excitation at 11.9°. The LAO peak before the excitation with a laser pulse is at 12.49° and 6.5 ps after the excitation at 12.58°. After the excitation, the LSMO peak is shifted to smaller angles since the LSMO layer expands after being heated by an absorption of the laser pulse. Unlike the LSMO peak, the LAO peak is shifted to higher angles because the expansion wave in the LSMO layer results in a compression wave in the LAO layer.

above. The diffraction intensity is normalized to the maximum of the NGO substrate peak at 12.25°. Before the excitation, the diffraction peak of the LAO layer is at 12.46° and LSMO layer at 12.1°. Around 6.5 ps after the excitation, the LSMO peak is shifted to the angle of 11.9° and LAO peak to the angle of 12.58°. Comparing the diffraction intensity from the LAO layer at the angle of 12.58° before the excitation with a laser pulse and 6.5 ps after the excitation, when it is at its maximum, gives an increase in intensity by a factor of 27. After 15.5 ps the compression wave reaches the sample surface and is reflected back as an expansion wave, reducing the diffraction intensity by a factor of 31. This results in a 9 ps window of the increased diffraction intensity triggered by a laser pulse. The angle of the sample can be tuned in such way, that it is slightly off the (002) peak of the LAO layer.

So that when the compression wave first passes through the top LAO layer, the Bragg condition is achieved and the diffraction intensity is at the maximum. The expansion wave returning from the sample surface restores the previous condition to a certain degree, reducing the diffraction intensity. This provides an X-ray switching mechanism capable of shortening X-ray pulses on the scale of several picoseconds.

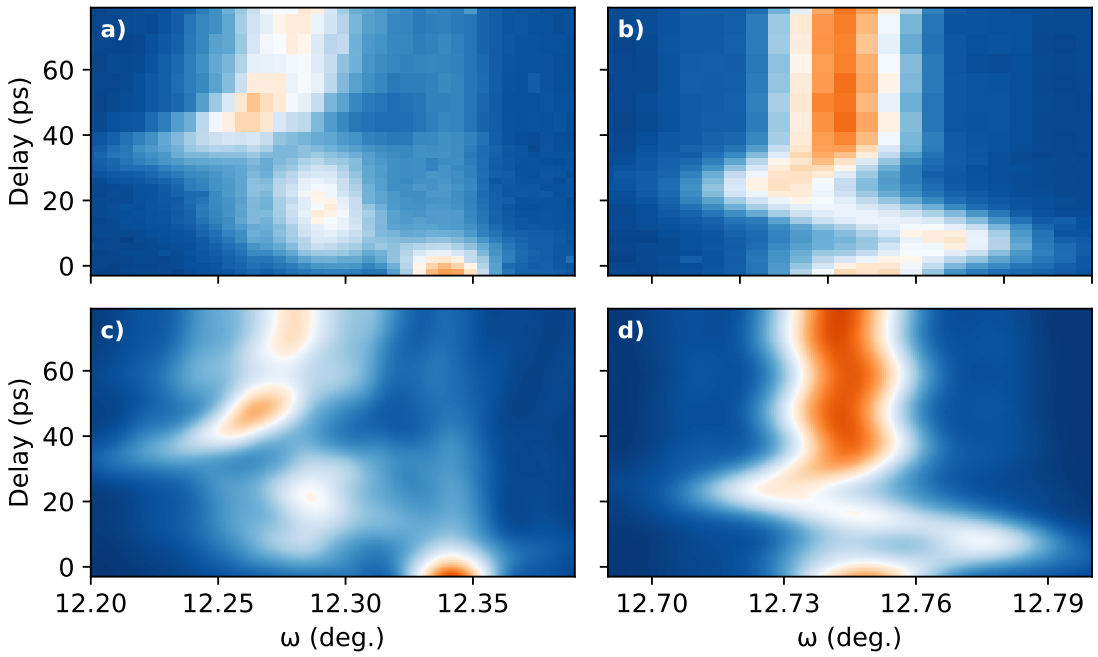

Figure 3.3: Experimental data acquired using time-resolved X-ray diffraction. A sound wave propagating in the a) LSMO layer and b) the LAO layer following an excitation with a laser pulse. Simulation of the sound wave propagation in c) LSMO, d) LAO layer convoluted with the instrument function.

Fig. 3.3 shows the experimental data acquired at ESRF ID09. The temporal resolution of the beamline was increased from approximately 120 ps to 7.5 ps using the Bragg switch described above. Subsequently, the shortened X-ray pulses were used to study the switching process in another Bragg switch. The images a) and b) show the time-resolved measurements for the LSMO and LAO peaks, respectively. Following an excitation, the LAO peak shifts to higher angles, reaching the maximum of its shift after around 10 ps. The images c) and d) show the corresponding simulation convoluted with the Gaussian distribution with $\sigma = 7.5$ ps. In experiments, the duration of X-ray pulses has been successfully shortened from 120 ps to 7.5 ps with a switching contrast of 33 relative to the initial value [62].
This method of X-ray pulse shaping comes with a cost of an overall decrease in number of photons. First, a reduction of the X-ray pulse duration itself reduces the

number of photons since the long pulse has naturally more photons than a short one, assuming the same intensity. Second, the diffraction from the thin top layer yields only a small number of photons compared to a direct beam or a diffraction from the substrate peak. The thickness of the top layer plays a major role in pulse shortening capabilities, since the switching time depends on the time that the strain wave takes to propagate through the top layer. Thus, it is always a trade-off of between the diffraction efficiency and the reduced pulse duration. The total contrast considering the diffraction efficiency and loses by the shortening of the pulse duration itself was calculated to be around 2.94 with the total efficiency of $1.8{\cdot}10^{-4}$. The repetition rate at which this switching mechanism can work is limited mainly by the accumulated heat. It was successfully shown that a similarly structured sample can switch X-ray with a repetition rate of up to 1 MHz [13, 62]. Other factors such as sample deterioration, surface distortion and residual effects might become a limiting factor at higher repetition rates.

3.2 Measurement of periodic sub-angstrom surface distortions

Transient Grating technique can be used to create periodic displacements, which in turn can be probed optically or with help of time-resolved XRR. The concepts behind TG and its applications were described in Section 2.2 and a basic experimental implementation in Section 2.2.2. It provides a method of exciting and probing structures on the nanoscale with a high temporal resolution, which can range from around 100 ps for typical time-resolved synchrotron setups to femtoseconds for optically probed setups using ultra-fast laser pulses. However, despite its excellent temporal properties, it is hard to measure the absolute value of the surface displacement. The induced surface displacement is typically below one nanometer, even for strong excitations near the damage threshold of most materials. This is much smaller than the spatial period of a laser induced transient grating, which is usually in the range of one to several micrometers for wavelengths used in near infra-red amplified ultra-fast pulsed lasers, such as amplified 800 nm Ti:Sapphire lasers. Furthermore, the surface displacement is a sum of displacements created by the localized heating of the surface (thermal grating) and induced acoustic waves (SAW and SSLW). The sum of displacements of due to the transient thermal grating and standing the acoustic wave is shown in Figure 3.4 a) and b). The surface displacement is depicted in orange, the thermal grating in red and the amplitude of the standing Rayleigh SAW wave in blue. Fig. 3.4 a) shows the surface displacement caused by the thermal

grating enhanced by the Rayleigh wave due to the positive interference and b) the decreased surface displacement caused by the negative interference of the thermal grating and the oscillating Rayleigh wave.

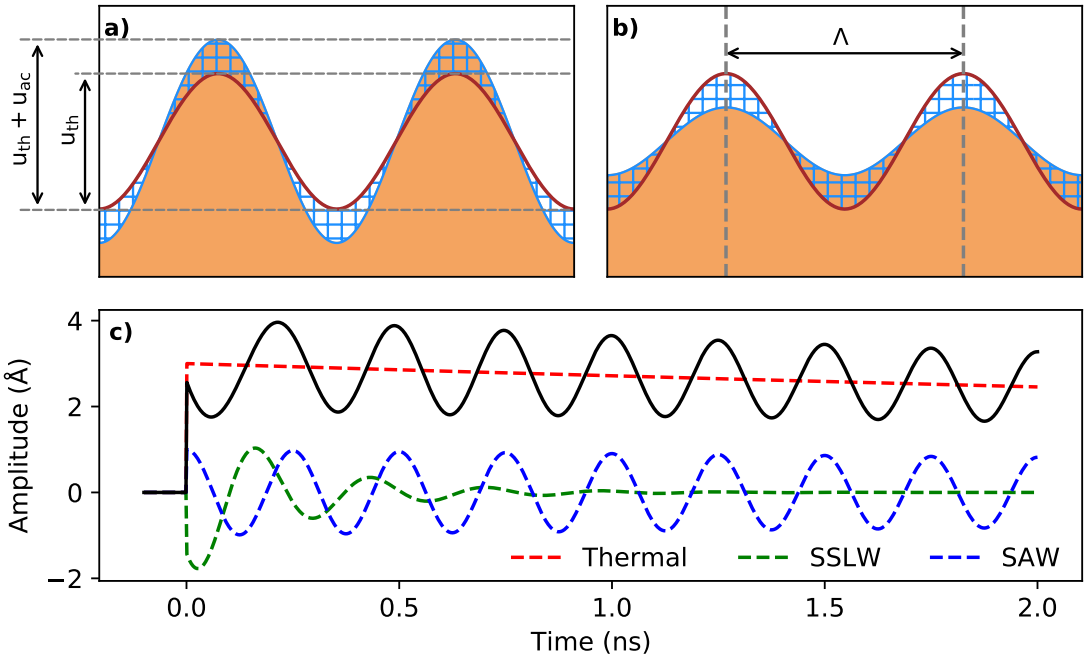

Figure 3.4: A surface displacement created as a result of a laser induced transient grating. The total surface displacement u is the sum of the displacement created by the heat from an absorbed laser pulse (transient thermal grating) u_{th} and induced acoustic waves (Rayleigh SAW, SSLW) u_{ac}. The thermal grating is shown in red. The amplitude of the acoustic wave is shown in blue. a) The acoustic wave interferes constructively with the thermal grating, increasing the surface displacement. b) The acoustic wave with phase shift of π, after a half of its oscillation period passed, overlapping with the persistent thermal grating decreasing the surface displacement. c) Modelled transient grating excitation using Eq. 3.1 showing the surface displacement as an overlap of the transient thermal grating, SAW and SSLW. The oscillation periods of SAW and SSLW are 250 ps and 270 ps, respectively. The decay time of the thermal transient grating is 10 ns.

The thermal grating decays on the timescale of hundreds of nanoseconds by the in-plane diffusion. For induced transient gratings with a period of a few micrometers, the created standing Rayleigh wave has an oscillation period of hundreds of picoseconds. However, it loses its energy on much longer scale of hundreds of nanoseconds (e.g., for STO with v = 7900 m/s and induced grating with period of $\Lambda = 2$ µm the oscillation period is $T = \Lambda/v = 253$ ps). Since the period of the standing Rayleigh wave is a factor of a thousand times smaller than the decay times of its amplitude

and the amplitude of the thermal grating, one can decouple the measurement of their displacements. In a simple case, it can be done by measuring the oscillating surface displacement when it reaches it minimum and maximum. The difference is than two times the amplitude of the Rayleigh wave. A better way is to model the surface displacement of the transient thermal grating by assuming an exponential decay, combined with a model for slowly decaying standing surface acoustic waves and fast decaying surface-skimming waves.

$$\begin{aligned} u(t) = u_{th}e^{-t/\tau_{th}} &+ u_{saw}e^{-t/\tau_{saw}}\sin(\omega_{saw}t + \phi_{saw}) \\ &+ u_{sslw}e^{-t/\tau_{sslw}}\sin(\omega_{sslw}t + \phi_{sslw}) \end{aligned} \tag{3.1}$$

with $\omega_{saw} = 2\pi/T_{saw}$, where T_{saw} is the oscillation period of the SAW, ϕ_{saw} its relative phase and τ_{saw} its decay time. Other parameters are used for the SSLW and the transient thermal grating in analogy with the parameters for the SAW. An excitation followed by an oscillating surface displacement modelled using Eq. 3.1 is shown in Fig 3.4 c). The total surface displacement is shown in black, the slowly decaying thermal displacement in red, the slowly decaying Rayleigh SAW in blue and fast decaying SSLW in green. The model can be expanded to be used for multiple SAW modes and more complicated decay processes e.g., in multilayer systems.

The absolute value of of surface displacement can be obtained by analyzing the dependence of the diffraction efficiency on the amplitude of the surface displacement. The diffraction efficiency of a sinusoidal phase grating was described in Section 2.3.1. For for the +1 diffraction order and small displacements it can be calculated as $\eta = |J_1(\Delta\phi)|^2$, where $\eta = I/I_0$ can be measured directly by measuring the intensity of diffracted and incident beams I and I_0, respectively. The phase difference $\Delta\phi$ is given by the Eq. 2.15 and depicted in Fig. 2.5 (top):

$$\Delta\phi = \frac{\pi u}{\lambda}(\cos\alpha_i + \cos\alpha_f) = -\pi\alpha_i\frac{u}{\lambda}\left[1 + \sqrt{1 + 2n\frac{\lambda}{\Lambda\alpha_i^2}}\right] \tag{3.2}$$

with u being the surface displacement, Λ the spatial phase grating period, n the diffraction order and λ the wavelength of the diffracted beam. The angles α_i and α_f are the incidence and diffraction angle, respectively. The right side of Eq. 3.2 can be obtained by developing $\cos\alpha_f$ and expressing it through the incidence angle α_i and the momentum transfer $\pm 2\pi/\Lambda$. Alternatively, it can be derived from geometrical considerations [63].

Figure 3.5 shows the diffraction efficiency of the first order of diffraction from an induced transient grating with spatial periods of 1, 2 and 4 nm. The values for the

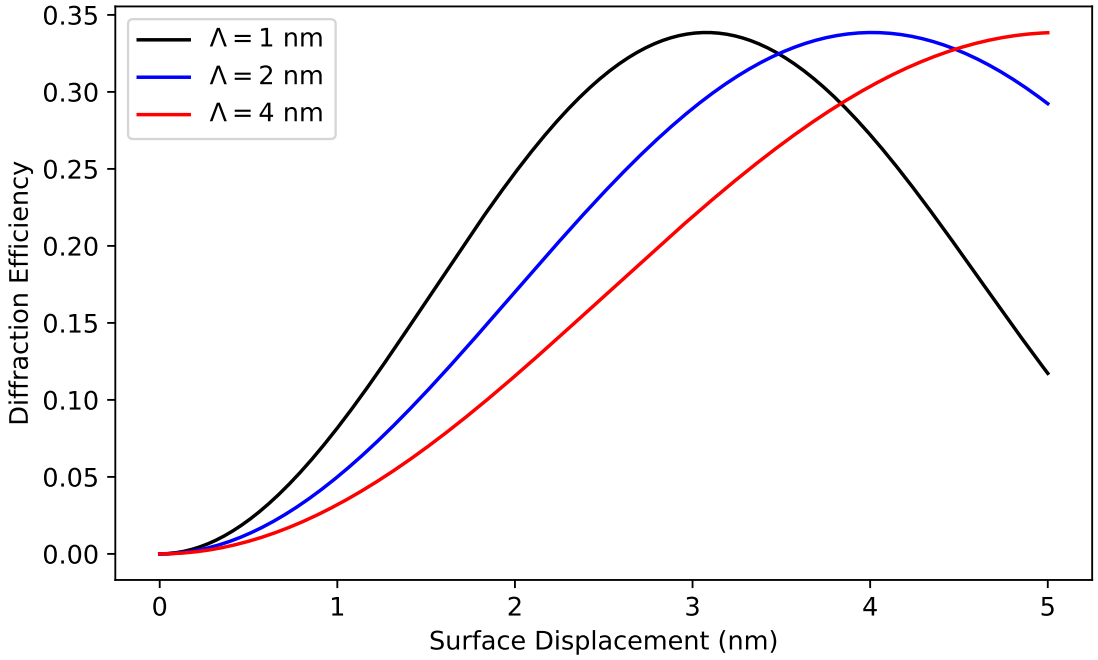

Figure 3.5: Dependence of the first order diffraction efficiency of an induced transient grating on the surface displacement calculated using Eq. 2.16 and 3.2. Calculation is done for grating with spatial periods of 1, 2 and 4 nm. The wavelength of the diffracted beam is 0.08266 nm and the incidence angle is 0.15°. The maximum of the diffraction efficiency is approximately 33%. The surface displacement can be obtained by comparing an experimentally measured diffraction efficiency with the model.

wavelength and incidence angle are 0.08266 nm and 0.15°, respectively. Comparing an experimentally obtained data with the model yields absolute value of the surface displacement. The calibration can be achieved by making a sequence of measurements with a varying fluence. From a simple consideration, one can derive that the surface displacement u is proportional to the fluence F of the exciting beam

$$u = \Delta L = \alpha \Delta T L = \frac{\alpha \Delta U L}{cV} = \frac{\alpha F A L}{cAL} = F\frac{\alpha}{c} \propto F \tag{3.3}$$

assuming $\Delta L/L = \alpha \Delta T$ and $\Delta U = cV\Delta T$ with α being thermal expansion coefficient and the heat capacity per volume $V = A \cdot L$ of the sample material. More precise derivation using an arbitrary heat distribution, e.g., $T(z) = T_0 e^{-z/\lambda}$ leads to the same result due to additivity of material expansions from different depths.

3.3 Spatiotemporal control of periodic surface distortions

Transient grating excitation by ultra-short laser pulses can be used to create standing and propagating acoustic waves. An application of multiple subsequent excitations can be used to control an excited standing Rayleigh SAW by means of the interference. Depending on the relative phase of the subsequent pulses, the amplitude of the acoustic wave can be amplified or extinguished. Furthermore, a laser induced TG excitation inevitably creates a thermal transient grating containing most of the exciting pulses energy. The transient thermal grating can also be controlled by an introduction of a spatial phase shift to the subsequently induced transient grating. Both, the acoustic wave and the thermal grating can be controlled independently, which could open many new possibilities to selectively excite and probe solids and nanostructures with high temporal and spatial precision.

A transient grating excitation with a single pulse is described in Section 2.2. Equations 2.4 and 2.5 describe the surface displacement caused by the transient thermal grating and the amplitude of the standing acoustic wave, respectively. The total surface displacement $u(x,t)$ created by two excitation pulses with a delay τ between pulses can be written as

$$u(x,t) = H(t)[u_{th,1}(x,t) + u_{ac,1}(x,t)] + H(t-\tau)[u_{th,2}(x,t-\tau) + u_{ac,2}(x,t-\tau)] \tag{3.4}$$

with $H(t)$ being the Heaviside function to model the sharp rise time, which is usually much slower than the oscillation period of the acoustic wave. In general, both excitation pulses do not have to have the same intensity. However, assuming that the amplitude of the acoustic wave does not decrease on the timescale of the measurement significantly, the displacement due to the thermal grating and the acoustic wave can be given as

$$u_{th}(x,t) = \frac{u_{th,1}}{2} e^{-\alpha_x q_\parallel^2 t}(1 + \sin(q_\parallel x)) + \frac{u_{th,2}}{2} e^{-\alpha_x q_\parallel^2 (t-\tau)}(1 + \sin(q_\parallel x - \phi_x)) \tag{3.5}$$

$$u_{\mathrm{ac}}(x,t) = u_{ac,1} \sin(q_\parallel x)\cos(\omega t) + u_{ac,2} \sin(q_\parallel x - \phi_x)\cos(\omega t - \phi_t) \tag{3.6}$$

where $q_\parallel = 2\pi/\Lambda$ is the momentum transfer by diffraction from the grating with Λ being the spatial transient grating period. The temporal phase shift $\phi_t = \omega\tau = 2\pi\tau/T$ is a result of the delay τ between the initial and second excitation pulse with T being the oscillation period of the acoustic wave. The spatial phase ϕ_x does not

depend on the delay τ, meaning that the amplitude of the acoustic wave depends on both spatial phase ϕ_x and temporal phase ϕ_t, but the surface displacement caused by the transient thermal grating depends only on the spatial phase ϕ_x. Thus, the transient thermal grating can not be extinguished by means of the delay between excitation pulses and has to be controlled by different means.

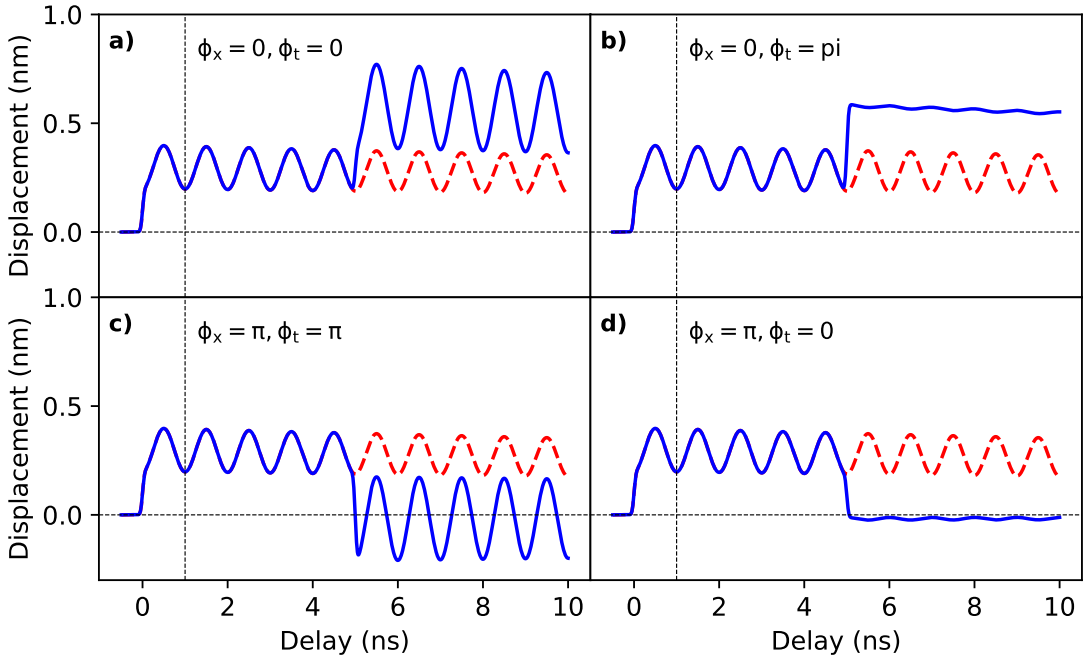

Figure 3.6: Modelled two pulse transient grating excitation with variable spatial and temporal phase based on Eq. 3.5 and 3.6. Acoustic wave oscillation period is 1 ns, the delay between two pulses is 1 ns, decay times of the transient thermal grating and the acoustic wave are both 80 ns. An initial excitation creates a thermal grating and induces a standing acoustic wave. a) Second excitation with the same spatial and temporal phase amplifies the amplitude of the thermal grating and the acoustic wave. b) The spatial phase of the second excitation is the same, but the temporal phase is shifted by π. This results in an increased amplitude of the thermal grating, but extinguishes the acoustic wave. c) The spatial phase and the temporal phases are shifted by π, leading to the removal of the thermal grating and amplification of the standing acoustic wave. d) The spatial phase is shifted by π, but the temporal phase is the same as one of the initial excitation, resulting in removal of the thermal grating and extinguishing the acoustic wave.

Most interesting cases of multi pulse TG excitation are obtained when ϕ_x and ϕ_t are either $2\pi n$ or $2\pi(n+1)$ with $n \in \mathbb{N}_0$ as in such special cases either the acoustic wave or the thermal grating interfere independently constructively or destructively. All four cases are depicted in Figure 3.6 and summarized in the Table 3.1. The phase is reduced to values of 0 and π.

	spatial ϕ_x	temporal ϕ_t	thermal ϕ_{th}	acoustic ϕ_{ac}
Case A	0	0	0	0
Case B	0	π	0	π
Case C	π	π	π	0
Case D	π	0	π	0

Table 3.1: Four special cases of possible spatial and temporal phase variations with resulting equivalent phases of the transient thermal grating and the standing acoustic wave. Phase shifts are limited to the interval $[0, 2\pi]$

Assuming the initial excitation pulse has the temporal and spatial phase of zero, and the decay time much longer than the delay between excitation pulses. In Cases A, the spatial phase and temporal phase of the second excitation pulse are the same as of the initial excitation pulse ($2\pi n \equiv 0$). Amplitudes of the thermal transient grating and the acoustic wave are doubled. This case can be used to ramp up the amplitude of the standing acoustic wave using multiple subsequent laser pulses, if the amplified transient thermal grating is also acceptable in the context of the experiment. In Case B, the spatial phase does not change, but the temporal phase is shifted by $2\pi(n+1) \equiv \pi$. The amplitude of the thermal transient grating is doubled, the acoustic wave, however, is extinguished. This case allows controlling the duration of the standing acoustic wave. In case of laser pulses with different intensity, it also allows decreasing the amplitude of the acoustic wave on short timescales. In both cases A and B the transient thermal grating is present and amplified as a by-product of the control exerted on standing surface waves. In Case C, both temporal phase and spatial phase are shifted by π. This leads to the destructive interference for the transient thermal grating and simultaneously amplified standing acoustic wave. This case allows the creation of standing acoustic waves by an ultra-short laser pulses without the accompanying thermal grating. However, despite the thermal grating being removed, the absorbed heat of both laser pulses is still present in the sample. In Case D, only the spatial phase is shifted by π, resulting in the extinction of both the transient thermal grating and the standing acoustic wave. If probing is done by measuring the intensity of the first diffraction, no signal will be observed after the second excitation pulse. Finally, more than two pulses can be used to achieve a combined effect of a full spatio-temporal control of surface deformations.

Figure 3.7 shows an experimental setup capable of producing two laser pulse excitations with spatial and temporal phase control. First, the beam passes a Michelson interferometer setup with adjustable positions of mirrors M1 and M2. The laser pulse is split using a polarizing beam splitter in two pulses with different polarization. The split ratio is controlled by a half-wave plate placed before the beam splitter. Both

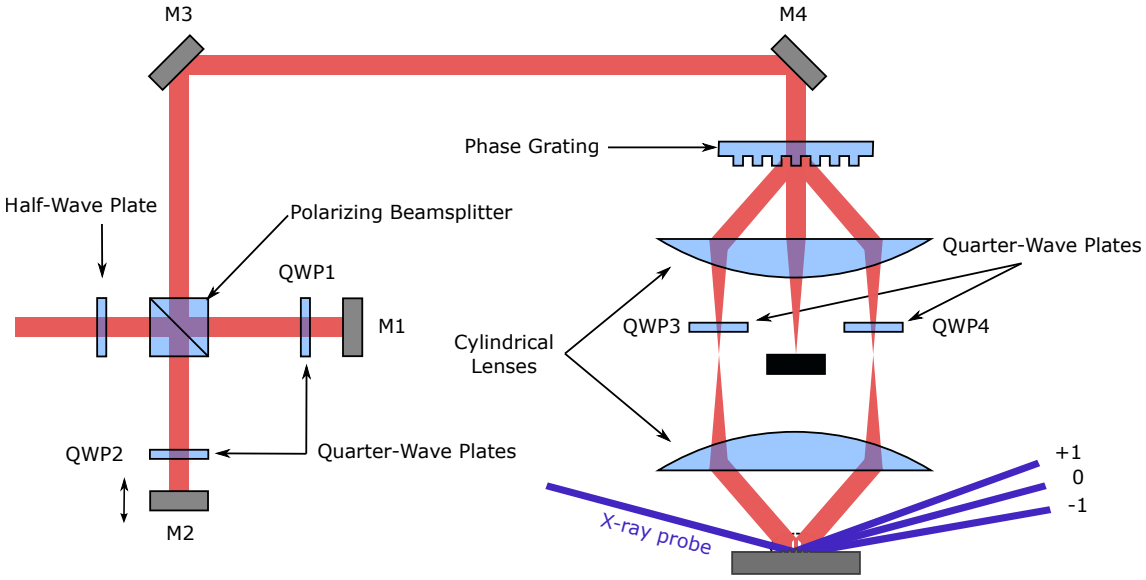

Figure 3.7: Transient grating setup with ability to control spatial and temporal phase of the induced transient grating. The setup uses two ultra-short laser pulses of perpendicular polarization to excite the sample. The beam is split in two by a Michelson interferometer setup with a variable intensity control. The delay between pulses is controlled by the mirror M1 positioned on a translation stage. The spatial phase of the induced transient grating is controlled by the relative angle of two quarter-wave plates QWP3 and QWP4. The sample can be probed either optically or using X-rays.

beams pass through quarter-wave plates QWP1 and QWP2 before being reflected back by mirrors M1 and M2. Quarter-wave plates QWP1 and QWP2 create a total rotation of the polarization by 90° for each beam. Thereafter, the beam is directed to the usual transient grating setup described in Section 2.2 with addition of two tunable quarter-wave plates QWP3 and QWP4 in both first order diffracted beams coming from the phase grating. The temporal phase can be controlled using the delay between both excitation pulses. The temporal delay for the four cases described above can be achieved by setting the delay to be $\tau = nT/2$ resulting in temporal phase $\phi_t = \pi n$. The spatial phase can be controlled by changing the relative angle of the quarter-wave plates QWP3 and QWP4. If the the axes of quarter-wave plates QWP3 and QWP4 are parallel, the spatial phase delay ϕ_x is zero. However, if the axes of both are perpendicular to each other, each induced transient grating is shifted spatially by $\pm\pi/2$, resulting in total spatial phase shift of $\phi_x = \pi$. Thus, both the temporal and the spatial phase can be controlled independently.

3.4 Strain-induced magnetization dynamics

Laser-induced changes of the magnetization direction can be achieved by a variety of different methods, such as ultrafast demagnetization, nonthermal optomagnetic effects and optical switching [64–70]. One of the ways to achieve it, is to use an ultrashort laser pulse to create a strain pulse, which in turn launches a magnetic precession [71]. A detailed description of FMR driven by a surface acoustic wave was given by Dreher et al. [72] and precession magnetization switching by Thevenard et al. [73]. This section contains a discussion of the excitation mechanism of FMR in Pt/Co multilayer samples.

3.4.1 Sample and Geometry

The sample consist of substrate, texture layer, stack and capping layer. Its structure is shown in Fig. 3.8. The texture layer is a 6 nm Pt layer on the SiO_2 substrate and is designed to give upper layers a defined growth pattern. On the top of the texture layer is a stack of 6x alternating 2 nm Co and 1 nm Pt layers. On the top of the sample is a protective 3 nm Pt cap layer that protects the sample from oxidation. In-plane, the sample is composed of randomly oriented grains with different orientation of magnetization. The total magnetization without an external magnetic field near zero with an easy plane oriented perpendicular to the surface normal. The samples were created and characterized by J. Wagner [74].

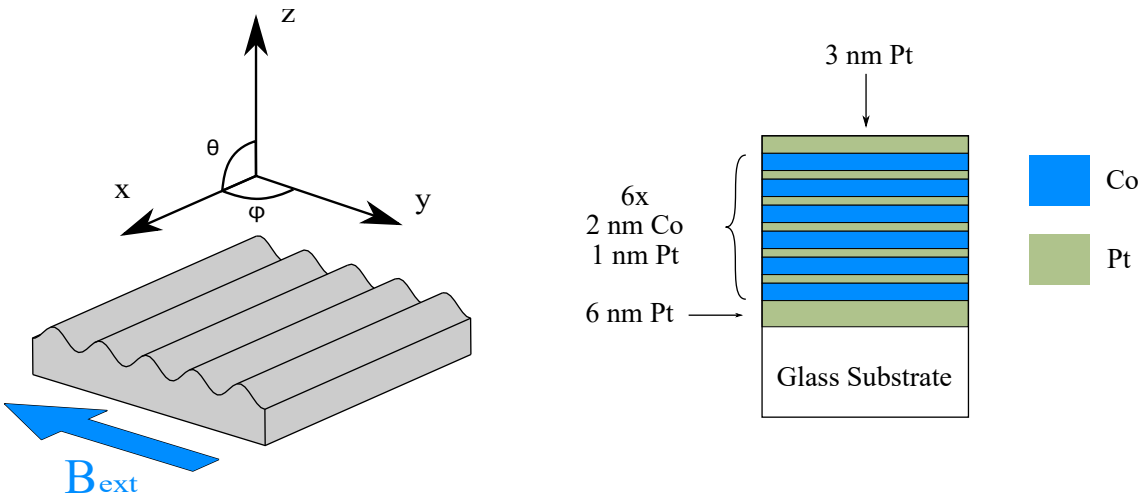

Figure 3.8: (left) Coordinate system. The sample normal is parallel to the z-axis. The magnetic field and k-vector of the transient grating excitation are aligned along the y-axis. (right) Sample structure. The sample consists of a 6 nm Pt texture layer on the glass substrate, a stack of 6 times 1 nm Pt / 2 nm Co layers and a protective 3 nm Pt top layer.

The coordinate system is chosen in such a way that the sample normal is along the z-axis. An external magnetic field is applied along the y-axis, and the k-vector of an induced transient grating excitation is also parallel to the y-axis. In spherical coordinates, the standard definitions are applied (Fig. 3.8).

Experimental geometry

A schematic depiction of the experimental geometry is shown in Fig 3.9. The sample is pumped by two amplified femtosecond laser pulses with the wavelength of 400 nm. Both pulses overlap on the sample surface, exciting a thermal grating and launching strain waves in the sample. The sample is subsequently probed by a variably delayed 800 nm probe pulse. The probe pulse passes through the sample and is then redirected onto a Wollaston prism. The Wollaston prism splits the probe beam in two polarized beams with an orthogonal polarization. After exiting the Wollaston prism, the difference in the intensities of both pulses is measured by a balanced photodetector. A variable magnetic field up to 60 mT is applied parallel to the k-vector of the excited transient grating.

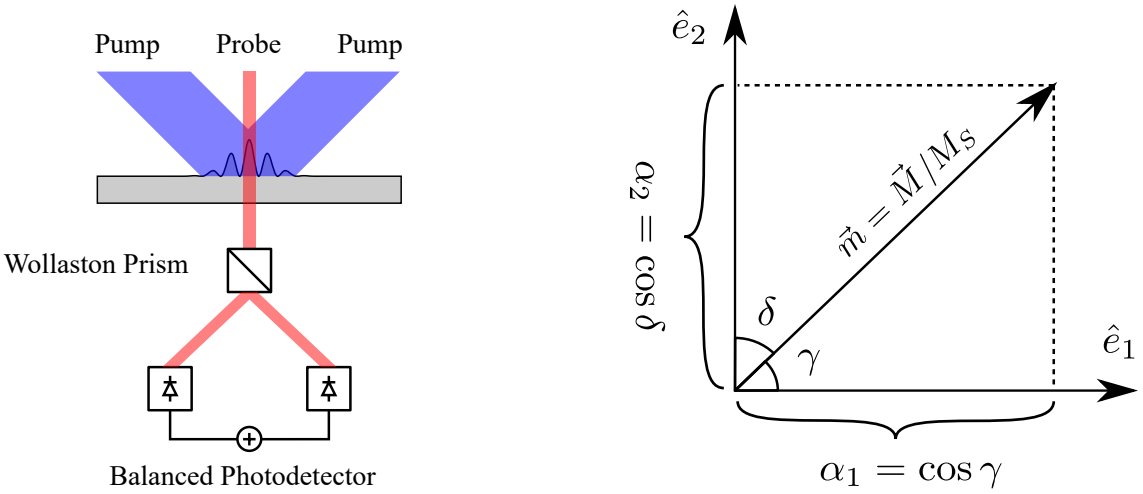

Figure 3.9: (left) Experimental geometry. The sample is pumped by two 400 nm pump pulses and probed by an 800 nm probe pulses. The pump pulses overlap and generate a transient grating on the sample surface. The probe pulse is split by a Wollaston prism in its polarization components. A balanced detector measured the intensity difference between both orthogonally polarized probe beams. (right) Directional cosines α_i are components of the magnetization direction $\mathbf{m} = \mathbf{M}/M_S$ along the crystal axes $\hat{\mathbf{e}}_\mathbf{i}$. (In general, they are projections of a unit vector $\hat{\mathbf{u}}$ on the coordinate system axes $\alpha_i = \mathbf{u} \cdot \hat{\mathbf{e}}_\mathbf{i}$)

3.4.2 Strain-induced precession of the magnetization

Ultrashort laser pulses can create strain in the sample by rapid heating of the sample surface. The induced strain can in turn have effect on the orientation of the magnetization in the sample by means of magnetoelastic coupling, discussed in Section 2.4.5. This happens due to the positional shift of the free energy density minimum of the system. The magnetization vector tries to orient itself in such a way that energy is minimized, which results in the precession of the magnetization. The precession happens around the energy minima, in the ideal case on the lines of constant energy. However, in real systems it decays towards the energy minimum as the system loses its energy.

Using experimental geometry described in Section 3.4.1 and neglecting angle-independent terms, the free energy density of the system can be given by combining Eq. 2.31 and Eq. 2.48:

$$f(\vartheta, \varphi, \epsilon_1, \ldots, \epsilon_6) = -B_y M_S \sin\vartheta \sin\varphi + K_{1,eff} \sin^2\vartheta + \bar{f}_{me}(\vartheta, \varphi, \epsilon_1, \ldots, \epsilon_6). \quad (3.7)$$

where the first term is the Zeeman energy density $\mathbf{B}_{\text{ext}} \cdot \mathbf{M}$ with the external field B_y pointing in y-direction and the projection of the magnetization vector on the y-axis in spherical coordinates. The second term is the contribution of the uniaxial anisotropy and third term is the magnetoelastic contribution to the free energy density. The dynamic of the magnetization vector can be describer using Landau-Lifshitz equation in spherical coordinates.

$$\frac{\partial\varphi}{\partial t} = \frac{\gamma}{M_S \sin\vartheta} \frac{\partial f}{\partial\vartheta}, \qquad \frac{\partial\vartheta}{\partial t} = -\frac{\gamma}{M_S \sin\vartheta} \frac{\partial f}{\partial\varphi} \ . \quad (3.8)$$

which can be derived from Landau-Lifshitz equation $\dot{\mathbf{M}} = -\gamma \mathbf{M} \times \mathbf{B}_{\text{eff}}$ using effective magnetic field $\mathbf{B}_{\text{eff}} = -\nabla_M f$ as described in Section 2.4.3. The change of free energy density in ϑ leads to the torque component in φ and vice versa. Free energy density $f(\vartheta, \varphi)$ with no strain applied is shown in Fig. 3.10 (top). It has a minimum for magnetization orientation $\vartheta = \varphi = 90°$ due to the negative value of the effective anisotropy constant $K_{1,eff} = -0.4\ MJ/m^3$ keeping the magnetization in-plane and an external magnetic field $B_y = 50\ mT$ pointing along the y-axis.

In perfect equilibrium, applying strain ϵ_1, ϵ_2 and ϵ_3 does not lead to the shift of the free energy minima and subsequent excitation of the precession. This is the case because ϵ_2 coincides with the direction of the magnetization in the equilibrium, while

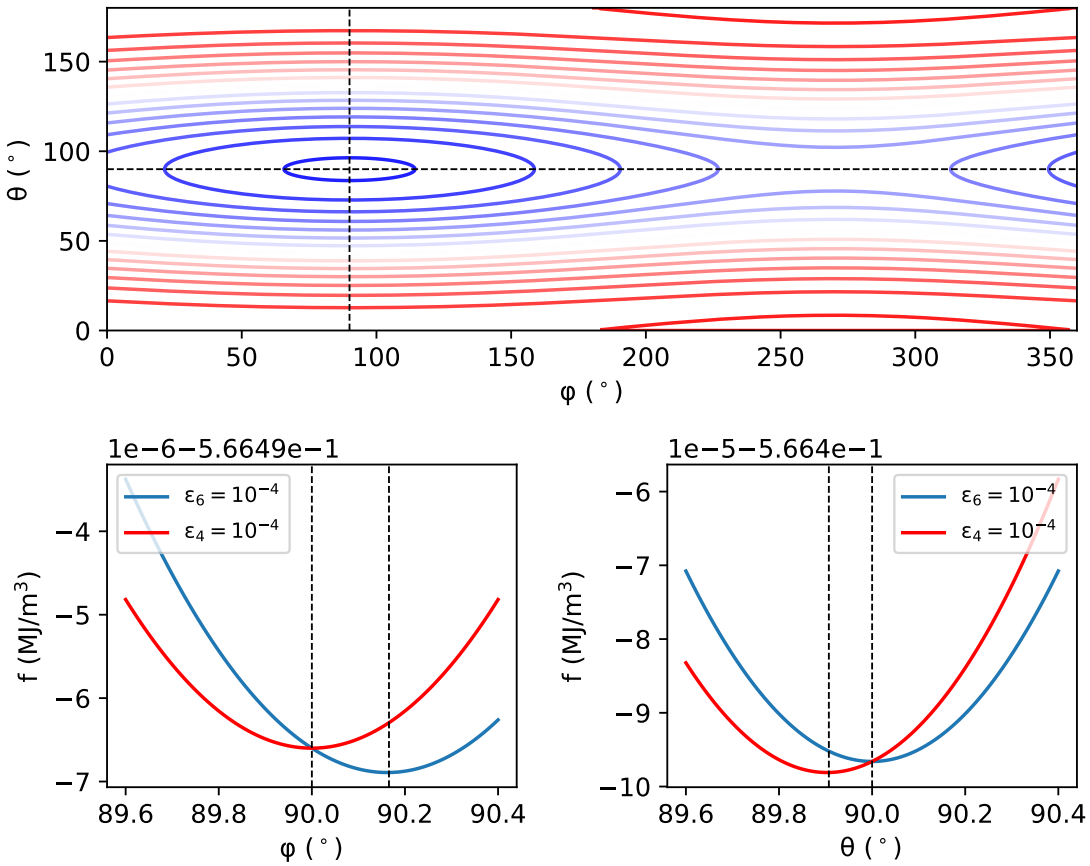

Figure 3.10: (top) Free energy density as function of magnetization orientation (Eq. 3.7). The magnetization vector lies in the sample surface plane due to the dominating contribution of the shape anisotropy and is pointing along the y-axis due to the applied external field. The equilibrium position $\vartheta = \varphi = 90°$ is marked with dashed lines. (bottom) Free energy density as function of φ (left) and ϑ (right) for applied shear strains $\epsilon_6 = 10^{-4}$ and $\epsilon_4 = 10^{-4}$. Applying shear strains ϵ_6, ϵ_4 leads to the shift of the free energy density minimum.

ϵ_1 and ϵ_3 are perpendicular to it. However, if the strain is high enough (approx. 10^{-2}) it can overcome an external magnetic, field turning a stable equilibrium in labile one. For similar reason, the shear strain component ϵ_5 (equivalent $2\epsilon_{xz}$) cannot start the precession on its own. On the other hand, the strain components ϵ_4 and ϵ_6 are able to shift the free energy density minimum and apply ϑ and φ torque components, respectively. A shift of the free energy density minimum applying ϵ_4 and ϵ_6 strain components is shown in Fig. 3.10 bottom left and right. If stain components ϵ_4 and ϵ_6 are present, the system loses its symmetry about y-axis and the typically much stronger stain components ϵ_1, ϵ_2 and ϵ_3 can induce the precession.

3.4.3 Heat-induced precession excitation

One of the possible mechanisms for excitation of FMR (Ferromagnetic Resonance) is a sudden change of the easy axis of the magnetization as a result of the temperature jump induced by an absorption of a laser pulse. The reason for the change of an easy axis is the change of the sign of the effective anisotropy constant, as described in Section 2.4.1. However, an analysis of this excitation mechanism requires the knowledge of the time-dependence of the effective anisotropy constant. Since the effective anisotropy constant depends on the saturation magnetization, the Eq. 2.32 can be used to calculate the magnetization if the temperature is known. The temperature can be obtained from simulations using scientific software called udkm1Dsim toolbox [75]. It provides an implementation of N-Temperatures model including temporal pulse shape, sample structure and heat diffusion.

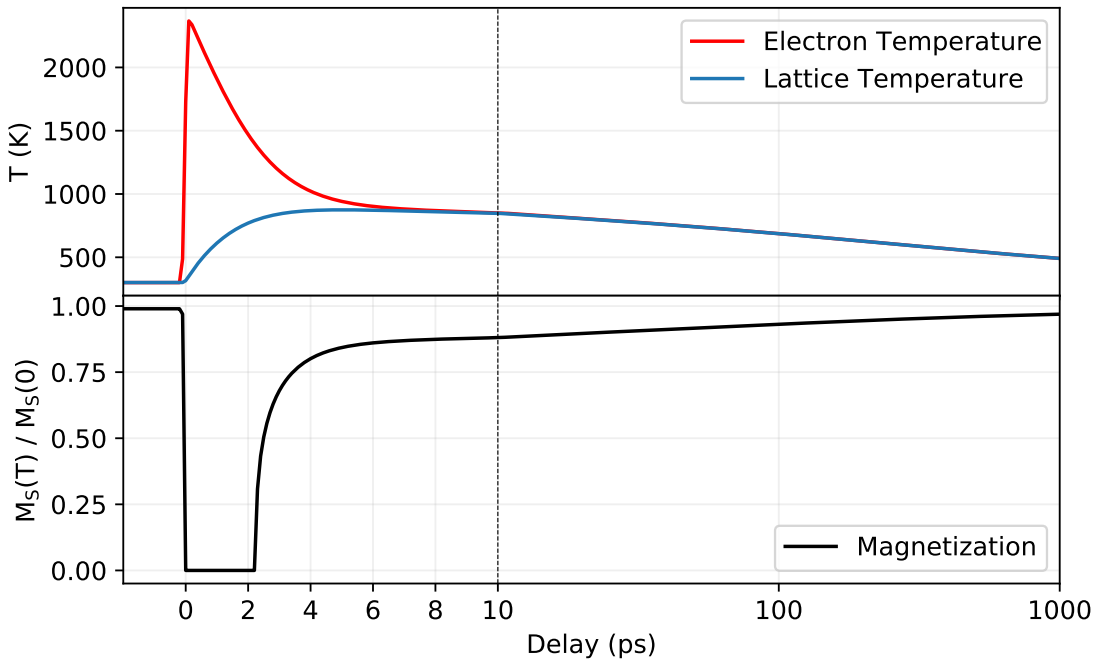

Figure 3.11: Simulation of an excitation of Pt/Co multilayer sample with a single laser pulse. The excitation fluence is 6.2 mJ/cm2. The pulse is absorbed on the sample surface with a penetration depth of around 15 nm. After the excitation, the electron temperature rises above the Curie temperature and the sample is demagnetized. After around 2 ps the temperature has decreased below the Curie temperature and after around 5 ps approximately 80 % of the initial magnetization is restored. The last 20 % of the magnetization are restored as the sample surface is cooling down due to the heat diffusion.

The simulation results of a single pulse excitation of the Pt/Co multilayer samples are shown in Fig. 3.11. The simulation is done for an absorbed fluence of 6.2

mJ/cm^2 used in the experiment. After an excitation with a laser pulse and reaching of the thermodynamic equilibrium, a distinct temperature can be assigned to the excited electrons. The temperature of the excited electrons is plotted in red. The electrons exchange energy with the lattice via electron-phonon coupling, resulting in the rise of the lattice temperature (shown in blue) and drop of electron temperature. After about 5 ps, the electrons and the lattice reach the same temperature, which is then decreasing on the timescale of nanoseconds as the heat is spreading into the sample from its surface. Since the initial temperature of the electrons after an excitation is above the Curie temperature in fcc Co the sample is completely demagnetized. This state lasts around 2 ps, after which the temperature of the excited electrons drops below the Curie temperature. After around 5 ps, the magnetization is restored to around 80 % of its initial value and keeps increasing as the temperature of the sample decreases.

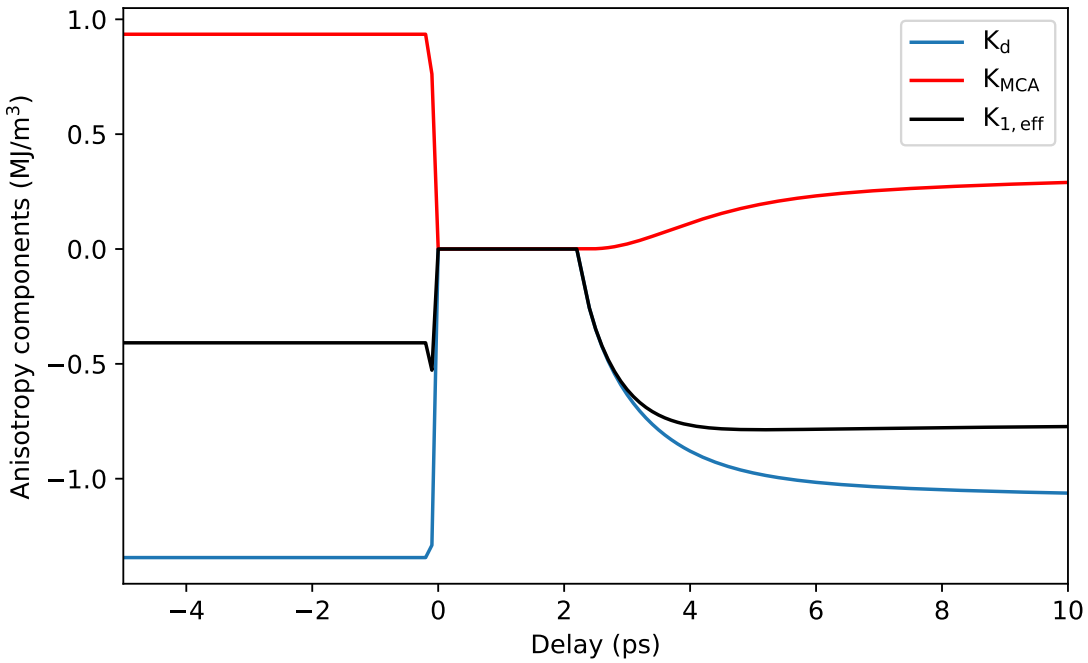

Figure 3.12: Effective anisotropy constant and its parts as a function of temperature for Pt/Co multilayer sample excited with a single 6.2 mJ/cm^2 laser pulse. The shape anisotropy provides a positive contribution, plotted in red. The magnetocrystalline anisotropy (volume and surface) provides a negative contribution and is plotted in blue. The effective anisotropy constant is the sum of all parts and is plotted in black. When the sample is heated by a laser pulse the sign of the effective anisotropy does not change due to the fast growth rate of the dominant surface anisotropy.

The time dependence of the effective anisotropy constant can be calculated using the knowledge of the saturation magnetization as a function of time obtained

from the simulations. Plugging the result of the simulation in Eq. 2.33 provides the necessary temperature dependence of the parts of the effective anisotropy constant plotted in Fig 3.12. As given by the Eq. 2.31 the effective anisotropy constant is a sum of the parts of magnetocrystalline and shape anisotropies. The magnetocrystalline anisotropy contribution consists of volume and surface contributions, although the volume contribution is only around 0.22 mJ/cm^2 for the given sample. The surface anisotropy provides the highest contribution to the effective anisotropy constant and is responsible for the in-plane orientation of the easy axis. When the sample is heated by a laser pulse above the Curie temperature, both magnetocrystalline and shape anisotropies disappear. For fcc Co the magnetocrystalline anisotropy depends on the 10th power of the saturation magnetization while the shape anisotropy on the 2nd power only. This means that the volume and surface anisotropies decrease faster than the shape anisotropy with increasing temperature and increase faster with decreasing temperature. However, since in the moment of the excitation the electrons follow the strong electric field of the exciting pulse, the magnetization as such cannot be properly defined. After the electron temperature decreased below the Curie temperature, the surface anisotropy is again the most dominant part of the effective anisotropy constant, as it has higher growth rate than the shape anisotropy. Overall, it can be assumed that the sign of the effective anisotropy constant does not change when the Pt/Co multilayer samples with negative effective anisotropy constant at room temperature are rapidly heated by a single pulse. Suggesting that the heating of the sample cannot be the primary mechanism for excitation of FMR for analyzed the samples.

Chapter 4

Summary

This thesis discusses applications of laser-induced strain as a functional tool in thin films and nanostructures. This includes development of both experimental and analytical methods, based on experiments conducted at synchrotrons and tabletop experimental setups. Based on the physical principles and experimental techniques discussed in Chapter 2, the following underlying physics and experimental techniques were presented in Chapter 3:

- An implementation and study of a new generation of Bragg switch devices, allowing a shortening of X-ray pulses at synchrotron facilities. Using a dedicated layer for absorption of the stain-generating laser pulse and a separate X-ray switching layer resulted in increased contrast due to reduction of thermal background and significantly increased repeatability rate up to 1 MHz. Under optimal conditions, such Bragg switches can sustain a flux of more than 10^9 photons per second and bandwidth of the X-ray pulses of 0.2%.

- Measurement of an absolute amplitude of periodic displacements with sub-angstrom precision based on an analytical method. This method uses the relationship between periodic surface displacements and diffraction efficiency at the periodic surface grating consisting of such displacements. Further, the modelling of such periodic surface displacements allows a decomposition of a periodic surface displacement in its thermal and strain induced components.

- Full spatial and temporal control of periodic surface displacements. This is achieved by a subsequent excitation of strain waves with multiple laser pulses in a Transient Grating configuration. The new experimental setup provides not only the control of the temporal phase by varying the delay between laser pulses, but an independent control of the spatial phase. This allows a creation

and independent control of a slowly decaying induced thermal grating and strain-driven oscillating periodic surface displacements.

- A study of excitation mechanisms and dynamic of the magnetization precession in Pt/Co multilayers. Evaluation of the collected experimental data on the coupling between the magnetization precession and strain oscillations suggests that a pure thermal excitation is not the mechanism responsible for the excitation of ferromagnetic precession, unlike it was shown in Co samples earlier.

Techniques presented in this thesis are only the first step towards employing strain as a functional tool in solid-state devices. Next steps consist in determining further processes that are prone to nanoscale strain control and transferring the techniques described in this thesis to real-world applications.

Bibliography

[1] Yuanjie Huang. Strain-induced electric effects in condensed matters. Journal of Materials Sciences and Application, 5:44–57, 06 2019.

[2] Alexei Bykhovski, Boris Gelmont, and Michael Shur. The influence of the strain-induced electric field on the charge distribution in gan-aln-gan structure. Journal of Applied Physics, 74(11):6734–6739, 1993.

[3] Markus Schmitz, Alexander Weber, Oleg Petracic, Markus Waschk, Paul Zakalek, Stefan Mattauch, Alexandros Koutsioubas, and Thomas Brückel. Strain and electric field control of magnetism in $La_{(1-x)}Sr_xMnO_3$ thin films on ferroelectric $BaTiO_3$ substrates. New Journal of Physics, 22(5):053018, May 2020.

[4] John Cenker, Shivesh Sivakumar, Kaichen Xie, Aaron Miller, Pearl Thijssen, Zhaoyu Liu, Avalon H. Dismukes, Jordan Fonseca, Eric Anderson, Xiaoyang Zhu, Xavier Roy, Di Xiao, Jiun Haw Chu, Ting Cao, and Xiaodong Xu. Reversible strain-induced magnetic phase transition in a van der waals magnet. Nature Nanotechnology, 17:256 – 261, 2022.

[5] Yao Wang, Shan-Shan Wang, Yunhao Lu, Jian-Zhong Jiang, and Shengyuan Yang. Strain-induced isostructural and magnetic phase transitions in monolayer mon2. Nano Letters, 16, 06 2016.

[6] Nathaniel Woodward, Brandon Mitchell, I. Feng, J. Li, H. Jiang, Joung-Yol Lin, J. Zavada, and Volkmar Dierolf. Enhanced magnetization in erbium doped gan thin films due to strain induced electric fields. Applied Physics Letters - APPL PHYS LETT, 99, 09 2011.

[7] Christopher Nicholson, Maxime Rumo, Aki Pulkkinen, Geoffroy Kremer, Björn Salzmann, M.-L Mottas, Baptiste Hildebrand, T. Jaouen, Timur Kim, Saumya Mukherjee, Keyuan Ma, Matthias Muntwiler, Fabian Rohr, Cephise Cacho, and Claude Monney. Uniaxial strain-induced phase transition in the 2d topological semimetal irte2. Communications Materials, 2, 03 2021.

[8] Philippe Benech and Jean-Marc Duchamp. Piezoelectric materials in rf applications. In Toshio Ogawa, editor, Piezoelectric Materials. IntechOpen, Rijeka, 2016.

[9] M Sonnleitner, M Ritsch-Marte, and H Ritsch. Optomechanical deformation and strain in elastic dielectrics. New Journal of Physics, 14(10):103011, oct 2012.

[10] Pu Chen, Guangxi Li, and Zhiyuan Zhu. Development and application of saw filter. Micromachines, 13, 2022.

[11] P.H. Bucksbaum and R. Merlin. The phonon bragg switch: a proposal to generate sub-picosecond x-ray pulses. Solid State Communications, 111(10):535–539, 1999.

[12] J.M.H. Sheppard, P. Sondhauss, R. Merlin, P. Bucksbaum, R.W. Lee, and J.S. Wark. Simulations of the phonon bragg switch in gaas. Solid State Communications, 136(3):181–185, 2005.

[13] Peter Gaal, Daniel Schick, Marc Herzog, André Bojahr, Roman Shayduk, Jevgeni Goldshteyn, Wolfram Leitenberger, Ionela Vrejoiu, Dmitry Khakhulin, Michael Wulff, and M. Bargheer. Ultrafast switching of hard x-rays. Journal of synchrotron radiation, 21:380–5, 03 2014.

[14] Hans Joachim Eichler, Guenter Peter, and Dieter W. Pohl. Laser-induced dynamic gratings. Springer Berlin, 2013.

[15] Peter Hess. Surface acoustic waves in materials science. Physics Today, 55(3):42–47, March 2002.

[16] D.R. Morgan. Surface acoustic wave devices and applications: 1. introductory review. Ultrasonics, 11(3):121–131, 1973.

[17] S.V. Biryukov, Yu.V. Gulyaev, Victor Krylov, and Victor Plessky. Surface Acoustic Waves in Inhomogeneous Media, volume 20. 06 1995.

[18] J. Janusonis, T. Jansma, C. L. Chang, Qi Liu, A. Gatilova, A. M. Lomonosov, V. Shalagatskyi, T. Pezeril, V. V. Temnov, and R. I. Tobey. Transient grating spectroscopy in magnetic thin films: Simultaneous detection of elastic and magnetic dynamics. Scientific Reports, 6, July 2016.

[19] Felix Hofmann, Michael P. Short, and Cody A. Dennett. Transient grating spectroscopy: An ultrarapid, nondestructive materials evaluation technique. MRS Bulletin, 44(5):392–402, 2019.

[20] O. W. Käding, H. Skurk, A. A. Maznev, and E. Matthias. Transient thermal gratings at surfaces for thermal characterization of bulk materials and thin films. Applied Physics A: Materials Science & Processing, 61(3):253–261, September 1995.

[21] Anil R. Duggal, John A. Rogers, and Keith A. Nelson. Real-time optical characterization of surface acoustic modes of polyimide thin-film coatings. Journal of Applied Physics, 72(7):2823–2839, 1992.

[22] B. Sun, J. M. Winey, N. Hemmi, Z. A. Dreger, K. A. Zimmerman, Y. M. Gupta, Darius H. Torchinsky, and Keith A. Nelson. Second-order elastic constants of pentaerythritol tetranitrate and cyclotrimethylene trinitramine using impulsive stimulated thermal scattering. Journal of Applied Physics, 104(7):073517, 2008.

[23] John A. Rogers and Keith A. Nelson. Study of lamb acoustic waveguide modes in unsupported polyimide thin films using real-time impulsive stimulated thermal scattering. Journal of Applied Physics, 75(3):1534–1556, 1994.

[24] J. Janušonis, C. L. Chang, T. Jansma, A. Gatilova, V. S. Vlasov, A. M. Lomonosov, V. V. Temnov, and R. I. Tobey. Ultrafast magnetoelastic probing of surface acoustic transients. Physical Review B, 94(2), jul 2016.

[25] C. L. Chang, R. R. Tamming, T. J. Broomhall, J. Janusonis, P. W. Fry, R. I. Tobey, and T. J. Hayward. Selective excitation of localized spin-wave modes by optically pumped surface acoustic waves. Phys. Rev. Appl., 10:034068, Sep 2018.

[26] Chengyun Hua and Austin J. Minnich. Transport regimes in quasiballistic heat conduction. Phys. Rev. B, 89:094302, Mar 2014.

[27] Baozhu Lu, Mykola Abramchuk, Fazel Tafti, and Darius H. Torchinsky. Transient grating measurements at ultralow probe power. J. Opt. Soc. Am. B, 37(2):433–439, Feb 2020.

[28] Jeremy A. Johnson, Alexei A. Maznev, Mayank T. Bulsara, Eugene A. Fitzgerald, T. C. Harman, S. Calawa, C. J. Vineis, G. Turner, and Keith A. Nelson. Phase-controlled, heterodyne laser-induced transient grating measurements of

thermal transport properties in opaque material. Journal of Applied Physics, 111(2):023503, 2012.

[29] J.-E. Pudell, M. Sander, R. Bauer, M. Bargheer, M. Herzog, and P. Gaal. Full spatiotemporal control of laser-excited periodic surface deformations. Phys. Rev. Applied, 12:024036, Aug 2019.

[30] Matthias Sander, Jan-Etienne Pudell, Marc Herzog, M. Bargheer, Roman Bauer, Valentin Besse, Vasily Temnov, and Peter Gaal. Quantitative disentanglement of coherent and incoherent laser-induced surface deformations by time-resolved x-ray reflectivity. Applied Physics Letters, 111, 12 2017.

[31] A. A. Maznev, K. A. Nelson, and J. A. Rogers. Optical heterodyne detection of laser-induced gratings. Opt. Lett., 23(16):1319–1321, Aug 1998.

[32] ALEJANDRO VEGA-FLICK, J. Eliason, A. Maznev, Amey Khanolkar, Maroun Abi Ghanem, N. Boechler, Juan Alvarado-Gil, and Keith Nelson. Laser-induced transient grating setup with continuously tunable period. Review of Scientific Instruments, 86:123101, 12 2015.

[33] J.W. Goodman. Introduction to Fourier Optics. McGraw-Hill classic textbook reissue series. McGraw-Hill, 1968.

[34] M. Born and E. Wolf. Principles of Optics: Electromagnetic Theory of Propagation, Interference and Diffraction of Light. Elsevier Science, 2013.

[35] Soheil Mehrabkhani and Thomas Schneider. Is the rayleigh-sommerfeld diffraction always an exact reference for high speed diffraction algorithms? Opt. Express, 25(24):30229–30240, Nov 2017.

[36] W. Freude and G.K. Grau. Rayleigh-sommerfeld and helmholtz-kirchhoff integrals: application to the scalar and vectorial theory of wave propagation and diffraction. Journal of Lightwave Technology, 13(1):24–32, 1995.

[37] Jan A. C. Veerman, Jurgen J. Rusch, and H. Paul Urbach. Calculation of the rayleigh–sommerfeld diffraction integral by exact integration of the fast oscillating factor. J. Opt. Soc. Am. A, 22(4):636–646, Apr 2005.

[38] James E. Harvey and Richard N. Pfisterer. Understanding diffraction grating behavior, part II: parametric diffraction efficiency of sinusoidal reflection (holographic) gratings. Optical Engineering, 59(1):1 – 11, 2020.

[39] Anders Madsen, Tilo Seydel, Metin Tolan, and Gerhard Grübel. Grazing-incidence scattering of coherent X-rays from a liquid surface. Journal of Synchrotron Radiation, 12(6):786–794, Nov 2005.

[40] Jan-David Nicolas, Tobias Reusch, Markus Osterhoff, Michael Sprung, Florian J. R. Schülein, Hubert J. Krenner, Achim Wixforth, and Tim Salditt. Time-resolved coherent X-ray diffraction imaging of surface acoustic waves. Journal of Applied Crystallography, 47(5):1596–1605, Oct 2014.

[41] James Harvey, Cynthia Vernold, Andrey Krywonos, and Patrick Thompson. Diffracted radiance: A fundamental quantity in nonparaxial scalar diffraction theory. Applied optics, 38:6469–81, 12 1999.

[42] James Harvey, Cynthia Vernold, Andrey Krywonos, and Patrick Thompson. Diffracted radiance: A fundamental quantity in nonparaxial scalar diffraction theory: Errata. Applied optics, 39:6374–5, 01 2001.

[43] James E. Harvey, Andrey Krywonos, and Dijana Bogunovic. Nonparaxial scalar treatment of sinusoidal phase gratings. J. Opt. Soc. Am. A, 23(4):858–865, Apr 2006.

[44] Douglas A. Gremaux and Neal C. Gallagher. Limits of scalar diffraction theory for conducting gratings. Appl. Opt., 32(11):1948–1953, Apr 1993.

[45] Drew A. Pommet, M. G. Moharam, and Eric B. Grann. Limits of scalar diffraction theory for diffractive phase elements. J. Opt. Soc. Am. A, 11(6):1827–1834, Jun 1994.

[46] James E. Harvey and Richard N. Pfisterer. Understanding diffraction grating behavior: including conical diffraction and Rayleigh anomalies from transmission gratings. Optical Engineering, 58(8):1 – 21, 2019.

[47] H. Ibach and H. Lüth. Solid-State Physics: An Introduction to Principles of Materials Science. Advanced texts in physics. Springer Berlin Heidelberg, 2009.

[48] N. W. Ashcroft and N. D. Mermin. Solid State Physics. Holt-Saunders, 1976.

[49] M T Johnson, P J H Bloemen, F J A den Broeder, and J J de Vries. Magnetic anisotropy in metallic multilayers. Reports on Progress in Physics, 59(11):1409–1458, nov 1996.

[50] S. Buegel. Magnetische anisotropie und magnetostriktion. Schriften des Forschungszentrums Juelich, 1999.

[51] N. Akulov. Zur quantentheorie der temperaturabhaengigkeit der magnetisierungskurve. Z. Phys., 100:197–202, 03 1936.

[52] M. Heigl, R. Wendler, S. D. Haugg, and M. Albrecht. Magnetic properties of co/ni-based multilayers with pd and pt insertion layers. Journal of Applied Physics, 127(23):233902, Jun 2020.

[53] Holger Stillrich, Christian Menk, Robert Frömter, and Hans Peter Oepen. Magnetic anisotropy and spin reorientation in co/pt multilayers: Influence of preparation. Journal of Magnetism and Magnetic Materials, 322(9-12):1353–1356, 2010.

[54] M. D. Kuz'min. Shape of temperature dependence of spontaneous magnetization of ferromagnets: Quantitative analysis. Phys. Rev. Lett., 94:107204, Mar 2005.

[55] Earl R. Callen and Herbert B. Callen. Static magnetoelastic coupling in cubic crystals. Phys. Rev., 129:578–593, Jan 1963.

[56] Lev Davidovich Landau and E Lifshitz. On the theory of the dispersion of magnetic permeability in ferromagnetic bodies. Phys. Z. Sowjet., 8:153, 1935.

[57] G. V. Skorotskii and L. V. Kurbatov. Theory of anisotropy of the width of ferromagnetic resonance. Sov. Phys. JETP, 35(8):148–151, Jan 1959.

[58] J. Smit and H. G. Beljers. Philips Res. Repts., 10:113, 6 1955.

[59] L. Baselgia, M. Warden, F. Waldner, Stuart L. Hutton, John E. Drumheller, Y. Q. He, P. E. Wigen, and M. Maryško. Derivation of the resonance frequency from the free energy of ferromagnets. Phys. Rev. B, 38:2237–2242, Aug 1988.

[60] D Sander. The correlation between mechanical stress and magnetic anisotropy in ultrathin films. Reports on Progress in Physics, 62(5):809–858, jan 1999.

[61] S. W. Sun and R. C. O'Handley. Surface magnetoelastic coupling. Phys. Rev. Lett., 66:2798–2801, May 1991.

[62] Mathias Sander, Roman Bauer, Victoria Kabanova, Matteo Levantino, Michael Wulff, Daniel Pfuetzenreuter, Jutta Schwarzkopf, and Peter Gaal. Demonstration of a picosecond Bragg switch for hard X-rays in a synchrotron-based pump–probe experiment. Journal of Synchrotron Radiation, 26(4):1253–1259, Jul 2019.

[63] M. Sander, J.-E. Pudell, M. Herzog, M. Bargheer, R. Bauer, V. Besse, V. Temnov, and P. Gaal. Quantitative disentanglement of coherent and incoherent laser-induced surface deformations by time-resolved x-ray reflectivity. Applied Physics Letters, 111(26):261903, 2017.

[64] E. Beaurepaire, J.-C. Merle, A. Daunois, and J.-Y. Bigot. Ultrafast spin dynamics in ferromagnetic nickel. Phys. Rev. Lett., 76:4250–4253, May 1996.

[65] Andrei Kirilyuk, Alexey Kimel, Fredrik Hansteen, Theo Rasing, and Roman V. Pisarev. Ultrafast all-optical control of the magnetization in magnetic dielectrics. Low Temperature Physics, 32(8):748–767, 2006.

[66] C. D. Stanciu, F. Hansteen, A. V. Kimel, A. Kirilyuk, A. Tsukamoto, A. Itoh, and Th. Rasing. All-optical magnetic recording with circularly polarized light. Phys. Rev. Lett., 99:047601, Jul 2007.

[67] J. Kisielewski, A. Kirilyuk, A. Stupakiewicz, A. Maziewski, A. Kimel, Th. Rasing, L. T. Baczewski, and A. Wawro. Laser-induced manipulation of magnetic anisotropy and magnetization precession in an ultrathin cobalt wedge. Phys. Rev. B, 85:184429, May 2012.

[68] Oleksandr Kovalenko, Thomas Pezeril, and Vasily V. Temnov. New concept for magnetization switching by ultrafast acoustic pulses. Phys. Rev. Lett., 110:266602, Jun 2013.

[69] C Schmising, M Giovannella, David Weder, S Schaffert, J Webb, and S Eisebitt. Nonlocal ultrafast demagnetization dynamics of co/pt multilayers by optical field enhancement. New Journal of Physics, 17, 03 2015.

[70] B. Pfau, S. Schaffert, L. Müller, C. Gutt, A. Al-Shemmary, F. Büttner, R. Delaunay, S. Düsterer, S. Flewett, R. Frömter, J. Geilhufe, E. Guehrs, C. M. Günther, R. Hawaldar, M. Hille, N. Jaouen, A. Kobs, K. Li, J. Mohanty, H. Redlin, W. F. Schlotter, D. Stickler, R. Treusch, B. Vodungbo, M. Kläui, H. P. Oepen, J. Lüning, G. Grübel, and S. Eisebitt. Ultrafast optical demagnetization manipulates nanoscale spin structure in domain walls. Nature Communications, 3(1):1100, Oct 2012.

[71] T. L. Linnik, A. V. Scherbakov, D. R. Yakovlev, X. Liu, J. K. Furdyna, and M. Bayer. Theory of magnetization precession induced by a picosecond strain pulse in ferromagnetic semiconductor (ga,mn)as. Phys. Rev. B, 84:214432, Dec 2011.

[72] L. Dreher, M. Weiler, M. Pernpeintner, H. Huebl, R. Gross, M. S. Brandt, and S. T. B. Goennenwein. Surface acoustic wave driven ferromagnetic resonance in nickel thin films: Theory and experiment. Phys. Rev. B, 86:134415, Oct 2012.

[73] L. Thevenard, I. S. Camara, S. Majrab, M. Bernard, P. Rovillain, A. Lemaître, C. Gourdon, and J.-Y. Duquesne. Precessional magnetization switching by a surface acoustic wave. Phys. Rev. B, 93:134430, Apr 2016.

[74] Jochen Wagner. The magnetic properties of ultrathin cobalt multilayers symmetrically and antisymmetrically sandwiched between layers of platinum and iridium. Dissertation, 2018.

[75] D. Schick, A. Bojahr, M. Herzog, R. Shayduk, C. von Korff Schmising, and M. Bargheer. udkm1dsim—a simulation toolkit for 1d ultrafast dynamics in condensed matter. Computer Physics Communications, 185(2):651 – 660, 2014.

JOURNAL OF SYNCHROTRON RADIATION
ISSN 1600-5775

Demonstration of a picosecond Bragg switch for hard X-rays in a synchrotron-based pump–probe experiment

Mathias Sander,[a,b] Roman Bauer,[c,b] Victoria Kabanova,[a] Matteo Levantino,[a] Michael Wulff,[a] Daniel Pfuetzenreuter,[d] Jutta Schwarzkopf[d] and Peter Gaal[c,b]*

[a]European Sychrotron Radiation Facility, 71 Avenue des Martyrs, 38000 Grenoble, France, [b]Tailored X-ray Products gGmbH, Berlin, Germany, [c]Institut für Nanostruktur- und Festkörperphysik, Universität Hamburg, Luruper Chaussee 149, Hamburg 20355, Germany, and [d]Leibniz-Institut für Kristallzüchtung, Max-Born-Strasse 2, 12489 Berlin, Germany. *Correspondence e-mail: pgaal@physnet.uni-hamburg.de

Received 29 November 2018
Accepted 18 April 2019

Edited by G. Grübel, HASYLAB at DESY, Germany

Keywords: ultrafast X-ray diffraction; photoacoustics; synchrotrons; pump–probe experiments; active X-ray optics.

A benchmark experiment is reported that demonstrates the shortening of hard X-ray pulses in a synchrotron-based optical pump–X-ray probe measurement. The pulse-shortening device is a photoacoustic Bragg switch that reduces the temporal resolution of an incident X-ray pulse to approximately 7.5 ps. The Bragg switch is employed to monitor propagating sound waves in nanometer thin epitaxial films. From the experimental data, the pulse duration, diffraction efficiency and switching contrast of the device can be inferred. A detailed efficiency analysis shows that the switch can deliver up to 10^9 photons s^{-1} in high-repetition-rate synchrotron experiments.

1. Introduction

Currently, users in the synchrotron community with an interest in X-ray pulses of a sub-100 ps duration face a changing landscape of facilities. Conditions for time-resolved experiments have been improved significantly by the advent of X-ray free-electron lasers (XFELs), which provide ultrashort hard X-ray pulses of unprecedented brilliance [*Nature Photonics* editorial (2017), vol. 11, p. 609]. Alternatives for hard X-ray pulses of a few picoseconds or femtoseconds are the femto-slicing beamlines at the ALS (Schoenlein *et al.*, 2000) and SLS (Ingold *et al.*, 2007; Beaud *et al.*, 2007), table-top plasma sources (Zamponi *et al.*, 2009; Schick *et al.*, 2012) and the new FemtoMax facility at MAX IV (Enquist *et al.*, 2018). X-ray pulses with a duration of a few picoseconds are generated in third-generation storage rings using a low-charge-filling mode, the so-called low-α mode (Jankowiak & Wüstefeld, 2013). This mode reduces the total photon flux due to the low filling charge and is therefore only offered a few weeks per year. Currently, an upgrade project is planned for the BESSY II synchrotron (Helmholtz-Zentrum Berlin, 2015) which will provide a permanent improved low-α mode after the installation of additional RF cavities in the storage ring (Di Mitri, 2018).

In parallel with the commissioning of XFELs and alternative short-pulse sources, many existing synchrotrons are being updated to fourth-generation low-emittance storage rings (Schroer *et al.*, 2018). While low emittance provides better focusing properties and higher beam coherence, the temporal structure, *i.e.* the pulse duration and pulse repetition rate, is significantly less favourable for time-resolved experiments. Opportunities for time-resolved experiments at new

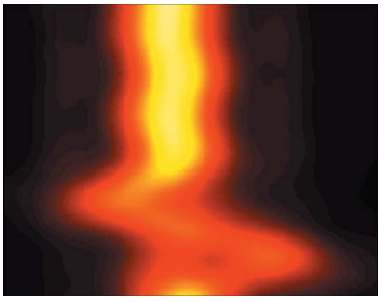

diffraction-limited synchrotron radiation facilities are discussed intensively within the community.

In this article we present a new photoacoustic Bragg switch that allows the shortening of hard X-ray pulses emitted from synchrotron storage rings, down to a few picoseconds. The idea of switching a synchrotron X-ray pulse with a controlled lattice deformation is almost 50 years old (Allam, 1970). Since then, several attempts have been made that relied on piezoelectric excitation (Grigoriev *et al.*, 2006; Zolotoyabko & Quintana, 2004), the generation of optical (Bucksbaum & Merlin, 1999; Sheppard *et al.*, 2005) and acoustic phonons (Gaal *et al.*, 2014; Sander *et al.*, 2016) or picosecond thermal excitations (Navirian *et al.*, 2011). Our device, which we call the PicoSwitch, has been tested in a synchrotron-based optical pump–X-ray probe experiment to measure the propagation of sound waves in epitaxial nanometer thin films. We discuss important quality parameters, *e.g.* the switching contrast and the angle- and time-dependent diffraction efficiency to determine the absolute pulse duration and photon efficiency of the shortened pulse. Based on our experimental results, we show that the switch can be operated at repetition rates of up to 1 MHz and delivers pulses of 5–10 ps duration. The device accepts a limited relative bandwidth of up to $\Delta E/E_0 = 0.2\%$. On the ID09 beamline at the European Synchrotron (ESRF), where our benchmark experiment was performed, the PicoSwitch can deliver a total flux of up to 10^9 photons s^{-1}, which is the typical intensity from a bending-magnet beamline at the ESRF.

2. Experimental

In the following, we give a brief introduction to the working principle of the PicoSwitch. A more comprehensive description can be found elsewhere (Sander *et al.*, 2016).

The layout of the pulse-shortening benchmark experiment is shown in Fig. 1(*a*). Unlike conventional pump–probe experiments, we employ two optical pump beams from the same laser source, one to trigger the PicoSwitch and the other to excite the sample. The time delay of the first excitation is selected such that the PicoSwitch diffracts incident photons while the maximum intensity of the long synchrotron X-ray pulse is present. Thus, only a temporal slice of the maximum intensity is diffracted from the PicoSwitch, while other parts of the X-ray pulse are suppressed. The shortened X-ray pulse impinges on the sample and is employed to probe dynamics induced by the second optical pump pulse. Since both the PicoSwitch and the sample are excited by optical pulses that stem from the same laser source, the time delay between the optical pump and the shortened X-ray probe pulse is completely jitter free. The relative pump–probe delay between the optical excitation of the sample and the shortened X-ray pulse is controlled by a motorized delay stage to record the transient sample dynamics up to a pump–probe delay of 2 ns.

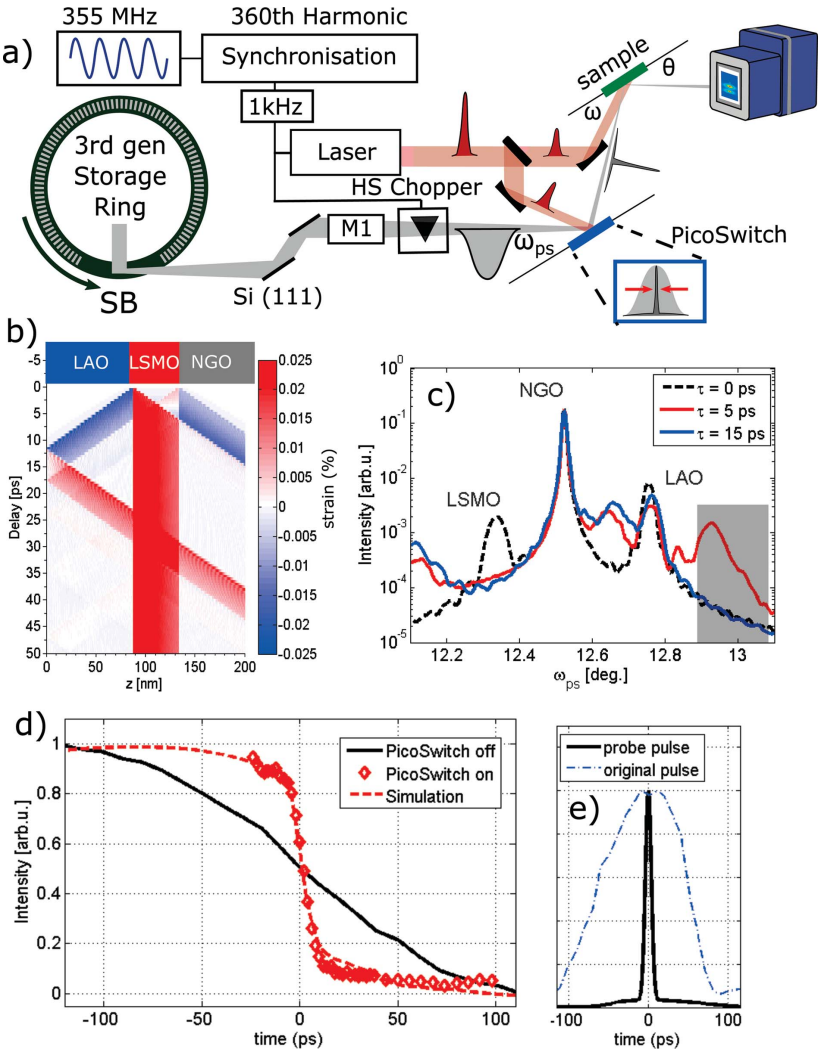

Figure 1
The working principle of the PicoSwitch. (*a*) The experimental setup on the ID09 beamline at the ESRF. Two optical pulses from a 1 kHz amplified laser system are employed to excite the PicoSwitch (blue) and the sample (green). X-ray pulses from the storage ring impinge on the PicoSwitch at an incidence angle ω_{ps}. A shortened X-ray pulse is diffracted to the sample at an incidence angle ω. (*b*) (Top) A sketch of the PicoSwitch and sample structure (details in the main text). The plot below shows a spatiotemporal strain map of propagating compression (red) and expansion (blue) waves in the bilayer structures. (*c*) Transient XRD curves of the PicoSwitch after laser excitation calculated from the strain map in panel (*b*). The simulations for 0 ps (black dashed line), 5 ps (red solid line) and 15 ps (blue solid line) show that the transient diffraction efficiency is turned on and off in the grey shaded area within a few picoseconds. (*d*) Pump–probe measurements with the shortened pulse (red symbols) and the original synchrotron pulse (black solid line) of the ultrafast decrease in diffraction efficiency from a nanostructure. A simulation of the short-pulse experiment is shown as a red dashed line. (*e*) The original (blue dot-dashed line) and shortened (black line) X-ray probe pulse. The original pulse was measured with a correlation technique (Gaal *et al.*, 2012) andthe shortened pulse was extracted from simulations (Gaal *et al.*, 2014; Sander *et al.*, 2016).

The PicoSwitch structure is shown in the top part of Fig. 1(*b*) and consists of two thin films grown by pulsed laser deposition (PLD) on a dielectric substrate (Sellmann *et al.*, 2014). The top layer is composed of a transparent dielectric. The bottom layer is an opaque metal that acts as a thermoelastic transducer upon optical excitation. We underline that several material combinations may be used to build a PicoSwitch device. Here, we use a combination of $LaAlO_3$ (LAO, 85 nm, transparent) and $La_{0.66}Sr_{0.33}MnO_3$ (LSMO, 57 nm, metallic) grown on an $NdGaO_3$ (NGO) substrate. Sound waves generated upon absorption of an optical pump pulse are shown in the coloured plot in Fig. 1(*b*) as expansive (red) and compressive (blue) strain. The strain pulses are launched from the interface of the transducer to the adjacent top layer and the substrate, respectively.

We calculate the impact of laser-generated strain waves on the angular diffraction efficiency of the PicoSwitch. The results are shown in Fig. 1(*c*) for pump–probe delays of 0, 5 and 15 ps (Schick *et al.*, 2014). The transient strain propagating through the PicoSwitch shifts the diffraction efficiency of the top LAO layer to larger diffraction angles and back to the initial position within 15 ps. The angular region is marked in grey in Fig. 1(*c*). Here, the PicoSwitch acts as a switchable mirror that is turned on and off by an acoustic pulse on a picosecond timescale.

An important quality parameter of the PicoSwitch is the switching contrast, which describes the suppression of incident X-ray photons during the off-state of the switch. The diffraction efficiency is at a low level η_0 before the arrival of the optical pump pulse. Upon laser excitation, the diffraction efficiency mounts to a high level η_{on} for a switching time ΔT, which is determined by the propagation of strain waves in the structure. After the coherent strain waves have propagated away from the thin films into the substrate, the diffraction efficiency falls back to its initial value $\eta_\infty \simeq \eta_0$. We define the switching contrast c_{sw} with the following expression (Gaal *et al.*, 2012),

$$c_{sw} = \frac{\eta - \eta_{0,\infty}}{\eta_{0,\infty}}. \tag{1}$$

c_{sw} basically has the same value before and after the switching is turned on and off This is a significant improvement compared to earlier designs of the PicoSwitch, where the final contrast $c_{sw,\infty}$ was strongly reduced by laser heating of the structure (Gaal *et al.*, 2014). Whether introducing the PicoSwitch results in high temporal resolution or not depends on the ratio of the pulse areas of the original and shortened pulses. Therefore, we define the total contrast c_{total} as the product of the switching contrast and the area loss factor, *i.e.* the ratio of the normalized pulse area of the original and shortened pulses,

$$c_{total} = c_{sw} \times \mathrm{ALF}, \tag{2}$$

where ALF is the area loss factor,

$$\mathrm{ALF} = \frac{\int_{-\infty}^{\infty} \mathrm{d}t\, I_{sw}(t) / I_{sw,m}}{\int_{-\infty}^{\infty} \mathrm{d}t\, \tilde{I}(t) / \tilde{I}_m}, \tag{3}$$

and $I_{sw}(t)$, $I_{sw,m}$, $\tilde{I}(t)$ and $\tilde{I}_m$ denote the time-dependent and maximum intensities of the shortened and original X-ray pulses, respectively. While $\tilde{I}(t)$ can be easily measured with the PicoSwitch (Gaal *et al.*, 2012), I_{sw} is deduced from model calculations as shown below.

The pulse-shortening capability is shown in Fig. 1(*d*), which shows a step-like decrease in the diffraction efficiency upon optical excitation. The sample and the physical origin of the sudden intensity change are discussed below. For now, we highlight the influence of the duration of the probe pulse on the measured dynamics. Fig. 1(*d*) clearly shows a dramatic increase in the temporal resolution of a measurement that employs the PicoSwitch. The temporal shape of the corresponding probe pulse is shown in Fig. 1(*e*). The original long synchrotron pulse was measured using a fast sampling method (Gaal *et al.*, 2012), which yields a full width at half-maximum (FWHM) pulse duration of 120 ps. We also clearly recognize the expected asymmetric pulse shape. The shortened pulse was derived from a simulation [red dashed line in Fig. 1(*d*)] and cross-checked by comparison with the experimental data.

3. Results and discussion

Now we discuss the experimental capabilities of the PicoSwitch pulse-shortening scheme in a real synchrotron-based pump–probe experiment. The sample is composed of a similar structure to the PicoSwitch itself, *i.e.* a thin-film system composed of a transparent dielectric LAO top layer with a thickness of 104 nm on a metallic LSMO layer with a thickness of 93 nm. The stack is grown on an NGO substrate. Note that the film thicknesses of the sample and the PicoSwitch are different, which results in slightly different propagation times of the coherent sound wave through the respective structure.

The lattice dynamics measured by time-resolved X-ray diffraction (XRD) of the metallic LSMO and dielectric LAO layers are shown in Figs. 2(*a*) and 2(*b*), respectively. Experiments were performed at an X-ray photon energy of 14.85 keV on the (002) lattice planes in symmetric ω–2θ geometry.

Both the sample and the PicoSwitch were mounted on motorized *xyz* translation stages and on a motorized rotation circle with angular resolution better than 0.1 mrad for tuning the incidence angle of the X-ray beam. The size of the X-ray beam before and after symmetric diffraction from the PicoSwitch was approximately 40 µm × 60 µm. The acceptance angle of the PicoSwitch was 870 µrad at an angle of 12.9°, which is eight times larger than the full vertical divergence in the focus of the X-ray beam. At the sample position, approximately 150 mm after the PicoSwitch, we observed no changes in the X-ray beam footprint, divergence or stability. In our setup, the shortened beam is deflected upwards. Insertion of a multilayer mirror could be used to deflect the beam downwards, thus yielding a horizontal beam. The repetition rate of the X-ray beam is reduced to 1 kHz by a system of choppers (Cammarata *et al.*, 2009) to match the laser repetition frequency. The main purpose of the choppers is to reduce the heat load on the beamline optics from the intense X-ray

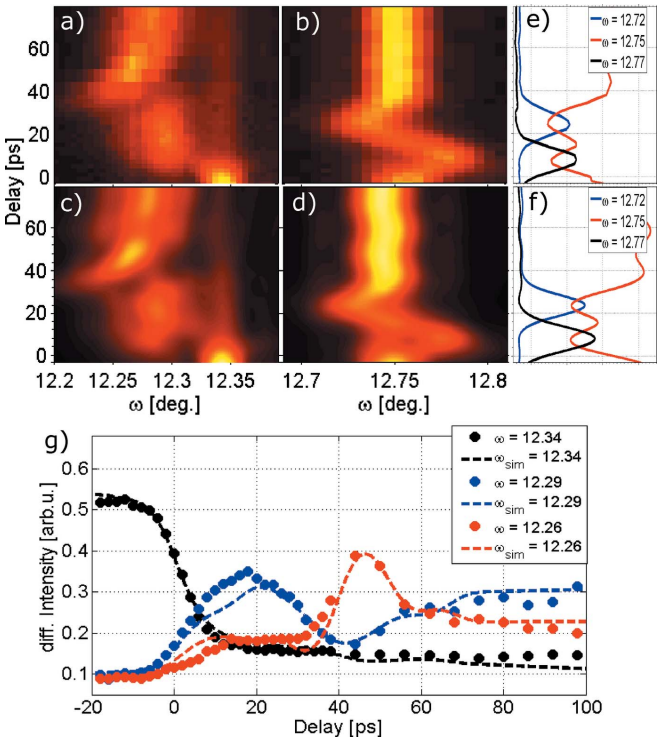

Figure 2
Experimental data. (*a*, *b*) Time-resolved measurements of propagating sound waves in (*a*) the LSMO film and (*b*) the LAO film of the sample. The measurement employed pulse shortening with the PicoSwitch. Fast picosecond lattice dynamics are clearly resolved by the experiment. The mechanism behind the observed XRD peak shift is outlined in the main text. (*c*, *d*) Simulations of propagating sound waves in (*c*) the LSMO layer and (*d*) the LAO layer. Comparison of the simulation and experimental data reveals an X-ray probe pulse duration of 7.5 ps and a total switching contrast of $c_{\rm total}$ = 2.94. (*e*)–(*g*) Cross sections of measured and simulated data at different incidence angles ω on the sample.

radiation. They also protect soft-matter and biological samples from unnecessary radiation damage, thus leading to a longer sample lifetime. It should be noted that the PicoSwitch contrast is not sufficient to gate a single pulse from the synchrotron pulse train. Instead, gating can be performed electronically by modern detectors (Shayduk *et al.*, 2017). On the ID09 beamline, diffraction and scattering signals are recorded by a Rayonix HS170 detector in accumulation mode, *i.e.* the signal from many laser/X-ray pulse pairs is accumulated without any time resolution provided by the detector. Beam parameters are summarized in Table 1.

The sample and PicoSwitch were excited with an optical fluence of 30 mJ cm^{-2}. The principal axes of the elliptical laser footprint on the sample and PicoSwitch were 920 µm/600 µm and 720 µm/630 µm, respectively. We performed simulations of coherent acoustic phonon propagation in the sample using a one-dimensional linear chain model of masses and springs (Herzog, Schick *et al.*, 2012). The phenomenon of propagating high-frequency coherent acoustic phonon wavepackets is well understood (Thomsen *et al.*, 1986; Rose-Petruck *et al.*, 1999; Larsson *et al.*, 2002; Bargheer *et al.*, 2004; Bojahr *et al.*, 2013, 2015; Herzog, Bojahr *et al.*, 2012; Shayduk *et al.*, 2013). Our simulations yield a two-dimensional map of lattice strain

Table 1
Main parameters of the ID09 beamline at ESRF.

The second column lists the parameters after the Extremely Brilliant Source (EBS) upgrade (FWHM values).

	ESRF	ESRF-EBS
Focus		
H (µm)	40	20
V (µm)	60	20
Divergence		
H (µrad)	860	53
V (µrad)	106	28
Photons per pulse (pink beam)	2.1 × 10^9	3.0 × 10^9
Pulse duration	<135 ps	<150 ps

versus pump–probe delay along the out-of-plane spatial axis in the sample, as shown in Fig. 1(*b*). From the spatiotemporal strain map we calculate transient XRD curves using dynamic diffraction theory (Schick *et al.*, 2014; Warren, 1990). Finally, we convolute the XRD simulation with the simulated X-ray probe pulse after reflection from the PicoSwitch. The FWHM pulse duration of the shortened pulse is approximately 7.5 ps and the pulse is shown in Fig. 1(*e*).

Figs. 2(*c*) and 2(*d*) show simulated dynamics of the LSMO and LAO diffraction peaks, respectively. To reproduce the experimental data in a simulated pump–probe experiment, we find a switching contrast of $c_{\rm sw}$ = 33. With ALF = 11.34 we find a total contrast $c_{\rm total}$ of 2.93. Both experiment and simulation show the effect of insufficiently suppressed photons of the original long X-ray pulse, *e.g.* at the equilibrium angle of the LSMO peak of 12.34 in Figs. 2(*a*) and 2(*c*). Still, the picosecond dynamics of the propagating sound waves are clearly resolved in the measurement.

Comparing the coloured plots shown in Figs. 2(*a*) and 2(*c*) and those in Figs. 2(*b*) and 2(*d*), we find excellent agreement of the simulated pump–probe experiment with the experimental data. In particular, we observe a step-like drop in the LSMO peak intensity at ω = 12.34° [black dashed line and black filled circles, Fig. 2(*g*)]. A delay scan at this incidence angle is shown in Fig. 1(*d*) compared with a measurement of the same dynamics with the original ESRF X-ray probe pulse. The LSMO peak reappears at ω = 12.29° for approximately 15 ps [blue dashed line and blue filled circles, Fig. 2(*g*)]. This new peak position corresponds to thermal expansion resulting from the energy deposited by the absorbed optical excitation pulse. At a pump–probe delay of ∼40 ps, the LSMO peak is distorted again but returns to its intermediate expanded angular position [red dashed line and red filled circles, Fig. 2(*g*)].

The dynamic features observed at the LSMO peak are well understood by simulations of thermal expansion and coherent phonon generation and propagation (Herzog, Schick *et al.*, 2012). The initial shift of the LSMO reflex stems from thermal expansion, while the second peak distortion originates from the coherent sound wave that is reflected back at the sample surface (Sander *et al.*, 2016). Having determined the sample geometry by static XRD and ellipsometry measurements, we adjust the simulated dynamics via the sound velocity in LSMO

and LAO, respectively, to the experimental data. The result agrees well with values reported by other groups (Bogdanova *et al.*, 2003; Michael *et al.*, 1992). For comparison, a similar experiment reported earlier by our group gave 20% higher sound velocities due to insufficient temporal and angular resolution of our XRD setup (Sander *et al.*, 2016).

As depicted in Fig. 2(*a*), we also observe a significant broadening of the LSMO peak after optical excitation. Within the time delay covered in the experiment, thermal transport and heat equilibration do not lead to a significant equilibration of strain within the two layers. Hence, due to the high temporal resolution provided by the PicoSwitch and the high angular resolution provided by the synchrotron, the initial excitation profile directly after absorption of the laser pulse is resolved. The data yield an exponential decay of the strain in the excited LSMO layer with a decay constant of 55 nm^{-1}.

Finally, we discuss the photon flux in the shortened X-ray pulse to check the efficiency of the PicoSwitch. By comparing the integral pulse areas of the original and shortened pulses shown in Fig. 1(*e*), we find an area loss factor ALF = 11.34. The total intensity loss must also account for the finite diffraction η_{on} of 2×10^{-3}. We find a total efficiency of 1.8×10^{-4}. Our measurement was performed with the U17 undulator on ID09 at the ESRF, which delivers 2.1×10^{6} photons per pulse at an energy of $E_0 = 14.85$ keV, a bunch current of 5 mA and a relative bandwith of $\Delta E/E_0 = 0.016\%$. With the above considerations, the photon flux reduces to 3.6×10^{2} photons per pulse.

The calculated initial, final and total contrasts are shown in Fig. 3(*a*) for a monochromatic X-ray pulse. The high-contrast region also determines a limit for the angular stability of the switch. For experiments which tolerate a higher relative bandwidth, the number of photons can be increased almost linearly with the relative bandwidth $\Delta E/E_0$. However, the switching contrast decreases if the relative bandwidth is too large.

The effect of a finite total contrast is demonstrated in Fig. 3(*b*), which again depicts the sampling of the LSMO peak (black dashed line) with a probe pulse of 7.5 ps FWHM and contrasts of 2.93 (red solid line) and 1.35 (blue solid line). The simulated probe pulses are shown in Fig. 3(*c*). Clearly, increasing the bandwidth of the X-ray probe pulse yields a higher photon flux, but it goes hand in hand with a reduced switching contrast. Therefore, the total contrast and intensity of the PicoSwitch probe pulse are related quantities, which allow for adaptation to specific experiments.

We would like to point out again that the PicoSwitch contrast is insufficient for pulse gating. For that, slower photoacoustic transient gratings with diffraction efficiencies of up to 33% may be used (Sander, Herzog *et al.*, 2017; Sander, Pudell *et al.*, 2017). Another parameter for optimizing the experiment and the X-ray flux is to increase the repetition frequency of the PicoSwitch. A successful implementation of the PicoSwitch at a repetition rate of 208 kHz has already been presented (Sander *et al.*, 2016) and operation even above 1 MHz has been tested successfully. Assuming the PicoSwitch is operated at the ESRF orbit frequency of 354 kHz, the

Table 2
Performance parameters of the X-ray beam on ID09, the shortened beam during the experiment and an optimized setting with increased bandwidth and repetition rate.

For the beam size and beam divergence we also list the beamline parameters after the Extremely Brilliant Source (EBS) upgrade.

Parameter	ID09 (ESRF)	PicoSwitch experiment	PicoSwitch optimized
Photons per pulse			
$\Delta E/E_0 = 10^{-4}$	2×10^{6}	3.6×10^{2}	
$\Delta E/E_0 = 10^{-2}$	2×10^{8}		3.6×10^{4}
Photons per second			
At 1 kHz	2×10^{9}	3.6×10^{5}	
At 100 kHz	2×10^{11}		3.6×10^{9}

experimentally derived parameters from the measurement shown in Fig. 2 yield a total X-ray flux of 1.2×10^{8} photons s^{-1}. The main performance parameters of the short-pulse beam are summarized in Table 2, which also provides values for an optimized beamline setting with increased bandwidth and increased repetition frequency. As discussed above, both parameters increase the X-ray flux in the shortened beam. In Table 3 we provide the pulse parameters for other synchrotron-based short-pulse facilities.

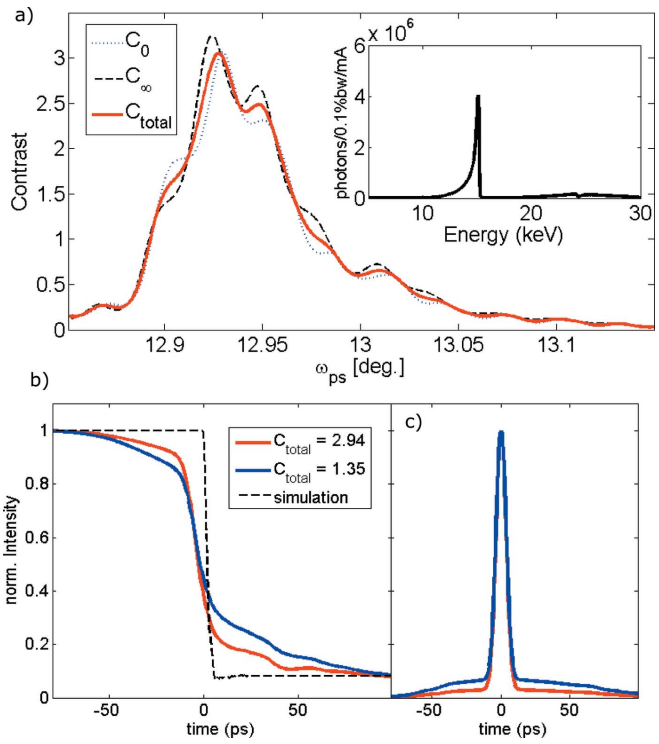

Figure 3
Switching contrast. (*a*) The calculated switching contrast of the PicoSwitch in the grey shaded area of Fig. 1(*c*). The contrast results from the difference in diffraction efficiency in the on and off states of the switch and from the area loss function ALF = 11.34. The inset shows the X-ray spectrum emitted by the U17 undulator on the ID09 beamline. (*b*) Calculated pump–probe signals of an ultrashort step function (black dashed line) with a contrast of 2.94 (red solid line) and 1.35 (blue solid line). The latter contrast is obtained at a ten times higher X-ray bandwidth. (*c*) X-ray probe pulses used for the calculations in panel (*b*).

Table 3
Summary of alternative synchrotron-based sources for picosecond and sub-picosecond X-ray pulses.

Parameter	FemtoMAX[a]	NSLS-II[b]	BESSY VSR[c]
Photons per pulse	1×10^7		
Energy (keV)	1.8–20	1–20	<10
Repetition rate	100 Hz	500 MHz	1.25 MHz
Pulse duration	100 fs	15–30 ps	15 ps to 300 fs

References: (*a*) Enquist *et al.* (2018); (*b*) NSLS-II, https://www.bnl.gov/ps/accelerator/; (*c*) Helmholtz-Zentrum Berlin (2015).

4. Conclusions

In conclusion, we have demonstrated the feasibility of pulse shortening with fast photoacoustic Bragg switches for synchrotron-based pump–probe experiments. Our device, which we call the PicoSwitch, shortens an incident 100 ps long hard X-ray pulse to a duration of 7.5 ps (FWHM). We have defined and quantified the relevant parameters for the pulse duration, efficiency and switching contrast of the PicoSwitch. Even with the rather low efficiency of a 1 kHz setup, our experiment monitors structural dynamics due to propagating sound waves in thin epitaxial films. In particular, we profit from the excellent beam stability and angular resolution of the synchrotron beam, which are not degraded by insertion of the PicoSwitch. In an optimized setup with repetition rates up to 1 MHz and a bandwidth of the X-ray pulse of 0.2%, the PicoSwitch would deliver a flux of more than 10^9 photons s^{-1}. The PicoSwitch is a powerful option for introducing high temporal resolution at the beamline level in synchrotron-based experiments. It may become a valuable tool for time-resolved experiments in current and future large-scale radiation facilities.

Funding information

Funding for this research was provided by: Bundesministerium für Bildung und Forschung (grant No. 05K16GU3); Horizon 2020 XPROBE (grant No. 637295 to Victoria Kabanova and Michael Wulff).

References

Allam, D. S. (1970). *J. Phys. E Sci. Instrum.* **3**, 1022–1023.
Bargheer, M., Zhavoronkov, N., Gritsai, Y., Woo, J. C., Kim, D. S., Woerner, M. & Elsaesser, T. (2004). *Science*, **306**, 1771–1773.
Beaud, P., Johnson, S. L., Streun, A., Abela, R., Abramsohn, D., Grolimund, D., Krasniqi, F., Schmidt, T., Schlott, V. & Ingold, G. (2007). *Phys. Rev. Lett.* **99**, 174801.
Bogdanova, K. G., Bulatov, A. R., Golenishchev-Kutuzov, V. A., Elokhina, L. V., Kapralov, A. V., Korolev, A. V., Neifel'd, A. & Shakirzyanov, M. M. (2003). *Phys. Solid State*, **45**, 298–303.
Bojahr, A., Gohlke, M., Leitenberger, W., Pudell, J., Reinhardt, M., von Reppert, A., Roessle, M., Sander, M., Gaal, P. & Bargheer, M. (2015). *Phys. Rev. Lett.* **115**, 195502.
Bojahr, A., Herzog, M., Mitzscherling, S., Maerten, L., Schick, D., Goldshteyn, J., Leitenberger, W., Shayduk, R., Gaal, P. & Bargheer, M. (2013). *Opt. Express*, **21**, 21188–21197.
Bucksbaum, P. H. & Merlin, R. (1999). *Solid State Commun.* **111**, 535–539.
Cammarata, M., Eybert, L., Ewald, F., Reichenbach, W., Wulff, M., Anfinrud, P., Schotte, F., Plech, A., Kong, Q., Lorenc, M., Lindenau, B., Räbiger, J. & Polachowski, S. (2009). *Rev. Sci. Instrum.* **80**, 015101.
Di Mitri, S. (2018). *J. Synchrotron Rad.* **25**, 1323–1334.
Enquist, H., Jurgilaitis, A., Jarnac, A., Bengtsson, Å. U. J., Burza, M., Curbis, F., Disch, C., Ekström, J. C., Harb, M., Isaksson, L., Kotur, M., Kroon, D., Lindau, F., Mansten, E., Nygaard, J., Persson, A. I. H., Pham, V. T., Rissi, M., Thorin, S., Tu, C.-M., Wallén, E., Wang, X., Werin, S. & Larsson, J. (2018). *J. Synchrotron Rad.* **25**, 570–579.
Gaal, P., Schick, D., Herzog, M., Bojahr, A., Shayduk, R., Goldshteyn, J., Leitenberger, W., Vrejoiu, I., Khakhulin, D., Wulff, M. & Bargheer, M. (2014). *J. Synchrotron Rad.* **21**, 380–385.
Gaal, P., Schick, D., Herzog, M., Bojahr, A., Shayduk, R., Goldshteyn, J., Navirian, H. A., Leitenberger, W., Vrejoiu, I., Khakhulin, D., Wulff, M. & Bargheer, M. (2012). *Appl. Phys. Lett.* **101**, 243106.
Grigoriev, A., Do, D.-H., Kim, D. M., Eom, C.-B., Evans, P. G., Adams, B. & Dufresne, E. M. (2006). *Appl. Phys. Lett.* **89**, 021109.
Helmholtz-Zentrum Berlin (2015). *Technical Design Study BESSY VSR.* https://www.helmholtz-Berlin.de/media/media/angebote/bibliothek/reports/r0001-bessy-vsr-tds.pdf.
Herzog, M., Bojahr, A., Goldshteyn, J., Leitenberger, W., Vrejoiu, I., Khakhulin, D., Wulff, M., Shayduk, R., Gaal, P. & Bargheer, M. (2012). *Appl. Phys. Lett.* **100**, 094101.
Herzog, M., Schick, D., Gaal, P., Shayduk, R., Korff Schmising, C. & Bargheer, M. (2012). *Appl. Phys. A*, **106**, 489–499.
Ingold, G., Beaud, P., Johnson, S., Streun, A., Schmidt, T., Abela, R., Al-Adwan, A., Abramsohn, D., Böge, M., Grolimund, D., Keller, A., Krasniqi, F., Rivkin, L., Rohrer, M., Schilcher, T., Schmidt, T., Schlott, V., Schulz, L., van der Veen, F. & Zimoch, D. (2007). *AIP Conf. Proc.* **879**, 1198–1201.
Jankowiak, A. & Wüstefeld, G. (2013). *Synchrotron Radiat. News*, **26**(3), 22–24.
Larsson, J., Allen, A., Bucksbaum, P., Falcone, R., Lindenberg, A., Naylor, G., Missalla, T., Reis, D., Scheidt, K., Sjogren, A., Sondhauss, P., Wulff, M. & Wark, J. S. (2002). *Appl. Phys. Mater. Sci. Process.* **75**, 467–478.
Michael, P. C., Trefny, J. U. & Yarar, B. (1992). *J. Appl. Phys.* **72**, 107–109.
Navirian, H. A., Herzog, M., Goldshteyn, J., Leitenberger, W., Vrejoiu, I., Khakhulin, D., Wulff, M., Shayduk, R., Gaal, P. & Bargheer, M. (2011). *J. Appl. Phys.* **109**, 126104.
Rose-Petruck, C., Jimenez, R., Guo, T., Cavalleri, A., Siders, C. W., Rksi, F., Squier, J. A., Walker, B. C. Wilson, K. R. & Barty, C. P. J. (1999). *Nature*, **398**, 310–312.
Sander, M., Herzog, M., Pudell, J. E., Bargheer, M., Weinkauf, N., Pedersen, M., Newby, G., Sellmann, J., Schwarzkopf, J., Besse, V., Temnov, V. V. & Gaal, P. (2017). *Phys. Rev. Lett.* **119**, 075901.
Sander, M., Koc, A., Kwamen, C. T., Michaels, H., v, A., Reppert, A., Pudell, J., Zamponi, F., Bargheer, M., Sellmann, J., Schwarzkopf, J. & Gaal, P. (2016). *J. Appl. Phys.* **120**, 193101.
Sander, M., Pudell, J.-E., Herzog, M., Bargheer, M., Bauer, R., Besse, V., Temnov, V. & Gaal, P. (2017). *Appl. Phys. Lett.* **111**, 261903.
Schick, D., Bojahr, A., Herzog, M., Shayduk, R., von Korff Schmising, C. & Bargheer, M. (2014). *Comput. Phys. Commun.* **185**, 651–660.
Schick, D., Bojahr, A., Herzog, M., von Korff Schmising, C., Shayduk, R., Leitenberger, W., Gaal, P. & Bargheer, M. (2012). *Rev. Sci. Instrum.* **83**, 025104.
Schoenlein, R. W., Chattopadhyay, S., Chong, H. H. W., Glover, T. E., Heimann, P. A., Shank, C. V., Zholents, A. A. & Zolotorev, M. S. (2000). *Science*, **287**, 2237–2240.
Schroer, C. G., Agapov, I., Brefeld, W., Brinkmann, R., Chae, Y.-C., Chao, H.-C., Eriksson, M., Keil, J., Nuel Gavaldà, X., Röhlsberger, R., Seeck, O. H., Sprung, M., Tischer, M., Wanzenberg, R. & Weckert, E. (2018). *J. Synchrotron Rad.* **25**, 1277–1290.

Sellmann, J., Schwarzkopf, J., Kwasniewski, A., Schmidbauer, M., Braun, D. & Duk, A. (2014). *Thin Solid Films*, **570**, 107–113.
Shayduk, R., Herzog, M., Bojahr, A., Schick, D., Gaal, P., Leitenberger, W., Navirian, H., Sander, M., Goldshteyn, J., Vrejoiu, I. & Bargheer, M. (2013). *Phys. Rev. B*, **87**, 184301.
Shayduk, R., Pennicard, D., Krausert, K., Gaal, P., Volkov, S., Vonk, V., Hejral, U., Jankowski, M., Reinhardt, M., Leitenberger, W. & Stierle, A. (2017). *J. Synchrotron Rad.* **24**, 1082–1085.
Sheppard, J. M. H., Sondhauss, P., Merlin, R., Bucksbaum, P., Lee, R. W. & Wark, J. S. (2005). *Solid State Commun.* **136**, 181–185.
Thomsen, C., Grahn, H. T., Maris, H. J. & Tauc, J. (1986). *Phys. Rev. B*, **34**, 4129–4138.
Warren, B. (1990). *X-ray Diffraction. Addison–Wesley Series in Metallurgy and Materials Engineering.* New York: Dover Publications.
Zamponi, F., Ansari, Z., Korff Schmising, C., Rothhardt, P., Zhavoronkov, N., Woerner, M., Elsaesser, T., Bargheer, M., Trobitzsch-Ryll, T. & Haschke, M. (2009). *Appl. Phys. A*, **96**, 51–58.
Zolotoyabko, E. & Quintana, J. P. (2004). *Rev. Sci. Instrum.* **75**, 699–708.

Quantitative disentanglement of coherent and incoherent laser-induced surface deformations by time-resolved x-ray reflectivity

M. Sander,[1] J.-E. Pudell,[1] M. Herzog,[1] M. Bargheer,[1,2] R. Bauer,[3] V. Besse,[4] V. Temnov,[5] and P. Gaal[3,a)]

[1]*Institut für Physik und Astronomie, Universität Potsdam, Karl-Liebknecht-Str. 24-25, 14476 Potsdam, Germany*
[2]*Helmholtz-Zentrum Berlin für Materialien und Energie GmbH, Wilhelm-Conrad-Röntgen Campus, BESSY II, Albert-Einstein-Str. 15, 12489 Berlin, Germany*
[3]*Institut für Nanostruktur und Festkörperphysik, Universität Hamburg, Jungiusstr. 11c, 20355, Germany*
[4]*IMMM CNRS 6283, Université du Maine, 72085 Le Mans cedex, France*
[5]*Institute of Molecules and Materials of Le Mans, CNRS UMR 6283, 72085 Le Mans, France*

(Received 13 September 2017; accepted 6 December 2017; published online 28 December 2017)

We present time-resolved x-ray reflectivity measurements on laser excited coherent and incoherent surface deformations of thin metallic films. Based on a kinematical diffraction model, we derive the surface amplitude from the diffracted x-ray intensity and resolve transient surface excursions with sub-Å spatial precision and 70 ps temporal resolution. The analysis allows for decomposition of the surface amplitude into multiple coherent acoustic modes and a substantial contribution from incoherent phonons which constitute the sample heating. *Published by AIP Publishing.*
https://doi.org/10.1063/1.5004522

Ultrafast photoacoustics[1] has become an established method to probe the interaction of optical,[2] electronic,[3] and magnetic[4] properties with the crystal lattice in solids. It employs strain pulses that are generated by absorption of femtosecond light pulses in an optoacoustic transducer.[5] Subsequent lattice dynamics can be probed either optically or by ultrafast x-ray diffraction.[6] Nowadays, tailored longitudinal strain waves can be generated and monitored using time-resolved optical and x-ray techniques.[1,7,8] Mode selective excitation of coherent acoustic surface modes can be achieved with a Transient Grating (TG) technique.[9] In addition to Rayleigh-like Surface Acoustic Waves (SAWs), this method also excites so-called Surface Skimming Longitudinal Waves (SSLWs).[10,11] However, in any photoacoustic experiment, the main fraction of the deposited optical energy is stored in incoherent phonon excitations.[12,13] The absolute magnitude of the coherent and incoherent excitation is hard to determine from purely optical experiments. In this paper, we perform a full decomposition of optically excited coherent acoustic surface and longitudinal waves which propagate with their respective group velocities and the concomitant thermal phonons which move only by diffusion. Our method allows for measuring the absolute deformation of a solid surface using time-resolved x-ray reflectivity (TR-XRR). This method can resolve surface deformation with sub-Å spatial and 70 ps temporal resolution.

The experiments were performed at the ID09 beamline of the European Synchrotron Radiation Facility (ESRF) in Grenoble, France. The beamline is equipped with a commercial Ti:Sapphire laser amplifier (Coherent Legend) which delivers 800 nm optical pulses with a duration of 600 fs at a repetition rate of 1 kHz. The laser is synchronized to the storage ring to allow for tuning the pump-probe delay with a precision of better than 5 ps.

The optical excitation pulses are coupled into the transient grating (TG) setup shown in Fig. 1 to produce +1 and −1 diffraction order from a series of transmission phase gratings with various spatial periods Λ'. Both diffracted beams are imaged onto the sample surface using a cylindrical (CL) and spherical (SL) lens in 4*f*-geometry with focal lengths $f_{CL} = 75$ mm and $f_{SL} = 150$ mm, respectively. Interference of

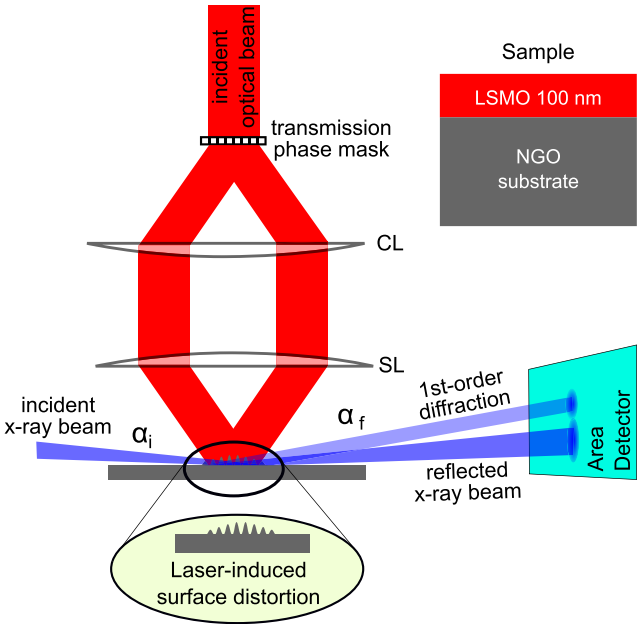

FIG. 1. Experimental setup installed at the ID09 beamline at the ESRF: Transient optical gratings are generated by splitting the output of a femtosecond laser system using a transmission phase mask and combining +1 and −1 order of the optical beam on the sample surface with a cylindrical (CL) and spherical (SL) lens in 4*f*-geometry. The surface is probed with 70 ps x-ray pulse impinging the sample at grazing incidence angle α_i. The specular beam is reflected at the exit angle α_f and the first order diffraction at $\alpha_f + \delta\alpha$. We measure TR-XRR in a pump-probe scheme. A schematic of the LSMO/NGO sample structure is shown at the top.

a)Electronic mail: pgaal@physnet.uni-hamburg.de

both beams at the sample surface results in a spatial light intensity distribution with spatial period $\Lambda = \Lambda' f_{SL}/f_{CL}$ which is determined by the phase grating period and the optical magnification of the setup. We define the associated wavevector $q_{\parallel} = 2\pi/\Lambda$ which lies within both the sample surface and the x-ray diffraction plane. The optical setup results in a laser profile envelope at the sample surface with full-width at half maximum of 30 μm and 4 mm.

The sample is probed by 70 ps x-ray pulses with a photon energy of 15 keV ($\lambda_{\text{x-ray}} = 0.8266$ Å) which impinge the surface with a wavevector $\vec{k}_i$ at an incidence angle of $\alpha_i = 0.15°$, i.e., below the critical angle of total reflection. The x-ray footprint on the sample in our experiment was 10 μm × 1 mm, thus assuring overlap in a homogeneously excited sample area. The area detector image shows two pronounced peaks. The first peak originates from specular reflection of the incident beam at the sample surface $\vec{k}_f = \vec{k}_i + \vec{q}_{\perp}$, where $\vec{q}_{\perp} = 2\vec{k}_i \sin(\alpha_i)$ is the recoil momentum due to total reflection. The second peak is offset by an angle $\delta\alpha$ which results from the momentum transfer $\vec{q}_{\parallel}$ according to the laser-induced surface distortion. Hence, we call this peak the first-order diffraction from the laser-induced transient surface grating. In the following, we investigate the temporal evolution of this first order peak.

The investigated sample consists of 100 nm Lanthanum Strontium Manganate (LSMO) on a Neodym Gallate (NGO) substrate. It was grown by pulsed laser deposition.[14] The substrate is transparent at the wavelength of the excitation laser. Hence, the optical pump pulses are absorbed exclusively in the metallic LSMO film.

Experimental data of the LSMO/NGO sample for an absorbed pump fluence of 28 mJ/cm^2 are shown in Fig. 2(a). The plot depicts the intensity change of the +1st-order diffraction vs. pump-probe delay $(I(\tau) - I_0)/I_0 = \Delta I/I_0$. Upon optical excitation, we observe an instantaneous rise of the diffracted intensity within the temporal resolution of the experiment. The initial rise is followed by a slight intensity decay which lasts for approximately 150 ps. The decay is followed by a signal increase which peaks at a pump-probe delay of approximately 800 ps and subsequently oscillates around an intensity offset with constant amplitude.

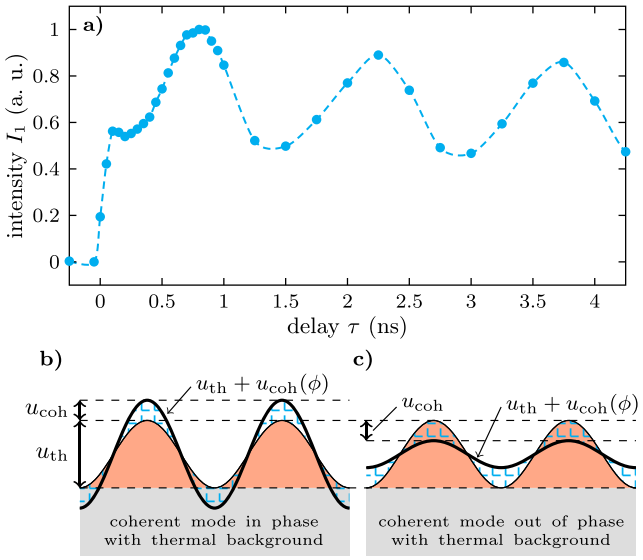

FIG. 2. (a) TR-XRR measurement of laser-generated transient surface deformations of a LSMO/NGO sample excited with 28 mJ/cm^2. The dotted line is a guide to the eye. (b) and (c) Visualization of coherent and incoherent surface dynamics: the surface amplitude is modulated by constructive and destructive interference, respectively, of the periodic thermal grating and the propagating acoustic modes.

The time dependence of a similar TR-XRR measurement on a different sample was recently discussed in detail.[8] Briefly, the time-resolved data can be identified to be due to a periodic surface excursion with time-dependent amplitude $u(\tau)$ described by

$$u(\tau) = u_{th} \cdot e^{-\alpha_{th}\tau} + u_{SAW} \cdot \cos(\omega_{SAW}\tau + \varphi_{SAW}) + u_{SSLW} \cdot \cos(\omega_{SSLW}\tau + \varphi_{SSLW}) \cdot e^{-\alpha_{SSLW}\tau}. \quad (1)$$

Absorption of the ultrashort light pulse in the sample results in two fundamentally different processes. First, the sample is heated locally in the excitation area, which results in a periodic thermal expansion of the surface with amplitude u_{th}.[15] In addition, the impulsive optical excitation launches coherent strain waves which propagate parallel and perpendicular to the sample surface[7,16,17] and consist of two independent modes with surface displacement amplitudes $u_{SAW/SSLW}$, frequencies $\omega_{SAW/SSLW}$, and phases $\varphi_{SAW/SSLW}$, respectively. The thermal grating decays on a timescale $1/\alpha_{th} \approx 100$ ns by in-plane thermal diffusion, a process which is much slower than the measurement range in our experiment. The SSLW mode is strongly damped with decay constant α_{SSLW}, whereas the SAW mode exhibits no decay within our measurement window. A visualization of this decomposition is depicted in Figs. 2(b) and 2(c). Figure 2(b) depicts constructive spatial interference of the coherent modes with the thermal grating. Figure 2(c) shows a situation where the thermal grating and the coherent modes are spatially in the opposite phase. Hence, both excitations interfere destructively. The interplay of coherent and incoherent excitations can be exploited for spatio-temporal control of the surface excursion.[8]

Here, we explicitly analyze the TR-XRR probing mechanism to derive a diffraction model which relates the diffracted intensity $I(\tau)$ to the amplitude u of the surface excursion. A spatial period of the distorted sample is shown in Fig. 3(a). An x-ray beam impinges the sample at an incidence angle α_i in the bottom (point A) and on the top (point B) of the distortion and is reflected with an exit angle α_f. After reflection from A, the beam travels an additional path length X_1, while the other beam travels an additional path X_2 before reflection from point B. The total path difference results in a relative phase of both beams of $\Delta\phi = \frac{2\pi}{\lambda x-ray} \cdot (X_2 - X_1)$. $\Delta\phi$ can be calculated using the following set of equations:

$$X_1 = \sqrt{u^2 + (\Lambda/2)^2} \cdot \cos(\gamma), \quad (2)$$

$$X_2 = \sqrt{u^2 + (\Lambda/2)^2} \cdot \sin(\eta), \quad (3)$$

$$\gamma = \alpha_f - \tan^{-1}(2u/\Lambda), \quad (4)$$

$$\eta = \pi/2 - \alpha_i - \tan^{-1}(2u/\Lambda), \quad (5)$$

and the grating equation for constructive interference:

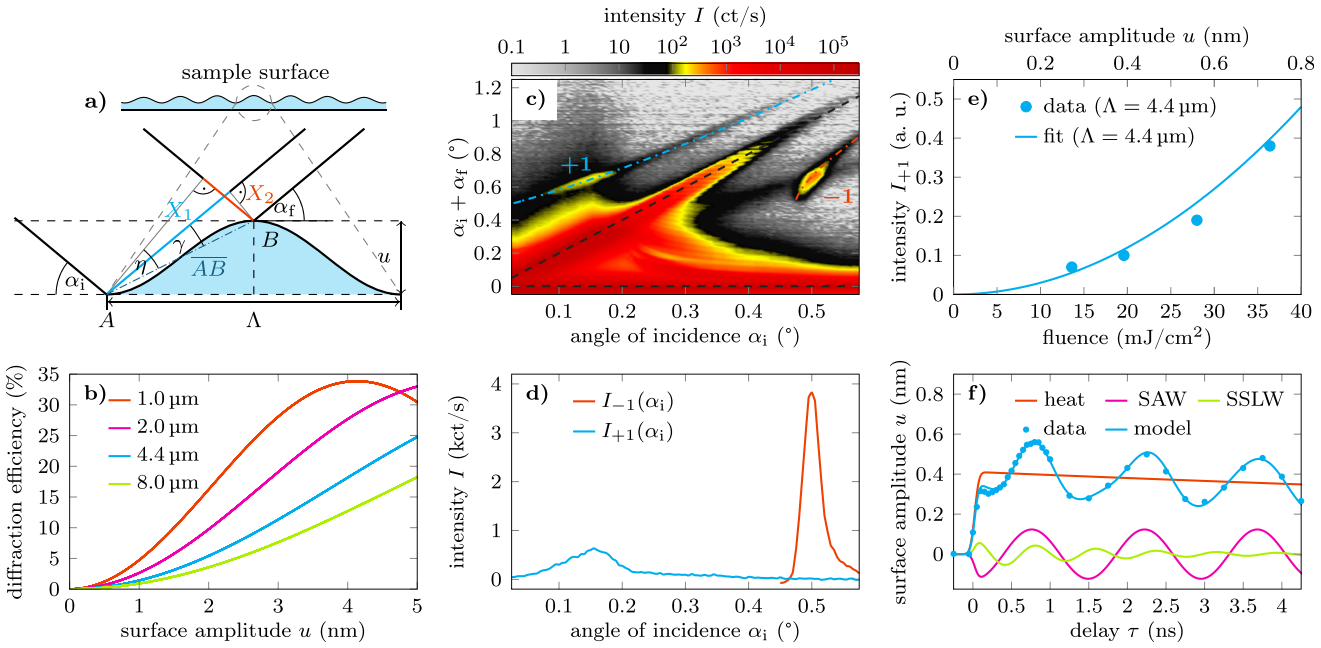

FIG. 3. (a) Schematic for the diffraction model given by Eqs. (2)–(5). (b) Relative diffraction efficiency vs. surface excursion for grating periods of $\Lambda = 8.0\,\mu$m (green), 4.4 μm (blue), 2.0 μm (magenta), and 1.0 μm (orange). (c) Angle-resolved diffracted intensity vs. incidence angle α_i. The specular reflection (black dashed line) and +1st and −1st order diffraction from the surface grating (blue and red dashed lines) are indicated. (d) Intensity along the +1st and −1st diffraction order, i.e., along the colored dashed lines in (c). (e) Diffracted intensity (symbols) vs. absorbed pump fluence (bottom) and surface amplitude (top). The solid line shows a quadratic dependence of the diffracted intensity as expected from Eq. (9). (f) Decomposition of the diffraction data for an absorbed pump fluence of 28 mJ/cm^2. The amplitude of the individual components is given in the absolute scale.

$$\eta\lambda_{\mathrm{x-ray}} = \Lambda(\cos(\alpha_f) - \cos(\alpha_i)). \tag{6}$$

From kinematical theory of surface diffraction,[18,19] we find the following expression for the diffraction intensity of n-th order from a periodically distorted surface for incidence angles below the critical angle $\alpha_i < \alpha_c$, i.e., from a pure phase grating,

$$I_n = \left| \frac{1}{r_0} \int_{\parallel} e^{-i\left(nq_{\parallel}r_{\parallel} + \frac{\Delta\varphi}{2}\sin\left(\frac{2\pi}{\Lambda}r_{\parallel}\right)\right)} \mathrm{d}r_{\parallel} \right|^2, \tag{7}$$

$$= \left| J_n\left(\frac{\Delta\varphi}{2}\right) \right|^2, \tag{8}$$

where $r_{\parallel}$ is the spatial coordinate along the surface grating, r_0 is a normalization constant, and J_n is the n-th Bessel function. The argument of the Bessel function is the modulation of the phase difference due to variation of the grating surface amplitude $\Delta\varphi = \Delta\phi - n\pi$, where $n\pi$ is the phase shift due to n-th order diffraction. For all practical purposes, we can assume that the surface amplitude is much smaller than the period of the surface grating, i.e., $u \ll \Lambda/2$ and therefore $\sqrt{u^2 + (\Lambda/2)^2} \approx \frac{\Lambda}{2}\left(1 + \frac{2u^2}{\Lambda^2}\right)$ and $\tan^{-1}\left(\frac{2u}{\Lambda}\right) \simeq \tan\left(\frac{2u}{\Lambda}\right) \simeq \frac{2u}{\Lambda}$. For grazing incidence $\alpha_i \leq \alpha_c$, the phase difference $\Delta\varphi$ is approximately given by

$$\Delta\varphi = -2\pi\frac{u}{\lambda_{\mathrm{x-ray}}}\alpha_i\left[1 + \sqrt{1 + \frac{2n\lambda_{\mathrm{x-ray}}}{\Lambda\alpha_i^2}}\right]. \tag{9}$$

The results of the diffraction model laid out by Eqs. (2)–(8) are presented in Fig. 3(b). We plot the normalized diffracted first-order intensity I_1 vs. the surface excursion u for spatial grating periods $\Lambda = 8.0\,\mu$m (pink), 4.4 μm (blue), 2.0 μm (green), and 1.0 μm (red). The diffraction efficiency increases with increasing surface excursion and with decreasing spatial period Λ. The maximum diffraction efficiency is 33%, i.e., the maximum of the Bessel function shown in Fig. 3(b). Experimental data are shown in Fig. 3(c) which depicts the diffracted intensity from the sample vs. incidence angle α_i. The specular reflection and the ±1st-order diffraction are marked by dashed lines. Integrated intensity of the +1st (blue) and −1st diffraction order is shown in Fig. 3(d). The integration was performed along the colored dashed lines in panel 3(c).

The fluence dependence of the +1st diffraction order intensity from a laser-generated surface grating with spatial period $\Lambda = 4.4\,\mu$m is depicted in Fig. 3(e). The symbols indicate the measured maximum diffracted intensity at 800 ps time delay vs. absorbed pump fluence. The total surface excursion at this time delay is the sum of a thermal grating and coherent sound waves with an out-of-plane polarization component [see Fig. 2(b)]. Using recent time-resolved x-ray diffraction data from a similar LSMO sample,[20] a calibration factor for the laser-generated layer strain under the given circumstances can be estimated to be approx. 0.02% per mJ/cm^2.[21] Taking into account the LSMO layer thickness of 100 nm, the experimental fluence can thus be converted to a total surface excursion which is given at the top abscissa of Fig. 3(e). The solid line shows results from our diffraction model presented in Eqs. (2)–(5). The experimental data show the expected quadratic dependence as derived from Eq. (9).

The time-resolved surface dynamics upon transient grating excitation is shown in Fig. 3(f). By taking the square root of the diffracted intensity, i.e., data shown in Fig. 2(a), we

depict the surface excursion on an absolute length scale. Experimental data (symbols) are decomposed into a slowly decaying thermal grating (red), a Rayleigh-like SAW mode (magenta), and a SSLW-mode (green), respectively. The solid blue line shows the time-dependent surface dynamics given as described by Eq. (1), showing excellent agreement with the experimental curve.

In conclusion, we measure the absolute amplitude of the surface excursion of a laser-induced transient grating on a solid surface by time-resolved x-ray reflectivity. Ultrafast optical excitation generates incoherent thermal surface distortions and coherent acoustic surface waves. The measured dynamics at the surface allow for a decomposition of the surface amplitude in a thermal background and two coherent acoustic modes: a Rayleigh-like surface acoustic wave and a surface skimming longitudinal wave. Our method can be applied to decompose coherent and incoherent surface dynamics with sub-Å precision and with a temporal resolution better than 100 ps.

The experiments were performed at the beamline ID09 of the European Synchrotron Radiation Facility (ESRF), Grenoble, France. We are grateful to Gemma Newby, Martin Pedersen, and Micheal Wulff for providing assistance in using beamline ID09. We also thank Jutta Schwarzkopf for preparation of the sample. We acknowledge financial support from BMBF via 05K16GU3, from *Stratégie Internationale* "NNN-Telecom" de la Région Pays de La Loire, ANR-DFG "PPMI-NANO" (ANR-15-CE24-0032 and DFG SE2443/2), and from DFG via BA2281/8-1.

[1]P. Ruello and V. E. Gusev, Ultrasonics **56**, 21 (2015).
[2]M. Weiß, J. B. Kinzel, F. J. R. Schülein, M. Heigl, D. Rudolph, S. Morkötter, M. Döblinger, M. Bichler, G. Abstreiter, J. J. Finley, G. Koblmüller, A. Wixforth, and H. J. Krenner, Nano Lett. **14**, 2256 (2014).
[3]Y. Wang, Y. Chen, H. Li, X. Li, H. Chen, H. Su, Y. Lin, Y. Xu, G. Song, and X. Feng, ACS Nano **10**, 8199 (2016).
[4]J.-W. Kim, M. Vomir, and J.-Y. Bigot, Phys. Rev. Lett. **109**, 166601 (2012).
[5]C. Thomsen, H. T. Grahn, H. J. Maris, and J. Tauc, Phys. Rev. B **34**, 4129 (1986).
[6]C. Rose-Petruck, R. Jimenez, T. Guo, A. Cavalleri, C. W. Siders, F. Rksi, J. A. Squier, B. C. Walker, K. R. Wilson, and C. P. J. Barty, Nature **398**, 310 (1999).
[7]M. Herzog, A. Bojahr, J. Goldshteyn, W. Leitenberger, I. Vrejoiu, D. Khakhulin, M. Wulff, R. Shayduk, P. Gaal, and M. Bargheer, Appl. Phys. Lett. **100**, 094101 (2012).
[8]M. Sander, M. Herzog, J. E. Pudell, M. Bargheer, N. Weinkauf, M. Pedersen, G. Newby, J. Sellmann, J. Schwarzkopf, V. Besse, V. V. Temnov, and P. Gaal, Phys. Rev. Lett. **119**, 075901 (2017).
[9]J. A. Rogers, A. A. Maznev, M. J. Banet, and K. A. Nelson, Annu. Rev. Mater. Sci. **30**, 117 (2000).
[10]J. Janusonis, T. Jansma, C. L. Chang, Q. Liu, A. Gatilova, A. M. Lomonosov, V. Shalagatskyi, T. Pezeril, V. V. Temnov, and R. Tobey, Sci. Rep. **6**, 29143 (2016).
[11]J. Janušonis, C. L. Chang, T. Jansma, A. Gatilova, V. S. Vlasov, A. M. Lomonosov, V. V. Temnov, and R. I. Tobey, Phys. Rev. B **94**, 024415 (2016).
[12]M. Herzog, D. Schick, P. Gaal, R. Shayduk, C. von Korff Schmising, and M. Bargheer, Appl. Phys. A **106**, 489 (2012).
[13]R. Shayduk, H. A. Navirian, W. Leitenberger, J. Goldshteyn, I. Vrejoiu, M. Weinelt, P. Gaal, M. Herzog, C. V. Korff Schmising, and M. Bargheer, New J. Phys. **13**, 093032 (2011).
[14]J. Sellmann, J. Schwarzkopf, A. Kwasniewski, M. Schmidbauer, D. Braun, and A. Duk, Thin Solid Films **570**(Part A), 107 (2014).
[15]M. Reinhardt, A. Koc, W. Leitenberger, P. Gaal, and M. Bargheer, J. Synchrotron Radiat. **23**(2), 474 (2016).
[16]A. Bojahr, M. Herzog, S. Mitzscherling, L. Maerten, D. Schick, J. Goldshteyn, W. Leitenberger, R. Shayduk, P. Gaal, and M. Bargheer, Opt. Express **21**, 21188 (2013).
[17]R. Shayduk, M. Herzog, A. Bojahr, D. Schick, P. Gaal, W. Leitenberger, H. Navirian, M. Sander, J. Goldshteyn, I. Vrejoiu, and M. Bargheer, Phys. Rev. B **87**, 184301 (2013).
[18]A. Madsen, T. Seydel, M. Tolan, and G. Grübel, J. Synchrotron Radiat. **12**, 786 (2005).
[19]J.-D. Nicolas, T. Reusch, M. Osterhoff, M. Sprung, F. J. R. Schülein, H. J. Krenner, A. Wixforth, and T. Salditt, J. Appl. Crystallogr. **47**, 1596 (2014).
[20]A. Bojahr, M. Herzog, D. Schick, I. Vrejoiu, and M. Bargheer, Phys. Rev. B **86**, 144306 (2012).
[21]Note that the calibration factor given in Ref. 20 refers to the incident fluence instead of the absorbed fluence and accounts only for the thermal component. At 800 ps the in-phase coherent modes require an enhanced calibration factor of 0.02% per mJ/cm^2 which is applied in Fig. 3(e).

Full Spatiotemporal Control of Laser-Excited Periodic Surface Deformations

J.-E. Pudell,[1] M. Sander,[2] R. Bauer,[3] M. Bargheer,[1,4] M. Herzog,[1,*] and P. Gaal[3,†]

[1] *Institut für Physik und Astronomie, Universität Potsdam, 14476 Potsdam, Germany*

[2] *European Synchrotron Radiation Facility (ESRF), 23800 Grenoble, France*

[3] *Institut für Nanostruktur und Festkörperphysik, Universität Hamburg, 20355 Hamburg, Germany*

[4] *Helmholtz-Zentrum Berlin für Materialien und Energie GmbH, Wilhelm-Conrad-Röntgen Campus, BESSY II, 12489 Berlin, Germany*

(Received 24 January 2019; revised manuscript received 12 June 2019; published 19 August 2019)

We demonstrate full control of acoustic and thermal periodic deformations at solid surfaces down to subnanosecond time scales and few-micrometer length scales via independent variation of the temporal and spatial phase of two optical transient grating (TG) excitations. For this purpose, we introduce an experimental setup that exerts control of the spatial phase of subsequent time-delayed TG excitations depending on their polarization state. Specific exemplary coherent control cases are discussed theoretically and corresponding experimental data are presented in which time-resolved x-ray reflectivity measures the spatiotemporal surface distortion of nanolayered heterostructures. Finally, we discuss examples where the application of our method may enable the control of functional material properties via tailored spatiotemporal strain fields.

DOI: 10.1103/PhysRevApplied.12.024036

I. INTRODUCTION

Ultrashort strain pulses can be generated by absorption of femtosecond or picosecond optical light pulses in solids and nanostructures [1,2]. This photoacoustic generation is employed to study properties of phonons in solids [3,4] or the interaction of lattice strain with optic [5], electronic [6], or magnetic [7,8] degrees of freedom. The various interaction channels suggest that lattice strain may be used as a functional tool to control and trigger specific processes and functions in materials. Recently, the control and enhancement of quantum entanglement using tailored surface acoustic waves was suggested [9]. In fact, thanks to their customizable short length and time scales down to a few nanometers and picoseconds, respectively, optically generated strain pulses may be particularly suited for selective excitation of nanostructures. However, a high level of control of the shape, frequency, lifetime, etc., of lattice strain is necessary before strain pulses can be used as functional tools for device operation. The control is typically gained by tailoring the temporal excitation sequence [10–13]. We recently demonstrated strain control on subnanosecond time scales by exploiting spatial variation of transient grating excitation sequences [14]. This method is not only limited to the control of coherent strain pulses but also applies to thermal deformations. In particular, the control of thermal deformations can be applied on the same time scale as the control of coherent excitations. Hence, thermal strain, which is often regarded as an undesired side effect to optical excitations, can now be used to trigger specific material functions.

In this article, we present a comprehensive discussion of spatiotemporal control of acoustic and thermal excitations in solids. Our method relies on shaping the temporal and spatial sequence of optical excitations using the so-called transient grating (TG) technique. In particular, our experimental TG setup allows for easy tuning of the relative spatial phase of subsequent TG excitations. The periodic surface deformation (PSD) of the sample upon optical excitation is detected using time-resolved x-ray reflectivity (TRXRR) [15]. The article provides a detailed discussion of spatiotemporal coherent control with particular focus on important limiting cases in Sec. II. Also, the quantitative probing of PSDs by diffraction of x rays in x-ray reflection geometry is briefly explained. The optical setup for generating and controlling PSDs is presented in Sec. III. In Sec. IV, we discuss results of spatiotemporal coherent control measurements on thermal and acoustic PSDs in nanoscopic heterostructures. We analyze and decompose the experimental data by comparison to an empirical modeling. Section V exemplifies how the strain-control capabilities our method may be exploited in order to control functional material properties. Finally, Sec. VI summarizes and emphasizes the main results.

*marc.herzog@uni-potsdam.de

†pgaal@physnet.uni-hamburg.de

II. COHERENT CONTROL OF PERIODIC SURFACE DEFORMATIONS

Classical coherent control can be performed on any oscillator or wavelike harmonic excitation due to the superposition principle. Without restriction of the general validity, we restrict our considerations to an impulsive and displacive excitation of modes by an ultrashort excitation pulse [16]; i.e., the dynamics of the involved modes is much slower than the excitation pulse duration and the coherent oscillation occurs around a displaced equilibrium. The oscillation amplitude of such an impulsively excited harmonic oscillator can either be suppressed or doubled by a second identical excitation with a relative time delay τ of a half-period (relative phase $\phi = \pi$) or a full period ($\phi = 2\pi$), respectively. This type of coherent control has been successfully applied to various phenomena such as phonons [17–20], magnons [21–23], phonon-polaritons [24], and surface acoustic waves (SAWs) [14,25–27]. In displacive excitations, coherent control is limited to the oscillatory motion, i.e., the coherent part of the system response. The displacement from the equilibrium ground state, which for optical excitations corresponds to a heating of the sample due to the absorbed optical energy, is typically ignored in the coherent control experiments, although it may contain most of the absorbed energy [28].

In addition to the temporal coherence exploited in earlier coherent control experiments, an impulsive TG excitation also possesses a spatial coherence in the form of a sinusoidal intensity variation with spatial period Λ, which is typically oriented parallel to the sample surface. Assuming a linear response of the sample, the absorption of optical energy thus generates a spatially periodic energy density along the sample surface with periodicity Λ. The depth profile of the absorbed energy density is dictated by either the optical properties of the sample or the sample dimensions. In the following, we consider a thermoelastic excitation; i.e., the absorbed energy density results in a mechanical stress that eventually gives rise to a thermal transient grating (TTG). Given the impulsive excitation with ultrashort laser pulses, the thermoelastic stress also launches coherent counterpropagating SAWs, resulting in a standing SAW in the optically excited area. Both excitations can be associated with the characteristic wave vector $|\vec{q}_\parallel| = 2\pi/\Lambda$. The spatial coherence introduces an additional coherent control coordinate given by the spatial phase of the TG excitation [14]. Hence, a second TG excitation with a spatial phase φ_x relative to the first TG excitation can be employed to control the relative spatial phase ϕ_{th} of the corresponding TTGs. Choosing $\phi_{\mathrm{th}} = 2n\pi$ or $\phi_{\mathrm{th}} = (2n-1)\pi$ either amplifies or suppresses the TTG, respectively. Here, the relative spatial phase of the TG excitation patterns directly determines the relative spatial phase of the TTGs, i.e., $\phi_{\mathrm{th}} = \varphi_x$. The coherent SAW, however, is controlled via the spatiotemporal phase $\phi_{\mathrm{SAW}} = \varphi_x + \varphi_t = \varphi_x + v_{\mathrm{SAW}}|\vec{q}_\parallel|\tau$, where v_{SAW} is the phase velocity of the excited SAW and τ is the temporal delay between the two TG excitation pulses. Similar to the TTG, the SAW can be amplified ($\phi_{\mathrm{SAW}} = 2n\pi$) or suppressed [$\phi_{\mathrm{SAW}} = (2n-1)\pi$]. According to the definition of ϕ_{SAW}, a change in the relative spatial phase φ_x implies an adopted time delay τ if the interference of the SAWs is to be kept unchanged. In summary, we introduce two experimental coherent control coordinates φ_x and φ_t given by the relative spatial phase and the relative time delay of two consecutive TG excitations in order to control the thermal and coherent PSD via the spatiotemporal phases ϕ_{th} and ϕ_{SAW}.

In this article, we employ these coherent control coordinates to disentangle four extreme cases of coherent control, which are depicted in Fig. 1:

A. Constructive interference of TTGs and constructive interference of two standing SAWs: $\varphi_x = 0, \varphi_t = 0 \rightarrow \phi_{\mathrm{th}} = 0, \phi_{\mathrm{SAW}} = 0$ [Fig. 1(a)].

B. Destructive interference of TTGs and destructive interference of two standing SAWs: $\varphi_x = \pi,\ \varphi_t = 0 \rightarrow \phi_{\mathrm{th}} = \pi, \phi_{\mathrm{SAW}} = \pi$ [Fig. 1(b)].

C. Constructive interference of TTGs and destructive interference of two standing SAWs: $\varphi_x = 0,\ \varphi_t = \pi \rightarrow \phi_{\mathrm{th}} = 0, \phi_{\mathrm{SAW}} = \pi$ [Fig. 1(c)].

D. Destructive interference of TTGs and constructive interference of two standing SAWs: $\varphi_x = \pi,\ \varphi_t = \pi \rightarrow \phi_{\mathrm{th}} = \pi, \phi_{\mathrm{SAW}} = 2\pi \equiv 0$ [Fig. 1(d)].

Note that, while there is no SAW oscillation present in cases B and C, the SAW modulates the surface deformation of a TTG or a flat surface in cases A and D, respectively, as indicated by the blue shading in Figs. 1(a)–1(d). As discussed below, TRXRR can unambiguously distinguish these situations as they manifest differently in the experimental data. Note that we assume two identical excitations in accordance with a time-independent TTG. The amplitude of the second TG excitation may of course be adapted to compensate for a potential decay of the first excitation during the time delay τ.

In the following, we briefly discuss the detection of dynamics triggered by the TG excitation. Typically, experiments employ an optical laser pulse that is diffracted from the excited modes via photothermal or photoelastic effects [29,30]. Alternatively, PSDs can be detected using x-ray diffraction and photoemission electron microscopy techniques [31–33]. We have recently shown that the PSD associated with the excited quasistatic and transient modes may also be probed by TRXRR [14,15]. This method is exclusively sensitive to the surface displacement and can detect deformations of only a few nanometers [14]. Thermally induced expansion can be

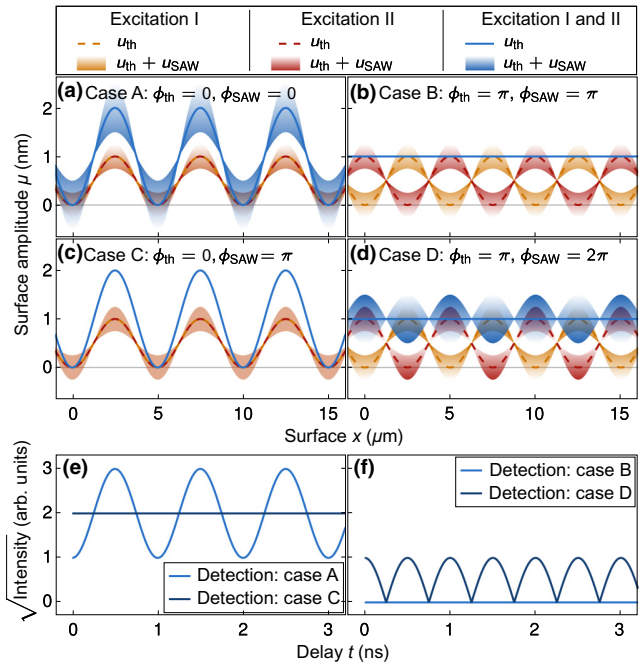

FIG. 1. Spatiotemporal coherent surface control with two tailored excitations: yellow and red dashed lines depict quasistatic TTGs of the individual excitations I and II, respectively. The gradient of the colored shaded areas represents the temporal evolution of the standing SAW on the TTG over a half-period. Blue lines and blue colored areas represent the combined excitation (excitation I & II). (a) Case A: constructive interference of two TTGs and constructive interference of two standing SAWs. Note that both excitations have the same spatiotemporal phase; therefore, the shaded area is orange. (b) Case B: destructive interference of two TTGs and destructive interference of two standing SAWs. (c) Case C: constructive interference of two TTGs and destructive interference of two standing SAWs. Note that both excitations have the same spatial phase and opposite temporal phase; therefore, the shaded area is orange without a color gradient. (d) Case D: destructive interference of two TTGs and constructive interference of two standing SAWs. (e),(f) Square root of the diffracted intensity from the combined excitation for (e) cases A and C and (f) cases B and D. Note that, for x rays, the square root of the intensity is proportional to the surface modulation amplitude.

unambiguously disentangled from coherent elastic effects via the characteristic time scale of the surface deformation [15], thus yielding a complete picture of the surface dynamics. For the TRXRR probe, the Laue condition, i.e., momentum conservation, must be fulfilled:

$$\vec{k}_{\pm 1} = \vec{k}_{\mathrm{in}} + \vec{q}_{\perp} \pm \vec{q}_{\parallel}, \tag{1}$$

where $\vec{k}_{\mathrm{in}}$ and $\vec{q}_{\perp}$ are the wave vector of the incident probe photons and the recoil momentum due to reflection at the surface, respectively. We restrict our considerations to first-order diffraction from the PSD, although diffraction to higher orders is also present, even if a perfect sinusoidal PSD is monitored [15]. Note that Eq. (1) is independent of the spatial phase of the TG; i.e., the phase of the PSD cannot be inferred from the diffracted intensity *per se*. The intensity of the diffracted x-ray probe pulse is proportional to $\Delta u^2(t)$, i.e., to the squared difference between the minimum and maximum surface deformation [15]. Thus, the square root of the diffracted intensity measures the magnitude of the total surface modulation amplitude, i.e., $\sqrt{I(t)} = |\Delta u(t)| = |\Delta u_{\mathrm{th}} + \Delta u_{\mathrm{SAW}} \cos(\omega t)|$, where $\omega = v_{\mathrm{SAW}}|q_{\parallel}|$ is the frequency of the SAW.

First, consider the case where a strong TTG is modulated by a SAW with relatively small amplitude, i.e., $\Delta u_{\mathrm{SAW}} < \Delta u_{\mathrm{th}}$. Excluding thermal diffusion within the TTG, $\Delta u(t) > 0$ holds for all times and the measured signal directly reveals the SAW's frequency and its relative phase with respect to the TTG as depicted in Fig. 1(e). However, if $\Delta u_{\mathrm{SAW}} > \Delta u_{\mathrm{th}}$, the detection signal is altered. The extreme case is shown in Fig. 1(d), where the SAW modulates a flat surface (case D), i.e., $\Delta u_{\mathrm{th}} = 0$ (note that $u_{\mathrm{th}} \neq 0$ may hold). Here, the time-dependent intensity is proportional to $\Delta u^2(t) = [\Delta u_{\mathrm{SAW}} \cos(\omega t)]^2 = \Delta u_{\mathrm{SAW}}^2 [1 + \cos(2\omega t)]/2$. Therefore, the diffracted probe intensity shows twice the frequency of the SAW as presented in Fig. 1(f). The effect of the TTG is analogous to a spatial local oscillator, which allows us to infer the spatiotemporal phase of the coherent SAW from the diffracted probe pulse after TG excitation.

III. EXPERIMENTAL METHODS

A detailed view of our optical experimental setup is shown in Figs. 2(a)–2(e). The general layout of the TG setup is described elsewhere [14,34]. Our particular setup is designed for optical pump TRXRR probe measurements at the ID09 beamline at the European Synchrotron Radiation Facility (ESRF). Taking into account the specific conditions at the beamline, we optimize the optical setup for small size, stability, and tunability. Therefore, we use two 50-mm-wide acylindrical lenses with a focal length of 40 mm to image the +1st and −1st diffraction order from a transmission phase mask onto the sample surface. Interference of the +1 and −1 beam at the sample surface results in a sinusoidal modulation of the optical intensity. Grating, lenses, and sample are mounted in 4f geometry. We optionally introduce an additional cylindrical lens with a focal length of 75.6 mm in the perpendicular plane. This lens is mounted with variable distance to the sample to generate higher excitation fluences.

To generate two replica of an ultrashort optical pump pulse with perpendicular polarization for coherent control, we use a Michelson interferometer [cf. Fig. 2(b)] with a polarizing beamsplitter (PBS). The relative intensity of the pulses can be tuned by a half-wave plate (HWP) in front of the PBS. Each arm of the Michelson

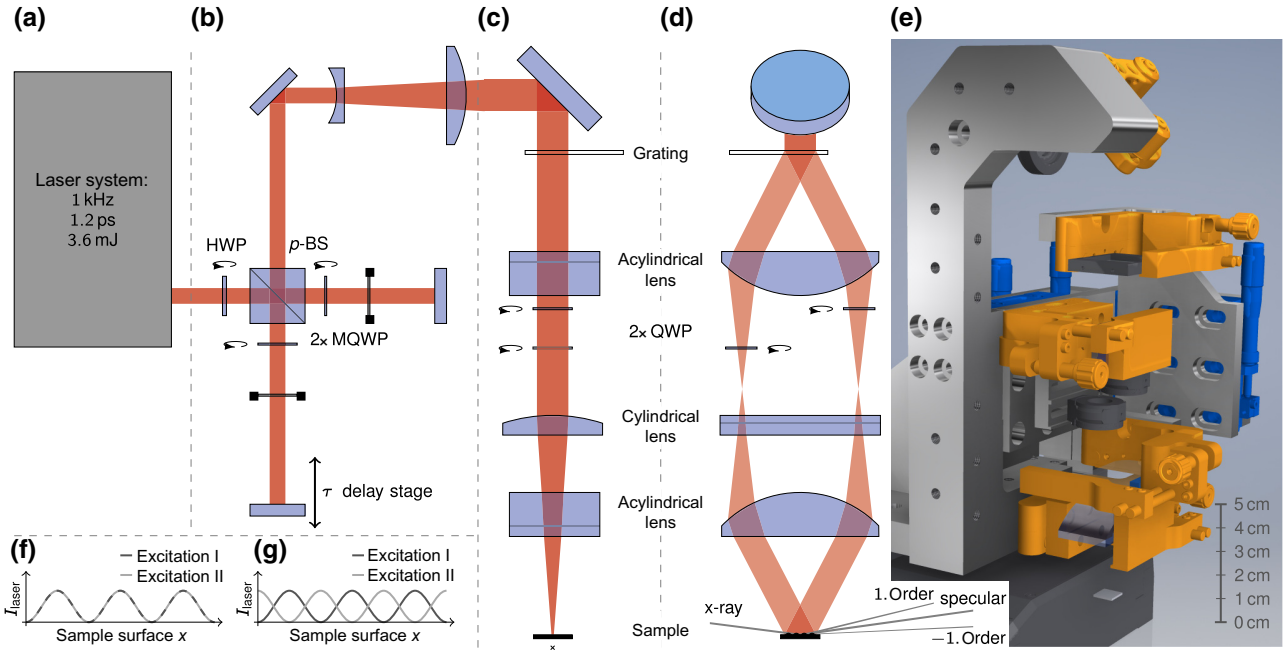

FIG. 2. Optical setup. (a) The output of a 1-kHz laser system is coupled to a Michelson interferometer (b), where *s*- and *p*-polarized replicas of the pump pulse are generated. (c) Side view of the TG setup. (d) Front view of the beam path of the +1st and −1st diffraction order. (e) Three-dimensional (3D) view of the TG setup with the optomechanical components. (f),(g) The created relative spatial phase of the interference grating for parallel and perpendicular setting of the QWPs.

interferometer includes a quarter-wave plate, which we refer to as Michelson-quarter-wave plates (MQWP) in Fig. 2b. Due to the double passage of the beams, the MQWP effectively rotates the linear polarization by 90°. Thus, the output of the interferometer yields one *s*- and one *p*-polarized optical pump pulse. The pulses have a variable relative time delay τ that is defined by the difference of the path lengths of the Michelson interferometer arms. Both pulses are subsequently coupled into the TG setup, where they essentially are diffracted into ±1st-order beams by the phase mask. Zero-order and higher-order diffraction intensities are minimized by the specific design of the transmission phase mask.

In addition to simple TG excitation, our setup allows for selecting the spatial phase of the TG to perform spatiotemporal coherent control. We use the fact that the spatial phase of the TG at the sample surface depends on the relative temporal phase of the interfering optical beams. For example, interference gratings generated by two optical beams of either parallel or antiparallel polarization have an opposite spatial phase with respect to each other [35]. Note that, in the antiparallel case, the electric fields of +1st- and −1st-order beams have a relative temporal phase of π, i.e., exactly the same value as the relative spatial phase shift of the generated TG. As explained below, we employ quarter-wave plates (QWP) and different polarizations to impose a relative spatial phase shift between two consecutive TG excitations.

After collimation by the first acylindrical lens, each beam propagates through a QWP. The QWPs are oriented either with the fast or slow axis aligned with the polarization of the laser pulses. If the QWPs have identical orientation, there is no relative temporal phase offset between the ±1st-order beams as they both traverse the QWPs at either the fast or the slow axis. Note that both consecutive *s*- and *p*-polarized laser pulses generate TGs with an identical spatial phase, i.e., $\varphi_x = 0$. Hence, with a parallel setting of the QWPs, one can generate cases A and C, discussed in Sec. II.

If the QWPs are oriented perpendicular to each other, the +1st- and −1st-order beams experience a relative temporal phase shift of $\pm\pi/2$, which directly translates into a spatial phase offset of $\pm\pi/2$ of the TG excitations. The opposite sign of the temporal phase shift holds for the *s*- and *p*-polarized beams, respectively. The magnitude of the spatial phase difference between the *s*- and *p*-polarized TG is therefore equal to π, i.e., $\varphi_x = \pi$. Hence, with a perpendicular setting of the QWPs, one readily obtains cases B and D, discussed in Sec. II, where the PSD due to the TTG is relieved by the second TG excitation.

The experimental results presented and discussed in the next section are obtained on a 30-nm-thick metallic $SrRuO_3$ (SRO) film epitaxially grown by pulsed laser deposition on a (110)-oriented $DyScO_3$ (DSO) substrate. The sample is excited with TG excitations, each having a spatial period $\Lambda = 2.4$ μm and an incident pump fluence

of 18 mJ/cm^2 for the central fringes of the TG [36]. We employ a commercial Ti:sapphire laser amplifier (Coherent Legend Elite), which delivers 800-nm pulses with a duration of 1.2 ps and a pulse energy of 3.6 mJ. The laser repetition rate is 1 kHz, synchronized to the synchrotron. The shortest grating period Λ inscribed in the sample is ultimately limited by the laser wavelength. By frequency doubling or tripling of the fundamental frequency, one can reduce the period to less than 300 nm. The generation of transient gratings with periods less than 100 nm has been demonstrated by using high-energy radiation from free-electron laser sources [37,38]. Thus, our method can be employed truly on nanometer length scales.

Monochromatized 15-keV x-ray probe pulses are selected from the synchrotron pulse train by a high-speed chopper at the same frequency. The pump-probe delay can be changed electronically by the laser synchronization unit. In the experiment presented here, the total temporal resolution is limited to 75 ps, mainly due to the duration of the x-ray probe pulses. In principle, the experimental time resolution is also limited by the rather large wavefront tilt between the exciting laser and probing x-ray pulses; however, in the present case, this is only a minor limitation (approximately 10 ps). Diffracted x-ray photons are captured on an area detector (Rayonics MX170-HS) [39,40]. For the evaluation, the intensity $I_{-1\mathrm{st}}$ of the -1st diffraction order is integrated in a region of interest on the area detector. The recorded intensity is normalized to a static diffraction background I_n to reduce influences of beam instabilities and thermal drifts of the sample and setup. In order to extract the surface modulation amplitude Δu, we take the square root of the diffracted intensity after subtracting a scattering background I_{bg} by averaging all unpumped detected intensities of the -1st diffraction order. This results in

$$\Delta u \propto \sqrt{\left|\frac{I_{-1\mathrm{st}} - I_{\mathrm{bg}}}{I_n}\right|}\,\mathrm{sgn}\left(I_{-1\mathrm{st}} - I_{\mathrm{bg}}\right), \tag{2}$$

where the absolute function circumvents imaginary results and the sgn function projects these values on the negative axis for the surface modulation amplitude Δu.

IV. RESULTS AND DISCUSSION

First, we briefly discuss the transient response of the sample surface to a single TG excitation. As derived in earlier studies [15], the surface modulation amplitude Δu is proportional to the square root of the diffracted intensity. The transient amplitude of the laser-generated PSD inferred from the the x-ray intensity diffracted into -1st-order is shown by the blue bullets in Fig. 3(a). It features a steplike rise followed by oscillations on top of a slowly decaying thermal offset. The surface excursion field can

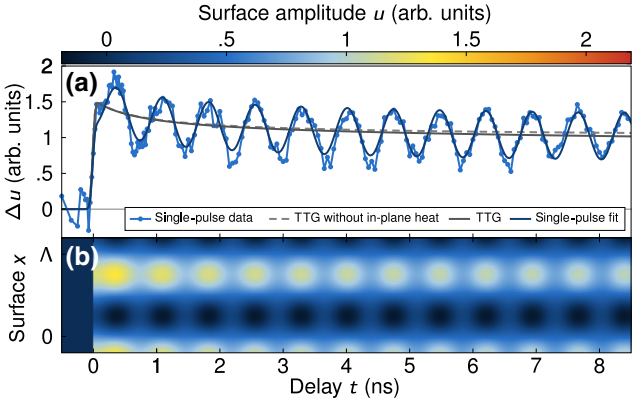

FIG. 3. Single-pulse excitation. (a) Time-dependent surface modulation amplitude $\Delta u(t)$ measured with TRXRR. The data (blue bullets) are modeled by calculating the spatiotemporal surface deformation field $u(x,t)$ [cf. Eq. (3)]. The dark blue solid line shows the time dependence of the Fourier component $(\mathcal{F}u)(q_\parallel,t)$ at the characteristic wave vector $q_\parallel$. The surface modulation amplitude of only the thermal distortion $(\mathcal{F}u_{\mathrm{th}})(q_\parallel,t)$ due to the TTG is shown by the gray lines with (solid) and without (dashed) in-plane heat diffusion. (b) Illustration of the spatiotemporal surface deformation field $u(x,t)$ calculated using Eq. (3).

thus be precisely modeled by

$$u = \Theta(t)\Big[u_{\mathrm{th}}(x,t,\varphi_x) + u_{\mathrm{SAW}}(x,t,\varphi_x,\varphi_t)\Big], \tag{3}$$

where u_{th} is the slowly decaying amplitude of the TTG and u_{SAW} is the amplitude of the coherent surface acoustic mode, defined as

$$u_{\mathrm{th}} = \frac{u_{\mathrm{th},0}(t)}{2}\, e^{-\alpha_x q_\parallel^2 t}\left[1 + \sin\left(q_\parallel x - \varphi_x\right)\right], \tag{4}$$

$$u_{\mathrm{SAW}} = -\frac{u_{\mathrm{SAW},0}}{2}\,\sin\left(q_\parallel x - \varphi_x\right)\cos(\omega t - \varphi_t). \tag{5}$$

The rise time τ_{rise} of the TTG is dictated by the ratio of the thickness (or the optical penetration depth if the latter is much shorter) and sound velocity of the laser-excited film. Typical time scales of thin-film expansion are a few tens of picoseconds or even down to a few picoseconds for very thin films [41]. In the present case, τ_{rise} is much shorter than all other involved dynamics and thus approximated by the Heaviside function $\Theta(t)$ in Eq. (3). In fact, τ_{rise} defines the fundamental limit for coherent control of the TTG (cases B and D), which can thus be truly applied down to picosecond time scales as demonstrated in Sander *et al.* [15]. The concept of spatiotemporal coherent control is generally applicable to an arbitrary number of coherent modes [14,15,42], but in the present case the data only exhibit a single Rayleigh-like SAW mode. We can thus restrict our model to only include this single coherent mode. Note that the first TG

excitation always defines the zero phase φ_x and φ_t, respectively. In order to mimic the sensitivity of the x-ray probe beam to only the modulation of the PSD, we extract the transient wave-vector-dependent surface modulation amplitude $\Delta u(q,t) = (\mathcal{F}u)(q,t)$ by Fourier transformation of the spatiotemporal surface deformation field $u(x,t)$ depicted in Fig. 3(b). We then evaluate the surface modulation amplitude $\Delta u(q_\parallel, t)$ at the characteristic wave vector $q_\parallel$. The dark blue solid line in Fig. 3(a) shows the temporal behavior convoluted with the experimental temporal resolution of 75 ps.

The slowly decaying signal shown in Fig. 3(a) is caused by the PSD associated with the TTG that slowly decays due to thermal diffusion. This decay clearly exhibits a fast component decaying within the first 2 ns and a much slower component. The latter is due to in-plane thermal diffusion between hot and cold areas of the TTG. An analytical solution of the in-plane thermal diffusion for a sinusoidal thermal grating yields the exponential term in Eq. (4), which implies a decay time of $(\alpha_x q_\parallel^2)^{-1} =$ 210 ns [43,44]. Here, the homogeneous in-plane diffusivity $\alpha_x = 0.8$ mm^2/s is used for a substrate temperature of 323 K [45]. The initial fast decay originates from different thermal expansion coefficients of the metallic SRO film and the insulating DSO substrate. In fact, SRO expands stronger upon heating than DSO [46,47]. Thus, as heat diffuses along the out-of-plane direction from the excited areas in the SRO film into the substrate, the total surface excursion is reduced. In order to verify this, we model the out-of-plane heat transport by solving the one-dimensional heat diffusion equation with a finite-element method [48,49] by accounting for all relevant thermophysical properties of the materials. The experimental data are reproduced without including additional thermal resistance at the interface due to the nearly perfect acoustic impedance match between the involved materials and the high structural quality of the sample. The simulation yields the surface distortion $u_{\mathrm{th},0}(t)$ used as input for Eq. (4). The surface modulation amplitude due to combined out-of-plane and in-plane thermal diffusion is shown as a gray solid line in Fig. 3(a). If in-plane thermal diffusion is neglected ($\alpha_x = 0$), the grey dashed line is obtained, which proves that the initial fast decay is indeed governed by the out-of-plane thermal transport. The very good agreement between experiment and calculation evidences that the presented method can be a powerful tool to investigate multidirectional thermal transport in nanoscopic heterostructures. We do not observe deviations from linear behavior of our sample even up to very large excitation densities [50]. This aspect is particularly important for the multipulse excitation discussed in the next paragraph.

With the well-calibrated single-pulse excitation, we finally demonstrate full spatiotemporal control of transient and quasistatic PSDs via double-pulse TG excitation. By employing two consecutive TG excitations, we set the spatiotemporal phase of the excitation to the four different cases introduced in Sec. II. The corresponding dynamic surface excursion measured by TRXRR for these four cases is shown in Figs. 4(a)–4(d), respectively. As predicted above, the spatial phase setting $\varphi_x = 0$, selected by a parallel alignment of the QWPs in the optical setup, results in an increase of the PSD (cases A and C) due to an enhancement of the TTG. In contrast, the 90° rotation of only one QWP suppresses the PSD and relieves the TTG completely (cases B and D). The phase of the SAW is controlled by both the spatial and temporal phase φ_x and φ_t, respectively. For any setting of the spatial phase, one can either suppress (cases C and B) or enhance (cases A and D) the SAW mode by choosing the correct time delay τ of the second TG excitation. Note, in particular, the comparison of cases A and B, where $\tau = 0.73$ ns is identical. Still, not only the timing τ alone determines the amplitude of the SAW after the second excitation, as explained in Sec. II.

The possibility of suppressing the coherent mode (cases B and C) offers a precise tool for investigations of the multidirectional thermal transport in nanoscale heterostructures without undesired coherent signals yet ensuring sufficient time resolution given by the ultrashort laser and x-ray pulses. In case C, we clearly observe the multicomponent relaxation due to in-plane and out-of-plane heat diffusion, which is discussed above for single-pulse excitation. However, here, the signal of thermal origin is not masked by the coherent signal. The finite decaying intensity after the second TG excitation in case B [Fig. 4(b)] evidences that the TTG is not immediately suppressed by the second excitation. This is caused by the partial decay of the first TTG between the two excitations due to fast out-of-plane heat diffusion, which results in the observed imbalance of both TTGs. All observations are accurately reproduced by our modeling introduced above. Altogether, the sensitivity to thermal transport in layered heterostructures can be greatly enhanced with spatiotemporal coherent control using TG excitations.

A qualitative difference from the other recorded signals is observed in case D shown in Fig. 4(d), where the TTG is suppressed and the SAW is enhanced. Here, we observe a coherent oscillation exhibiting twice the frequency of the excited SAW. Recall that the data represent the variations of the 1st-order diffracted x-ray intensity. If a true second harmonic of the fundamental SAW is present, Eq. (1) implies that the corresponding 1st order of the second harmonic would be diffracted toward larger angles. In other words, the 1st-order diffraction angle cannot contain signatures of a second harmonic SAW. Again, we model the transient diffracted x-ray intensity caused by the spatiotemporal sample surface dynamics in analogy to the single-pulse excitation data analysis [cf. Eqs. (3)–(5)]. Note that our model is a purely linear response

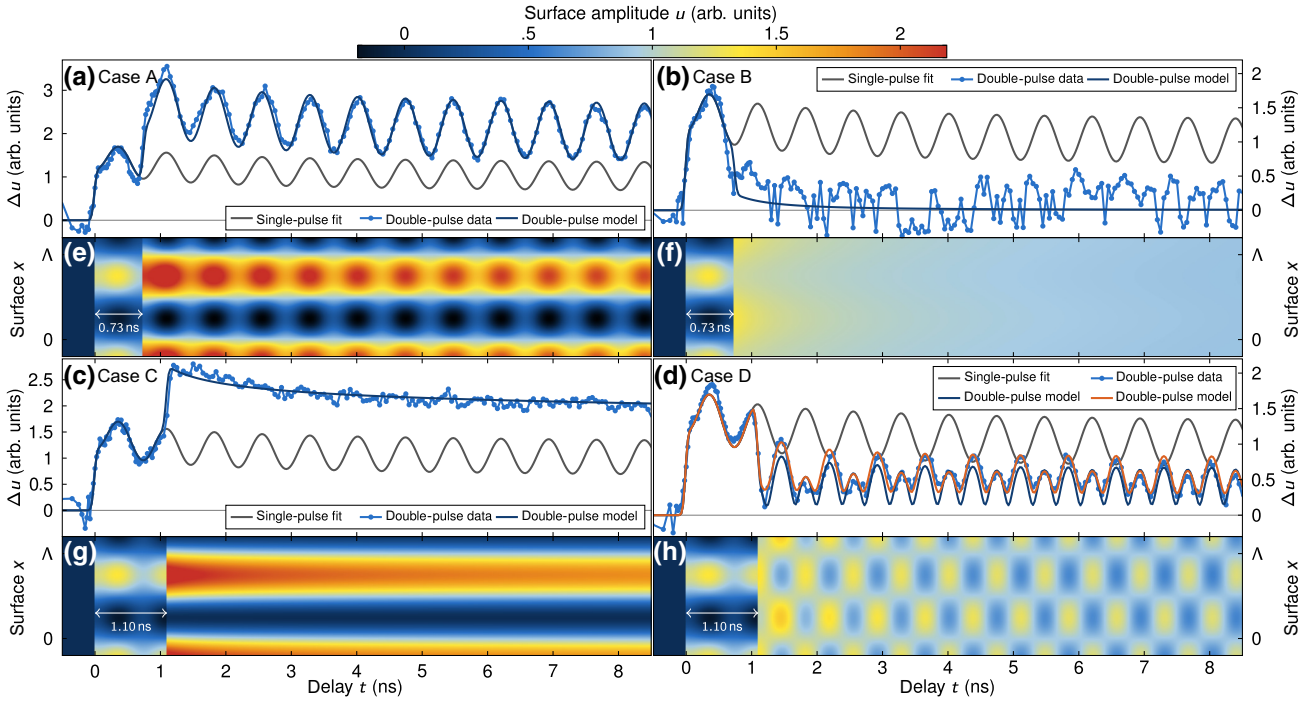

FIG. 4. Double-pulse excitation: (a),(e) case A; (b),(f) case B; (c),(g) case C; (d),(h) case D. The single-pulse responses as modeled in Fig. 3 are shown in gray for comparison in (a)–(d). Symbols show the TRXRR measurements and dark blue solid lines show the transient surface modulation amplitude $\Delta u(q_\parallel, t)$ for the characteristic wave vector $q_\parallel$ of the spatiotemporal surface deformation field shown in (e)–(h) derived from Eq. (3). All calculated traces are convoluted with a 75-ps Gaussian to match the temporal resolution of the experiment. The orange line in (d) represents the best fit to the double-pulse data by allowing for an amplitude and phase variation of the second excitation pulses.

model and thus does not support higher harmonics of the employed modes. Assuming the time delay τ chosen in the experiment and two identical TG excitations, we obtain the dark blue curve in Fig. 4(d). Obviously, our modeling correctly yields the doubled frequency. As indicated above, this is due to the detection process, which measures different oscillation frequencies from the same acoustic mode with and without the additional TTG that acts as a spatial local oscillator. Note that the amplitudes of the even and odd oscillation maxima are different, which can be traced back to the heat diffusion dynamics of the first TTG between the two TG excitations breaking the symmetry. As case B reveals, the two TTGs converge in amplitude after a few nanoseconds. In case D (dark blue line), this is manifested in the equilibration of the even and odd oscillation maxima on the same time scale. However, this equilibration of oscillation amplitudes is not fully featured in the experimental data, which indicates an asymmetry in the TG excitation strengths. Also, the level around which the signal oscillates is larger. Indeed, the data are accurately reproduced [orange line in Fig. 4(d)] if we assume a 9% larger amplitude and a slight detuning of the spatial phase of 3% for the second excitation pulse. Such errors may stem from slight deviations from optimal laser beam and QWP alignments.

V. STRAIN CONTROL IN FUNCTIONAL MATERIALS

In the following paragraph, we outline possible interaction channels between the excited deformation and functional properties of the crystal. In particular, we describe strain-induced changes of the free energy density via magnetoelastic effects and changes of the electronic band energy via deformation potential coupling. Finally, we briefly introduce active optical elements that use dynamic strain fields to manipulate x-ray pulses emitted by synchrotron storage rings.

If strain is used as a functional tool, it is important to recall that the interaction of lattice deformations with a material strongly depends on the symmetry, i.e., on the specific component of the strain tensor ε. The strain fields corresponding to TTG and coherent Rayleigh-like SAWs are composed of both compressive or tensile (e.g., ε_{xx}, ε_{zz}) and shear (e.g., ε_{xz}) components. The TRXRR method detects the absolute surface deformation, i.e., the integrated out-of-plane expansion of the excited volume. However, knowing one component of the strain tensor of a Rayleigh wave allows us to infer all the other components as well [51]. In our coherent control scheme, all strain components of the coherent mode are customizable as well as

the in-plane and shear components of the TTG. Only the out-of-plane component of the thermal grating is given by the initially absorbed energy density profile.

In multiferroic materials, a dynamic strain wave modifies the free energy density due to elastic deformations of the lattice. As an example, we discuss ferromagnetic materials, where the magnetoelastic interaction modulates the free magnetic energy density f_{mag} [52]. In a static case, f_{mag} is composed of the Zeeman energy, which depends on an external magnetic field, and of static anisotropy components such as magnetocrystalline, shape, and magnetoelastic anisotropy [53]. The interplay of these terms results in a direction and magnitude of the macroscopic magnetization $\vec{M}$. Their dynamics can be induced through time-dependent changes of free magnetic energy f_{mag}. Prominent examples are ferromagnetic resonance (FMR) measurements [54], which act on the Zeeman energy or all-optical switching [55], where laser-induced heating leads to changes of the shape anisotropy. In complete analogy, an acoustic wave dynamically changes f_{mag} via the magnetoelastic energy term [52].

Although magnetoelastic interaction is well known, magnetoacoustics has only been investigated quite recently [8,56,57]. Since then, strain-induced magentization dynamics of nanoparticles excited specifically by Rayleigh waves has gained strong interest [58,59]. These efforts are driven by the potential of strain-induced dynamics, i.e., energy efficiency, mode selectivity, and the ability to tailor the excitation to nanosize dimensions. Several of these recent experiments use optical generation of strain waves, thus pushing magnetoelastic excitations to picosecond time scales [34,42,60]. The strain control scheme described in this article not only allows us to selectively excite magnetization dynamics, but also enables control of these excitations on picosecond time scales. In particular, this is not only limited to the coherent strain but rather extends to thermal strain, while maintaining the high temporal resolution.

The second interaction channel we discuss is the deformation potential coupling of electrons with acoustic phonons. The deformation of the crystal lattice by an acoustic lattice distortion leads to an energy shift $\Delta E = a\varepsilon$ of the extremal points of the electron bands, where a is the deformation potential, which typically has a value of about 10 eV at the Γ point of tetrahedral semiconductors such as Si or GaAs [61]. Hence, already a small dynamic strain of the order of 10^{-3} up to 10^{-2} leads to changes of the conduction and valence bands of 10–100 meV. Strain-induced changes of the electronic structure affect charge transport and optical properties [62,63] and provide control of recombination dynamics in nanostructures [6,64]. Strain control of optical properties of nanostructures is a promising candidate for applications in quantum computation and quantum information technology [65,66]. The realization of such applications depends on the ability to control the lattice strain, ideally on short to ultrashort time scales. While the two examples given above may require probing mechanisms other than TRXRR (e.g., magneto-optical probing, optical and/or x-ray dichroism, or valence spectroscopies), the method presented in this paper may pave the way for these future applications.

Finally, we discuss a specific application developed by our group, where strain-induced deformations are used to realize active ultrafast x-ray optics. The devices are optimized for installation at synchrotron beamlines. A prominent example is the picosecond Bragg switch (PicoSwitch), which shortens an incident synchrotron x-ray pulse to a duration of a few picoseconds [67]. The coherent control of TTGs similar to case B (cf. Sec. II) allows for controlling diffraction of an incident x-ray pulse into the $\pm$1st diffraction order of the TTG. In particular, our approach allows us to turn the diffraction on and off on sub-nanosecond time scales. Thus, TTGs could be employed to pick individual x-ray pulses from a synchrotron pulse train for subsequent pump-probe experiments. Furthermore, the device may also be employed as a variable beam splitter in order to, e.g., distribute x-ray pulses among multiple beamlines. This may be particularly interesting at x-ray free-electron laser (XFEL) facilities, where currently only one experimental station is operational at a time. With such an approach, several instruments could be supplied with XFEL pulses in parallel. The main challenge for this device is to achieve high diffraction efficiencies. Our previous studies suggest that a maximum efficiency of more than 30% could be reached [14,15,68].

VI. CONCLUSION

In conclusion, we demonstrate spatiotemporal control of acoustic and thermal deformations of solid surfaces. The optical setup allows for generation of transient surface gratings with a variable spatial phase. Hence, a thermal deformation can either be enhanced or suppressed by a temporal sequence of excitation pulses on time scales much shorter than the deformation lifetime. In addition, we show that the suppression of the coherent signal facilitates investigations of multidirectional thermal transport in nanolayered heterostructures with high time resolution. We believe that our method presents an important step toward developing strain as a functional tool for solids and nanostructures. As examples, we discuss the magnetoelastic interaction in ferromagnetic materials. While numerous recent studies have demonstrated the ability to manipulate the macroscopic magnetization with coherent strain pulses, our present scheme paves the way for controlled strain-induced preparation of a ferromagnetic state. Strain control may also be applied to manipulate electronic states in bulk and low-dimensional semiconductors. Finally, we discuss active optical elements, which are a new kind of

strain-based device for ultrafast x-ray beam manipulation at synchrotrons.

ACKNOWLEDGMENTS

The TRXRR experiments are performed at the beamline ID09 of the European Synchrotron Radiation Facility (ESRF), Grenoble, France. We are grateful to Michael Wulff and Norman Kretzschmar for providing assistance in using beamline ID09. We also gratefully acknowledge the technical support of Christine Fischer and Elko Hannemann. Finally, we thank Jutta Schwarzkopf from the Leibniz-Institut für Kristallzüchtung, Berlin, for providing the sample. We acknowledge the Deutsche Forschungsgemeinschaft for the financial support via Grant No. BA2281/8-1 and funding from the BMBF via Grant No. FK05K16GU3.

[1] C. Thomsen, H. T. Grahn, H. J. Maris, and J. Tauc, Surface generation and detection of phonons by picosecond light pulses, Phys. Rev. B **34**, 4129 (1986).

[2] P. Ruello and V. E. Gusev, Physical mechanisms of coherent acoustic phonons generation by ultrafast laser action, Ultrasonics **56**, 21 (2015).

[3] R. Shayduk, M. Herzog, A. Bojahr, D. Schick, P. Gaal, W. Leitenberger, H. Navirian, M. Sander, J. Goldshteyn, I. Vrejoiu, and M. Bargheer, Direct time-domain sampling of subterahertz coherent acoustic phonon spectra in $SrTiO_3$ using ultrafast x-ray diffraction, Phys. Rev. B **87**, 184301 (2013).

[4] A. Bojahr, M. Gohlke, W. Leitenberger, J. Pudell, M. Reinhardt, A. von Reppert, M. Roessle, M. Sander, P. Gaal, and M. Bargheer, Second Harmonic Generation of Nanoscale Phonon Wave Packets, Phys. Rev. Lett. **115**, 195502 (2015).

[5] D. J. Singh, Q. Xu, and K. P. Ong, Strain effects on the band gap and optical properties of perovskite $SrSnO_3$ and $BaSnO_3$, Appl. Phys. Lett. **104**, 011910 (2014).

[6] M. Weiß, J. B. Kinzel, F. J. R. Schülein, M. Heigl, D. Rudolph, S. Morkötter, M. Döblinger, M. Bichler, G. Abstreiter, J. J. Finley, G. Koblmüller, A. Wixforth, and H. J. Krenner, Dynamic acoustic control of individual optically active quantum dot-like emission centers in heterostructure nanowires, Nano Lett. **14**, 2256 (2014).

[7] A. V. Scherbakov, A. S. Salasyuk, A. V. Akimov, X. Liu, M. Bombeck, C. Brüggemann, D. R. Yakovlev, V. F. Sapega, J. K. Furdyna, and M. Bayer, Coherent Magnetization Precession in Ferromagnetic (Ga,Mn)As Induced by Picosecond Acoustic Pulses, Phys. Rev. Lett. **105**, 117204 (2010).

[8] J.-W. Kim, M. Vomir, and J.-Y. Bigot, Ultrafast Magnetoacoustics in Nickel Films, Phys. Rev. Lett. **109**, 166601 (2012).

[9] R. Blattmann, H. J. Krenner, S. Kohler, and P. Hänggi, Entanglement creation in a quantum-dot–nanocavity system by fourier-synthesized acoustic pulses, Phys. Rev. A **89**, 012327 (2014).

[10] K. A. Nelson, R. J. D. Miller, D. R. Lutz, and M. D. Fayer, Optical generation of tunable ultrasonic waves, J. Appl. Phys. **53**, 1144 (1982).

[11] C. Klieber, E. Peronne, K. Katayama, J. Choi, M. Yamaguchi, T. Pezeril, and K. A. Nelson, Narrow-band acoustic attenuation measurements in vitreous silica at frequencies between 20 and 40 GHz, Appl. Phys. Lett. **98**, 211908 (2011).

[12] M. Herzog, A. Bojahr, J. Goldshteyn, W. Leitenberger, I. Vrejoiu, D. Khakhulin, M. Wulff, R. Shayduk, P. Gaal, and M. Bargheer, Detecting optically synthesized quasi-monochromatic sub-terahertz phonon wavepackets by ultrafast x-ray diffraction, Appl. Phys. Lett. **100**, 094101 (2012).

[13] F. J. R. Schülein, E. Zallo, P. Atkinson, O. G. Schmidt, R. Trotta, A. Rastelli, A. Wixforth, and H. J. Krenner, Fourier synthesis of radiofrequency nanomechanical pulses with different shapes, Nat. Nanotechnol. **10**, 512 EP (2015).

[14] M. Sander, M. Herzog, J. E. Pudell, M. Bargheer, N. Weinkauf, M. Pedersen, G. Newby, J. Sellmann, J. Schwarzkopf, V. Besse, V. V. Temnov, and P. Gaal, Spatiotemporal Coherent Control of Thermal Excitations in Solids, Phys. Rev. Lett. **119**, 075901 (2017).

[15] M. Sander, J.-E. Pudell, M. Herzog, M. Bargheer, R. Bauer, V. Besse, V. Temnov, and P. Gaal, Quantitative disentanglement of coherent and incoherent laser-induced surface deformations by time-resolved x-ray reflectivity, Appl. Phys. Lett. **111**, 261903 (2017).

[16] M. Bargheer, N. Zhavoronkov, Y. Gritsai, J. C. Woo, D. S. Kim, M. Woerner, and T. Elsaesser, Coherent atomic motions in a nanostructure studied by femtosecond x-ray diffraction, Science **306**, 1771 (2004).

[17] A. M. Lindenberg, I. Kang, S. L. Johnson, R. W. Falcone, P. A. Heimann, Z. Chang, R. W. Lee, and J. S. Wark, Coherent control of phonons probed by time-resolved x-ray diffraction, Opt. Lett. **27**, 869 (2002).

[18] O. Synnergren, T. N. Hansen, S. Canton, H. Enquist, P. Sondhauss, A. Srivastava, and J. Larsson, Coherent phonon control, Appl. Phys. Lett. **90**, 171929 (2007).

[19] P. Beaud, S. L. Johnson, A. Streun, R. Abela, D. Abramsohn, D. Grolimund, F. Krasniqi, T. Schmidt, V. Schlott, and G. Ingold, Spatiotemporal Stability of a Femtosecond Hard–X-ray Undulator Source Studied by Control of Coherent Optical Phonons, Phys. Rev. Lett. **99**, 174801 (2007).

[20] Y.-H. Cheng, F. Y. Gao, S. W. Teitelbaum, and K. A. Nelson, Coherent control of optical phonons in bismuth, Phys. Rev. B **96**, 134302 (2017).

[21] Q. Zhang, A. V. Nurmikko, A. Anguelouch, G. Xiao, and A. Gupta, Coherent Magnetization Rotation and Phase Control by Ultrashort Optical Pulses in CrO_2 Thin Films, Phys. Rev. Lett. **89**, 177402 (2002).

[22] T. Kampfrath, A. Sell, G. Klatt, A. Pashkin, S. Mährlein, T. Dekorsy, M. Wolf, M. Fiebig, A. Leitenstorfer, and R. Huber, Coherent terahertz control of antiferromagnetic spin waves, Nat. Photonics **5**, 31 (2010).

[23] J. Nishitani, T. Nagashima, and M. Hangyo, Terahertz radiation from antiferromagnetic MnO excited by optical laser pulses, Appl. Phys. Lett. **103**, 081907 (2013).

[24] D. W. Ward, J. D. Beers, T. Feurer, E. R. Statz, N. S. Stoyanov, and K. A. Nelson, Coherent control of

phonon-polaritons in a terahertz resonator fabricated with femtosecond laser machining, Opt. Lett. **29**, 2671 (2004).

[25] D. H. Hurley, R. Lewis, O. B. Wright, and O. Matsuda, Coherent control of gigahertz surface acoustic and bulk phonons using ultrafast optical pulses, Appl. Phys. Lett. **93**, 113101 (2008).

[26] Q. Li, K. Hoogeboom-Pot, D. Nardi, M. M. Murnane, H. C. Kapteyn, M. E. Siemens, E. H. Anderson, O. Hellwig, E. Dobisz, B. Gurney, R. Yang, and K. A. Nelson, Generation and control of ultrashort-wavelength two-dimensional surface acoustic waves at nanoscale interfaces, Phys. Rev. B **85**, 195431 (2012).

[27] H. F. Yang, F. Garcia-Sanchez, X. K. Hu, S. Sievers, T. Böhnert, J. D. Costa, M. Tarequzzaman, R. Ferreira, M. Bieler, and H. W. Schumacher, Excitation and coherent control of magnetization dynamics in magnetic tunnel junctions using acoustic pulses, Appl. Phys. Lett. **113**, 072403 (2018).

[28] M. Herzog, D. Schick, P. Gaal, R. Shayduk, C. V. Korff Schmising, M. Bargheer, Analysis of ultrafast X-ray diffraction data in a linear-chain model of the lattice dynamics, Appl. Phys. A **106**, 489 (2012).

[29] A. A. Maznev, A. Mazurenko, L. Zhuoyun, and M. Gostein, Laser-based surface acoustic wave spectrometer for industrial applications, Rev. Sci. Instrum. **74**, 667 (2003).

[30] A. Vega-Flick, J. K. Eliason, A. A. Maznev, A. Khanolkar, M. Abi Ghanem, N. Boechler, J. J. Alvarado-Gil, and K. A. Nelson, Laser-induced transient grating setup with continuously tunable period, Rev. Sci. Instrum. **86**, 123101 (2015).

[31] W. Sauer, M. Streibl, T. H. Metzger, A. G. C. Haubrich, S. Manus, A. Wixforth, J. Peisl, A. Mazuelas, J. Härtwig, and J. Baruchel, X-ray imaging and diffraction from surface phonons on GaAs, Appl. Phys. Lett. **75**, 1709 (1999).

[32] J.-D. Nicolas, T. Reusch, M. Osterhoff, M. Sprung, F. J. R. Schülein, H. J. Krenner, A. Wixforth, and T. Salditt, Time-resolved coherent x-ray diffraction imaging of surface acoustic waves, J. Appl. Crystallogr. **47**, 1596 (2014).

[33] M. Foerster, N. Statuto, B. Casals, A. Hernández-Mínguez, S. Finizio, A. Mandziak, L. Aballe, J. M. Hernàndez Ferràs, and F. Macià, Quantification of propagating and standing surface acoustic waves by stroboscopic x-ray photoemission electron microscopy, J. Synchrotron Radiat. **26**, 184 (2019).

[34] J. Janušonis, T. Jansma, C. L. Chang, Q. Liu, A. Gatilova, A. M. Lomonosov, V. Shalagatskyi, T. Pezeril, V. V. Temnov, and R. I. Tobey, Transient grating spectroscopy in magnetic thin films: Simultaneous detection of elastic and magnetic dynamics, Sci. Rep. **6**, 29143 (2016).

[35] F. Lagugné Labarthet, T. Buffeteau, and C. Sourisseau, Azopolymer holographic diffraction gratings: Time dependent analyses of the diffraction efficiency, birefringence, and surface modulation induced by two linearly polarized interfering beams, J. Phys. Chem. B **103**, 6690 (1999).

[36] The incident laser power per TG excitation is 970 mW at a 1-kHz repetition rate. The footprint of the noninterfering laser beams at the sample surface (elliptical Gaussian) is 4.0×3.4 mm^2 (major and minor $1/e$ diameter). Assuming a homogeneous distribution of the laser pulse energy over an ellipse, having the above size yields a pump fluence of 9 mJ/cm^2. Because of the interference of the crossing laser beams, the TG fringes at the center of the elliptical Gaussian have twice that fluence in the maximum.

[37] A. A. Maznev *et al.*, Generation of coherent phonons by coherent extreme ultraviolet radiation in a transient grating experiment, Appl. Phys. Lett. **113**, 221905 (2018).

[38] C. Svetina *et al.*, Towards x-ray transient grating spectroscopy, Opt. Lett. **44**, 574 (2019).

[39] M. Wulff, A. Plech, L. Eybert, R. Randler, F. Schotte, and P. Anfinrud, The realization of sub-nanosecond pump and probe experiments at the ESRF, Faraday Discuss. **122**, 13 (2003).

[40] M. Cammarata, L. Eybert, F. Ewald, W. Reichenbach, M. Wulff, P. Anfinrud, F. Schotte, A. Plech, Q. Kong, M. Lorenc, B. Lindenau, J. Räbiger, and S. Polachowski, Chopper system for time resolved experiments with synchrotron radiation, Rev. Sci. Instrum. **80**, 015101 (2009).

[41] D. Schick, M. Herzog, A. Bojahr, W. Leitenberger, A. Hertwig, R. Shayduk, and M. Bargheer, Ultrafast lattice response of photoexcited thin films studied by x-ray diffraction, Struct. Dyn. **1**, 064501 (2014).

[42] C. L. Chang, A. M. Lomonosov, J. Janusonis, V. S. Vlasov, V. V. Temnov, and R. I. Tobey, Parametric frequency mixing in a magnetoelastically driven linear ferromagnetic-resonance oscillator, Phys. Rev. B **95**, 060409(R) (2017).

[43] O. W. Käding, H. Skurk, A. A. Maznev, and E. Matthias, Transient thermal gratings at surfaces for thermal characterization of bulk materials and thin films, Appl. Phys. A **61**, 253 (1995).

[44] J. A. Johnson, A. A. Maznev, M. T. Bulsara, E. A. Fitzgerald, T. C. Harman, S. Calawa, C. J. Vineis, G. Turner, and K. A. Nelson, Phase-controlled, heterodyne laser-induced transient grating measurements of thermal transport properties in opaque material, J. Appl. Phys. **111**, 023503 (2012).

[45] J. Hidde, C. Guguschev, S. Ganschow, and D. Klimm, Thermal conductivity of rare-earth scandates in comparison to other oxidic substrate crystals, J. Alloys Compd. **738**, 415 (2018).

[46] S. Yamanaka, T. Maekawa, H. Muta, T. Matsuda, S.-I. Kobayashi, and K. Kurosaki, Thermophysical properties of SrHfO3 and SrRuO3, J. Solid State Chem. **177**, 3484 (2004).

[47] R. Uecker, B. Velickov, D. Klimm, R. Bertram, M. Bernhagen, M. Rabe, M. Albrecht, R. Fornari, and D. Schlom, Properties of rare-earth scandate single crystals (Re = Nd–Dy), J. Cryst. Growth **310**, 2649 (2008).

[48] R. Shayduk, H. Navirian, W. Leitenberger, J. Goldshteyn, I. Vrejoiu, M. Weinelt, P. Gaal, M. Herzog, C. V. K. Schmising, and M. Bargheer, Nanoscale heat transport studied by high-resolution time-resolved x-ray diffraction, New J. Phys. **13**, 093032 (2011).

[49] D. Schick, A. Bojahr, M. Herzog, R. Shayduk, C. von Korff Schmising, and M. Bargheer, udkm1Dsim – A simulation toolkit for 1D ultrafast dynamics in condensed matter, Comput. Phys. Commun. **185**, 651 (2014).

[50] M. Herzog, D. Schick, W. Leitenberger, R. Shayduk, R. M. van der Veen, C. J. Milne, S. L. Johnson, I. Vrejoiu, and M. Bargheer, Tailoring interference and nonlinear

manipulation of femtosecond x-rays, New J. Phys. **14**, 013004 (2012).

[51] P. Haas, Surface acoustic waves in materials science, Phys. Today **55**, 42 (2002).

[52] D. Sander, A. Enders, and J. Kirschner, Stress and magnetic properties of surfaces and ultrathin films, J. Magn. Magn. Mater. **200**, 439 (1999).

[53] R. C. O'Handley, *Modern magnetic materials: Principles and applications* (John Wiley, New York, 2000).

[54] M. Farle, Ferromagnetic resonance of ultrathin metallic layers, Rep. Prog. Phys. **61**, 755 (1998).

[55] A. Kirilyuk, A. V. Kimel, and T. Rasing, Ultrafast optical manipulation of magnetic order, Rev. Mod. Phys. **82**, 2731 (2010).

[56] M. Deb, E. Popova, M. Hehn, N. Keller, S. Mangin, and G. Malinowski, Picosecond acoustic-excitation-driven ultrafast magnetization dynamics in dielectric bi-substituted yttrium iron garnet, Phys. Rev. B **98**, 174407 (2018).

[57] S. P. Zeuschner, T. Parpiiev, T. Pezeril, A. Hillion, K. Dumesnil, A. Anane, J. Pudell, L. Willig, M. Rössle, M. Herzog, A. von Reppert, and M. Bargheer, Tracking picosecond strain pulses in heterostructures that exhibit giant magnetostriction, Struct. Dyn. **6**, 024302 (2019).

[58] Y. Yahagi, B. Harteneck, S. Cabrini, and H. Schmidt, Controlling nanomagnet magnetization dynamics via magnetoelastic coupling, Phys. Rev. B **90**, 140405(R) (2014).

[59] J. Tejada, E. M. Chudnovsky, R. Zarzuela, N. Statuto, J. C. de la Rosa, P. V. Santos, and A. Hernández-Mínguez, Switching of magnetic moments of nanoparticles by surface acoustic waves, Europhys. Lett. **118**, 37005 (2017).

[60] C. L. Chang, R. R. Tamming, T. J. Broomhall, J. Janusonis, P. W. Fry, R. I. Tobey, and T. J. Hayward, Selective Excitation of Localized Spin-Wave Modes by Optically Pumped Surface Acoustic Waves, Phys. Rev. Appl. **10**, 034068 (2018).

[61] A. Blacha, H. Presting, and M. Cardona, Deformation potentials of $k = 0$ states of tetrahedral semiconductors, Phys. Stat. Sol. (b) **126**, 11 (1984).

[62] Y. Wang, Y. Chen, H. Li, X. Li, H. Chen, H. Su, Y. Lin, Y. Xu, G. Song, and X. Feng, Buckling-based method for measuring the strain–photonic coupling effect of GaAs nanoribbons, ACS Nano **10**, 8199 (2016).

[63] O. D. D. Couto, Jr., S. Lazic, F. Iikawa, J. A. H. Stotz, U. Jahn, R. Hey, and P. V. Santos, Photon anti-bunching in acoustically pumped quantum dots, Nat. Photonics **3**, 645 EP (2009).

[64] M. M. de Lima and P. V. Santos, Modulation of photonic structures by surface acoustic waves, Rep. Prog. Phys. **68**, 1639 (2005).

[65] C. H. W. Barnes, J. M. Shilton, and A. M. Robinson, Quantum computation using electrons trapped by surface acoustic waves, Phys. Rev. B **62**, 8410 (2000).

[66] M. J. A. Schuetz, E. M. Kessler, G. Giedke, L. M. K. Vandersypen, M. D. Lukin, and J. I. Cirac, Universal Quantum Transducers Based on Surface Acoustic Waves, Phys. Rev. X **5**, 031031 (2015).

[67] M. Sander, R. Bauer, V. Kabanova, M. Levantino, M. Wulff, D. Pfuetzenreuter, J. Schwarzkopf, and P. Gaal, Demonstration of a picosecond Bragg switch for hard x-rays in a synchrotron-based pump–probe experiment, J. Synchrotron Radiat. **26**, 1253 (2019).

[68] S. Vadilonga, I. Zizak, D. Roshchupkin, A. Petsiuk, I. Dolbnya, K. Sawhney, and A. Erko, Pulse picker for synchrotron radiation driven by a surface acoustic wave, Opt. Lett. **42**, 1915 (2017).

JOURNAL OF SYNCHROTRON RADIATION

ISSN 1600-5775

Received 20 July 2020
Accepted 5 January 2021

Edited by S. M. Heald, Argonne National Laboratory, USA

Keywords: synchrotron; time-resolved; thermal deformation; transient grating; pulse picking.

A new concept for temporal gating of synchrotron X-ray pulses

D. Schmidt,[a] R. Bauer,[a] S. Chung,[b] D. Novikov,[b] M. Sander,[c] J.-E. Pudell,[d] M. Herzog,[d] D. Pfuetzenreuter,[e] J. Schwarzkopf,[e] R. Chernikov[f] and P. Gaal[e,a]*

[a]Institut für Nanostruktur- und Festkörperphysik, Universität Hamburg, Luruper Chaussee 149, 22761 Hamburg, Germany, [b]Deutsches Elektronen-Synchrotron (DESY), 22607 Hamburg, Germany, [c]Paul-Scherrer Institute, Forschungsstrasse 111, 5232 Villigen, Switzerland, [d]Institut für Physik und Astronomie, Universität Potsdam, 14476 Potsdam, Germany, [e]Leibniz-Institut für Kristallzüchtung, Max-Born-Strasse 2, 12489 Berlin, Germany, and [f]Canadian Light Source Inc., 44 Innovation Boulevard, Saskatoon, Canada SK S7N 2V3. *Correspondence e-mail: peter.gaal@ikz-berlin.de

A new concept for temporal gating of synchrotron X-ray pulses based on laser-induced thermal transient gratings is presented. First experimental tests of the concept yield a diffraction efficiency of 0.18%; however, the calculations indicate a theoretical efficiency and contrast of >30% and 10^{-5}, respectively. The full efficiency of the pulse picker has not been reached yet due to a long-range thermal deformation of the sample after absorption of the excitation laser. This method can be implemented in a broad spectral range (100 eV to 20 keV) and is only minimally invasive to an existing setup.

1. Introduction

Passive optical elements, for example monochromators, mirrors or lenses, are used in almost all synchrotron and free-electron laser (FEL) beamlines to tailor the properties of the emitted beam to the requirements of a specific experiment. Without these components the facilities could not host the broad range of science applications as they do today (Hand, 2009; Waldrop, 2014; Weckert, 2015). With the advent of high-power radiation sources adaptive optics are being developed to enable dynamic optimization of the beam conditions (Stoupin *et al.*, 2010; Quintana *et al.*, 1995; Berman & Hart, 1991; Yashchuk *et al.*, 2015; Goto *et al.*, 2015). Today most parameters of the emitted pulses can be tuned, for example energy and bandwidth, beam divergence, focal size or even the time structure of the emitted pulse itself (Schoenlein *et al.*, 2000; Sander *et al.*, 2019). The remaining parameter that can only be controlled with large effort is the time structure of the emitted pulse train. At most beamlines it is determined by the filling pattern of electron bunches in the storage ring. To accommodate all user needs, synchrotrons provide different bunch patterns over the year (Jankowiak & Wüstefeld, 2013; see also https://www.esrf.eu/Accelerators/Operation/Modes, https://photon-science.desy.de/facilities/petra_iii/machine/parameters/index_eng.html). In consequence, not all experiments available at a facility can be offered at the same time and some applications, in particular time-resolved experiments, constantly face an unfavorable time structure. In view of current upgrade programs to fourth-generation storage rings, this problem is expected to become even more pressing (Schroer *et al.*, 2018).

Few solutions exist that allow the time structure of the X-ray pulse pattern to be changed. The most reliable among them are mechanical choppers (LeGrand *et al.*, 1989; Wulff *et*

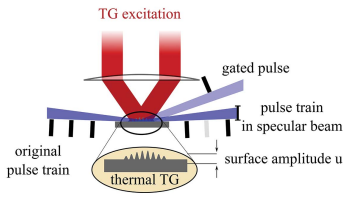

al., 2002; Gembicky & Coppens, 2007; Meents *et al.*, 2009; Kudo *et al.*, 2009; Ito *et al.*, 2009; Husheer *et al.*, 2012; Plogmaker *et al.*, 2012; Wang *et al.*, 2015; Förster *et al.*, 2015). Besides many technical challenges, their main disadvantage is the low flexibility of the devices which generally prevents a transfer to another setup. Other approaches employ rotating crystals (McPherson *et al.*, 2002) or piezoelectric crystals (Grigoriev *et al.*, 2006) to deflect individual X-ray bunches from the incident pulse train. Recently, this idea was successfully realized by oscillating micro-electromechanical structures (Mukhopadhyay *et al.*, 2015; Chen *et al.*, 2019). This method works only with monochromatic X-ray pulses and is generally limited to specific pre-selected pulse repetition rates. An undulator-based bunch kicker capable of isolating single bunches from a hybrid filling pattern was demonstrated at BESSY II (Holldack *et al.*, 2014). Finally, a promising concept relies on propagating surface acoustic waves (SAWs) which modulate the diffraction efficiency of a substrate Bragg peak (Roshchupkin *et al.*, 2003; Vadilonga *et al.*, 2017*a*). Due to the electronic control of the SAWs, this method provides the highest flexibility and is least invasive to an existing setup (Tucoulou *et al.*, 1997; Vadilonga *et al.*, 2017*b*). However, since it relies on Bragg diffraction from a crystalline substrate, it is limited to monochromatic hard X-rays.

In this work we present a new approach to control the time structure of an X-ray pulse train emitted by a synchrotron storage ring. Our method employs laser-induced thermal surface distortions with lateral periodicity. A grazing-incidence X-ray pulse is diffracted from the thermal transient grating (TG) away from the specular reflection and can be separated with an aperture or an analyzer crystal. The dynamics of the thermal grating can be controlled by the optical excitation (Pudell *et al.*, 2019), and temporal gating with opening times of 50 ps were demonstrated (Sander *et al.*, 2017*a*) with 1 ps optical pulses for the excitation of the TG. The theoretical limit of the diffraction efficiency is 33% (Sander *et al.*, 2017*b*). Realizing such high diffraction efficiency from the TG requires the generation of thermal surface gratings with amplitudes of few nanometres. Here we present surface height modulations from the thermal TG of several nanometres, which paves the way to application of thermal TGs for synchrotron pulse selection in a broad energy range of ∼100 eV to 20 keV. Since the diffraction does not rely on a Bragg peak, the method can tolerate a finite bandwith, for example a pink beam from an undulator.

In the next section, we briefly review diffraction of hard X-ray beams from laser-generated thermal TGs. In Section 3 we discuss the synchrotron pulse picking scheme in detail and present experimental data, which is discussed in Section 4. Current limitations of our approach and an outlook based on theoretical calculations are presented in Section 5.

2. X-ray diffraction from high-amplitude thermal transient gratings

Laser-generated thermal TGs consist of a periodic modulation of the sample surface height due to absorption of optical energy and subsequent thermal expansion. The lateral modulation of the optical intensity, which leads to the periodic expansion profile, is generated by interfering two laser pulses on the sample surface, as shown in Fig. 1(*a*). All-optical generation and probing of TGs is extensively discussed in the literature for thermal gratings and surface acoustic waves (Rogers *et al.*, 2000), phonon-polaritons (Goldshteyn *et al.*, 2014), magnetoacoustics (Janušonis *et al.*, 2016*a*,*b*) and coherent four-wave-mixing measurements (Knoester & Mukamel, 1991). Only recently thermal TGs were investigated by diffracting hard X-ray pulses under grazing-incidence geometry (Sander *et al.*, 2017*a*). Measurement of the transient surface excursion yields insights into the dynamics of coherent surface acoustic waves (Sander *et al.*, 2017*b*) and of the lateral and perpendicular thermal diffusion (Pudell *et al.*, 2019). The diffracted X-ray intensity in different diffraction orders is

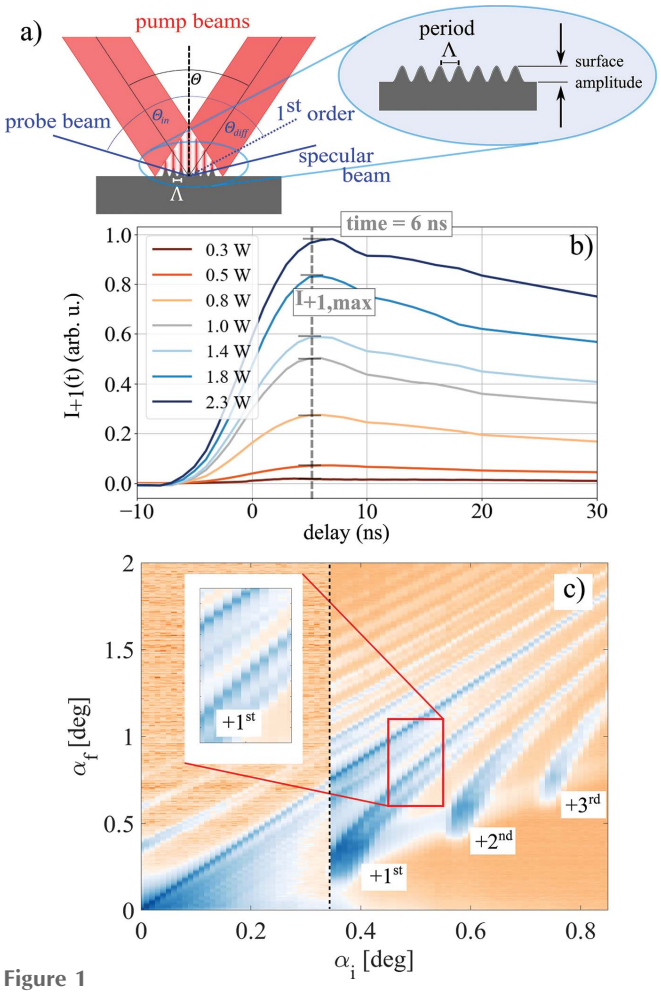

Figure 1
Experimental data. (*a*) Schematic of the optical generation and TRXRR probe of thermal TGs. (*b*) Measured first-order diffracted intensity from laser-generated thermal TGs. Measurements were performed at ID09 beamline at the European Synchrotron ESRF. The maximum of the diffracted intensity $I_{+1,\max}$ is reached at a delay of 6 ns (gray dashed line). (*c*) TRXXR measurement at a delay of 6 ns. The horizontal dashed line marks the concatenation of two measurements with different integration times of the detector. The measurement reveals multiple diffraction orders which are smeared out along α_f (*cf.* inset).

directly linked to the amplitude of the surface modulation. For the nth diffraction order, the intensity reads

$$I_n = \left| \frac{1}{r_0} \int_{r_\parallel} \exp\left\{ i\left[\frac{\Delta\varphi}{2} \sin(q_\parallel r_\parallel) - n\, q_\parallel r_\parallel \right] \right\} \mathrm{d}r \right|^2 = q \left| J_n\left(\frac{\Delta\varphi}{2}\right) \right|^2, \quad (1)$$

where J_n denotes the nth-order Bessel function of the first kind and $q_\parallel = 2\pi/\Lambda$ is the wavevector associated with the thermal TG. The phase term $\Delta\varphi$ is a function of X-ray wavelength λ_{Xray}, grating period Λ, incidence angle α_i and the surface amplitude u,

$$\Delta\varphi = -2\pi \frac{u}{\lambda_{\mathrm{Xray}}} \alpha_i \left[1 + \left(1 + \frac{2n\lambda_{\mathrm{Xray}}}{\Lambda \alpha_\mathrm{i}^2} \right)^{1/2} \right]. \quad (2)$$

We have discussed the limits of the diffraction model [*cf.* equations (1) and (2)] in a previous article (Sander *et al.*, 2017*b*). It is important to mention here that the maximum X-ray diffraction efficiency predicted by our model is 33% and that the necessary surface amplitude to reach this maximum value is a few nanometres.

Having connected the surface amplitude of the thermal TG to the diffracted intensity, one can now follow the amplitude decay over time due to thermal diffusion by time-resolved X-ray reflectivity (TRXRR) measurements. The analytical solution of the heat diffusion equation for a spatially periodic initial value problem allows for quick extraction of the lateral and perpendicular thermal conductivity from such measurements (Käding *et al.*, 1995). However, in this work we are interested in maximizing the diffracted X-ray intensity from a lateral thermal grating and do not retrieve thermal material properties from our measurements.

According to our diffraction model, maximizing the diffracted X-ray intensity requires high surface amplitudes of the thermal grating. However, energy absorption may lead to damage of the material if the sample temperature rises above the damage threshold. The peak temperature T_m generated by the excitation pulse can be estimated with the help of the diffusion parameter $\tau_\perp = a^2 c_\mathrm{p}\rho/2k$, where a, $c_\mathrm{p}\rho$ and k denote the optical penetration depth, volumetric specific heat and thermal conductivity, respectively. It is important to note that T_m is a function of the duration τ of the optical excitation pulse (Shayduk & Gaal, 2020). It can be approximated by

$$T_\mathrm{m}/T_\mathrm{s} = \frac{1}{(1+\tau/\tau_\perp)^{1/2}}, \quad (3)$$

where T_s is the peak temperature generated with an ultrashort optical pulse ($\tau \ll 100$ fs). A detailed derivation of equation (3) can be found elsewhere (Shayduk & Gaal, 2020). Our pulse picking scheme makes use of this effect: by employing an excitation pulse with a duration of 10 ns instead of only 1 ps we achieve a tenfold increase of the surface amplitude without inflicting any damage on our pulse picker sample.

Experimental data are shown in Fig. 1(*b*). The figure depicts the measured diffracted intensity in the +1st diffraction order I_{+1} over the pump–probe delay. To generate the TG in the sample we image a phase mask with $d = 4$ µm period on the sample surface with a magnification factor $M = 1/2$. Thus, the TG period was $\Lambda = d/2M = 4$ µm. The sample was a thin film heterostructure consisting of a top layer of optically transparent $LaAlO_3$ (LAO), an optically opaque layer of $La_{0.7}Sr_{0.3}MnO_3$ (LSMO) and a transparent $NdGaO_3$ (NGO) substrate. The layer thickness was 100 nm and 65 nm, respectively. We have studied similar samples with short excitation pulses (Bojahr *et al.*, 2015; Sander *et al.*, 2017*a*,*b*, 2019) and compared the effect of short- and long-pulse excitation directly (Shayduk & Gaal, 2020). With equation (3) we find a diffusion parameter $\tau_\perp \simeq 320$ ps. Due to the grazing-incidence angle of the X-ray probe pulse, the footprint of the pump and probe beams are larger than the sample surface, which makes it difficult to precisely determine the excitation fluence. We refrain from listing rough values for the excitation fluence and provide the laser output power as a measure for the excitation strength instead. We used a commercial amplified laser system (Coherent Legend) which delivers optical pulses at a wavelength of 800 nm, a repetition rate of 1 kHz and a pulse energy of 2 mJ. For the measurements shown in Fig. 1(*b*), we blocked the amplifier seed pulse to obtain a long pulse duration of 10 ns. The slow signal rise of the transients shown in Fig. 1(*b*) is evidence of the long excitation pulse. The diffracted intensity of all transients in Fig. 1(*b*) is normalized to the maximum value.

A time-resolved X-ray reflectivity (TRXRR) measurement at a pump–probe delay of 6 ns and a pump laser power of 2 W is depicted in Fig. 1(*c*). Due to strong diffuse scattering at grazing incidence angles, the data were recorded in two measurements with longer averaging at higher incidence angles. The concatenation of both measurements is marked by the horizontal black dashed line at an incidence angle of $\alpha_\mathrm{i} = 0.35°$. At the high surface amplitude of the transient grating we observe three positive diffraction orders and seven negative diffraction orders. Interestingly the diffracted intensity is smeared out along the exit angle α_f. We highlight this feature in the magnification of the red square, which shows a pronounced double structure of the specular beam and of the first diffraction order, respectively.

The data shown in Fig. 1 were measured at the ID09 beamline at the European Synchrotron ESRF. X-rays were delivered by the U17 undulator and monochromated to a relative bandwidth $\Delta E/E = 10^{-4}$ at an energy of 15 keV. A detailed discussion of the experimental setup can be found elsewhere (Shayduk & Gaal, 2020; Sander *et al.*, 2017*a*,*b*). Here, we want to point out that the X-ray beam diameter at the sample position was 20 µm, which results in a footprint of 20 µm × 5730 µm at grazing incidence angles of 0.2°. The elongation in the diffraction plane was larger than the sample with a surface area of 5 mm × 5 mm. Hence, an estimation of the diffraction efficiency from the grating was not possible. For that, we resort to the *in situ* and nanodiffraction beamline P23 at PETRA III, DESY. Experiments at this facility are

discussed in the next paragraph. In Section 4 we discuss the influence of the beam footprint and overlap with the excitation laser in detail and compare experimental data recorded at both facilities.

3. Synchrotron pulse picking using thermal transient gratings

In this section we demonstrate our new pulse picking approach by selecting a single X-ray pulse out of 255 consecutive synchrotron pulses. Our method is sketched in Fig. 2. X-ray pulses from a sychrotron storage ring impinge the sample at grazing incidence below the critical angle of total external reflection. Without TG excitation, the pulses are reflected in a specular beam. Upon inscribing a thermal TG, the X-ray pulse is diffracted into a higher order and can be separated by an aperture or by an analyzer crystal.

We have implemented this scheme at the *in situ* and nano-diffraction beamline P23 at PETRA III (DESY). The experimental setup is depicted in Fig. 3. Again we use an LAO/LSMO thin film heterostructure with thickness of 194 nm and 82 nm, respectively, grown on NGO substrate. The

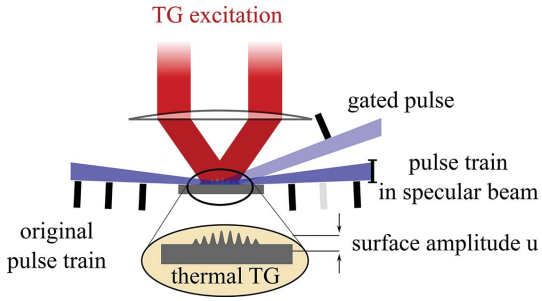

Figure 2
Pulse picking principle. X-ray pulses from the synchrotron impinge the NanoGate sample under grazing incidence and are diffracted away from the specular beam upon optical transient grating (TG) excitation. The main beam is blocked and only diffracted pulses are transferred to the sample.

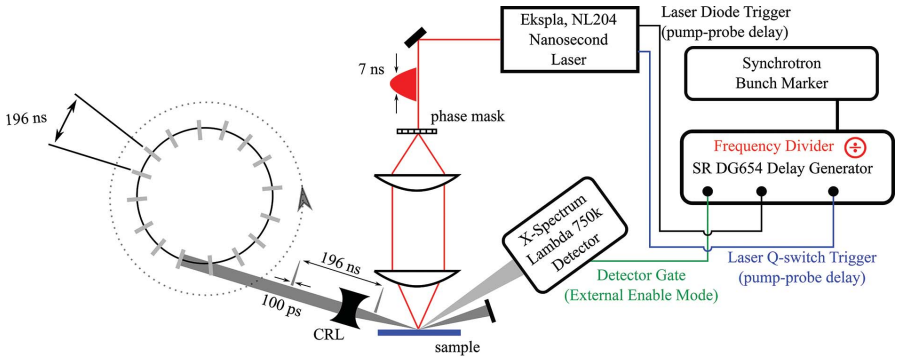

Figure 3
NanoGate layout. Experimental setup for NanoGate characterization measurements performed at P23 beamline at PETRA III, DESY. A Q-switched laser is synchronized to the PETRA III bunch clock and delivers optical excitation pulses with a duration of 7 ns to the TG setup (Pudell *et al.*, 2019) at a repetition rate of almost 1 kHz. The synchronization unit is also used to tune the pump–probe delay. The X-ray bunch spacing in 40 bunch mode is 196 ns and the X-ray pulse duration is 100 ps. Diffracted photons are detected by a hybrid pixel area detector in external gating mode (Pennicard *et al.*, 2013) (X-Spectrum LAMBDA 750k).

sample surface area was 10 mm × 10 mm to better shadow the direct beam at gracing incidence angles. Optical excitation pulses come from a Q-switched laser (Ekspla NL204) which delivers pulses with a duration ΔT = 7 ns at a wavelength of λ = 1064 nm and a pulse energy of 4 mJ. We use a delay generator (Stanford Research Systems DG645) which was synchronized to the synchrotron bunch marker to divide the bunch frequency to approximately 1 kHz and to generate trigger pulses for the laser and X-ray area detector. The pump–probe delay is implemented by scanning the laser diode and Q-switch trigger of the laser with 100 ps precision. Laser pulses are subsequently coupled into the TG setup which consists of a transmission phase mask and a system of lenses that images the phase mask onto the sample. The TG setup is discussed in detail elsewhere (Pudell *et al.*, 2019).

The P23 beamline delivers monochromatic X-ray pulses which can be focused to 1.6 µm × 200 µm (V × H) with a divergence of 0.5 mrad. In the horizontal direction the beam size was further reduced to 20 µm with a pair of slits. For our measurements the monochromator [Si(111) with $\Delta E/E$ = 10^{-4}] was tuned to an energy of 10.2 keV. The synchrotron was operated in 40 bunch mode, *i.e.* the temporal gap between two consecutive X-ray pulses is 196 ns. Again we use a phase mask with a d = 4 µm period which was now imaged with a magnification factor M = 1 onto the sample. Thus, the laser-generated thermal TG at the surface had a periodicity of Λ = 2 µm, *i.e.* only half the period of the ID09 measurement. In this configuration the incident beam is diffracted to higher angles which reduces the X-ray footprint on the sample and facilitates separation of the diffracted intensity from the specular reflection. The measured 1/e decay time for the transient grating was 52 ns, *i.e.* the TG is almost diffused within the bunch spacing dt = 196 ns. However, for shorter bunch spacing the thermal grating can be removed with a second TG excitation as described elsewhere (Pudell *et al.*, 2019). The specular reflection from the sample was blocked and photons diffracted into higher orders were captured with a hybrid pixel area detector (Pennicard *et al.*, 2013) with a pixel size of 55 µm × 55 µm (X-Spectrum, Lambda 750k). The detector was used in an external enable mode for electronic gating (Ejdrup *et al.*, 2009; Shayduk *et al.*, 2017). The electronic gate was set by the delay generator unit to values between 100 ns to 50 µs.

The sample was mounted on a 5+2 circle diffractometer in grazing incidence geometry. The detector distance to the sample was 1 m. The sample was exposed to a constant flow of room-temperature nitrogen gas for cooling, which had a noticeable effect on the stability and thermalization of the sample after exposure to the laser. The average laser power impinging the sample during the measurements was approximately 2 W.

4. Results and discussion

Test results of our pulse picking method are depicted in Fig. 4. Panel (*a*) shows diffracted intensity of a single X-ray pulse from the thermal transient grating on the area detector. The detector gate width was set to 140 ns, *i.e.* shorter than the interval between two X-ray pulses. The specular beam is blocked and the high-intensity areas stem from diffraction in the first and second order. The colorbar was chosen to saturate high intensities in order to pronounce the diffuse background. The incidence angle was set to 0.28° and the direct beam was completely shadowed by the sample. The specular reflex is blocked in Fig 4(*a*) to avoid saturation of the detector.

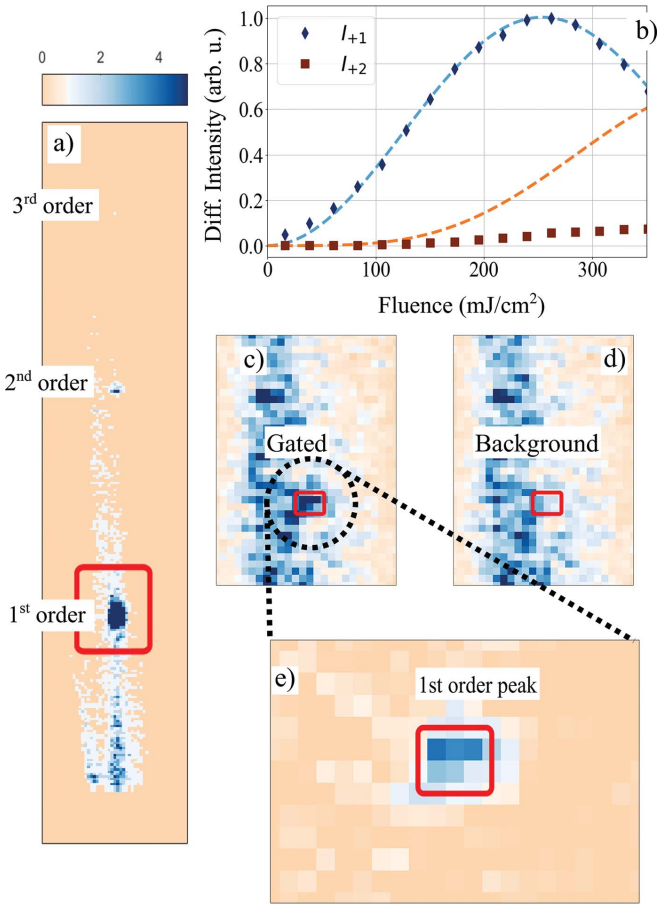

Figure 4
Synchrotron pulse gating. (*a*) Detector image depicting diffraction from a single synchrotron pulse in the first, second and third diffraction order. The pixel size is 55 µm × 55 µm, the red square marks the area (25 × 35 pixels) which is shown in (*c*) and (*d*). (*b*) Fluence dependence of the maximum diffracted intensity in the first (black diamonds) and second (brown squares) diffraction order. The dashed lines show calculated intensity using equation (1). The intensity of the first and the second order do not have the predicted ratio. (*c*, *d*) Diffraction in the first order with an external detector gate width of 50 µs, *i.e.* averaging 255 X-ray pulses from the synchrotron. Both images show the region marked with a red square in (*a*) and use the same colorscale. The long streak stems from diffuse surface scattering. The first diffraction order in the gated [(*c*)] and background [(*d*)] image is marked by the red rectangle. (*e*) Background-corrected image (20 × 12 pixels) of the first-order diffraction peak. The image was produced by subtracting the images (*c*) and (*d*).

In order to maximize the diffraction efficiency in the first order, we perform a fluence scan similar to Fig. 1(*b*). From the transient diffraction measurement we determined the delay of maximum diffraction from the thermal TG and subsequently scan the excitation fluence at that fixed delay. The result of that scan is shown in Fig. 4(*b*) for diffraction into the first (I_{+1}) and second (I_{+2}) orders. The maximum of I_{+1} is reached at a fluence of 250 mJ cm^{-2} and the fluence dependence follows the predicted Bessel-function from equation (1). However, comparison with the intensity of the direct beam yields a diffraction efficiency of only 0.1%, *i.e.* much lower than the expected 33% from our diffraction model. The dashed blue lines depict results of our diffraction model [*cf.* equation (1) and (2)] normalized to the measured I_{+1}. The calculated intensity in the second order is significantly lower than the values, indicating deviations of the surface deformation from a pure sine modulation. We will discuss possible distortion mechanisms in more detail in the next section.

Now we determine the on–off contrast of our pulse picking scheme: we increase the detector gate width from 140 ns to 50 µs so that each image accumulates the intensity of 255 X-ray pulses with a spacing of 196 ns each. For the image shown in Fig. 4(*c*) a thermal TG was excited to select one of the 255 pulses incident on the sample. The image shown in Fig. 4(*d*) was accumulated over 255 pulses without exciting a thermal TG, *i.e.* all intensity stems from accumulated background. Both images show strong diffuse scattering and look similar at the first glance. Only a few pixels, which are marked by the red square, show a difference in intensity, which stems from the single selected pulse from the thermal TG. To remove the accumulated background, we subtract images (*c*) and (*d*). The result is shown in Fig. 4(*e*). The intensity of the selected pulse is 2.1 times the intensity of the accumulated background in the same pixel which corresponds to an on–off contrast of ∼550 (Sander *et al.*, 2016, 2019). If the theoretical diffraction efficiency of 33% were achieved, the on–off contrast would exceed 10^5. In the next section, we will elucidate current limitations of the pulse picker and lay out improvements that enhance the performance to the theoretical optimum.

5. Current limitations and future improvements of the pulse picking scheme

Data measured at ID09, ESRF (not shown), and at P23, PETRA III [*cf.* Fig. 4], show significantly lower intensity in higher diffraction orders than expected. A reasonable explanation for this deviation is suggested by the splitting of the diffraction peaks that is highlighted in the inset of Fig. 1(*c*). The laser-induced thermal TG excitation of the sample leads to deformations on different length scales. First and foremost there is the expected surface modulation from the TG with a period of a few micrometres. The surface amplitude required to reach the maximum diffraction efficiency from the grating varies between 2 nm and 5 nm, depending on the actual experimental configuration (Sander *et al.*, 2017*b*). Second, we also expect a long-range modulation of the surface on the length scale of the excitation area due to accumulated heat in

the substrate (Shayduk & Gaal, 2020). The rising and falling slope of such deformations results in additional tilting of the diffraction geometry (Reinhardt *et al.*, 2016), thus generating the observed splitting of the diffraction peaks. The deformation amplitude h may be much larger than the thermal TG surface amplitude. An approximate sketch of such a total surface deformation is depicted in Fig. 5(*a*).

In order to estimate the effect of h on the diffraction efficiency in the +1st order, we include a Gaussian long-range surface modulation $\delta(r_\parallel)$ with amplitude h in equation (1) resulting in

$$\tilde{I}_n = \left| \frac{1}{r_0} \int_{r_\parallel} \exp\left(i \left\{ \frac{\Delta\varphi}{2} \left[\sin(q_\parallel r_\parallel) + \delta(r_\parallel) \right] - n \cdot q_\parallel r_\parallel \right\} \right) \mathrm{d}r \right|^2 = |\varphi|^2. \quad (4)$$

To evaluate the effect of $\delta(r_\parallel)$ on the diffraction efficiency, we depict the ratio of the diffracted intensity from the distorted and undistorted surface $\tilde{I}_{+1}/I_{+1}$ as a function of the distortion amplitude h by the blue line in Fig. 5(*b*). A similar ratio for the second-order diffraction $\tilde{I}_{+2}/I_{+2}$ is depicted in the dark red line. The calculation assumes a grating period of 2 µm, an incidence angle α_i of 0.2° and a surface amplitude u of 3.12 nm. Already small long-range thermal deformations result in a fast drop in the diffracted intensity. It is apparent that the higher-order intensity drops more rapidly upon increase of h. The reason for the drop in intensity is a dephasing of the reflected beam across the excitation region, as shown by the oscillating imaginary part of the diffraction integral φ in equation (4) (light orange dashed line). We estimated the influence of the surface roughness on the diffracted intensity in a similar way by replacing the long-range distortion $\delta(r_\parallel)$ with short-range random height fluctuations. The estimation predicts that realistic roughness values as measured on our samples with an atomic force microscope have no noticeable influence on the diffracted intensity.

Although equations (1) and (4) yield reasonable estimations of the diffracted intensity, the model is limited to diffraction below the critical angle of total reflection. For larger incidence angles, propagation effects in the medium may become important, which are not considered in the calculation of $\tilde{I}_{+1}$. In order to better estimate the real diffraction efficiency and in order to find the best operation conditions for the pulse picker, we perform ray-tracing simulations of grazing incidence diffraction from sinusoidal surface deformations imprinted on our sample.

Figure 5(*c*) depicts the simulated diffracted intensity as a function of the deformation amplitude for a perfect and for a rough surface (light and dark red line) of the LAO/LSMO/DSO heterostructure sample. The X-ray energy in the simulation was 10.2 keV and the incidence angle was 0.15°. As expected from equation (4) there is only negligible influence of the surface roughness. However, the peak diffracted intensity is only 25% and therefore lower than the theoretical maximum. The efficiency may be improved by coating the sample with a dense material, *e.g.* platinum (Pt) (blue line). Here, the theoretical diffraction maximum is reached at a slightly higher surface amplitude of 1.65 nm. Finally, we compare the influence of the spatial periodicity Λ on the diffracted intensity I_{+1}. Larger spatial periods require higher surface amplitudes to reach similar diffraction efficiency. In addition the angular separation of specular and first-order diffraction decreases, which makes it more difficult to separate the isolated diffracted pulse from the specular background. This behavior is also expected from our theoretical model [*cf.* equations (1) and (2)].

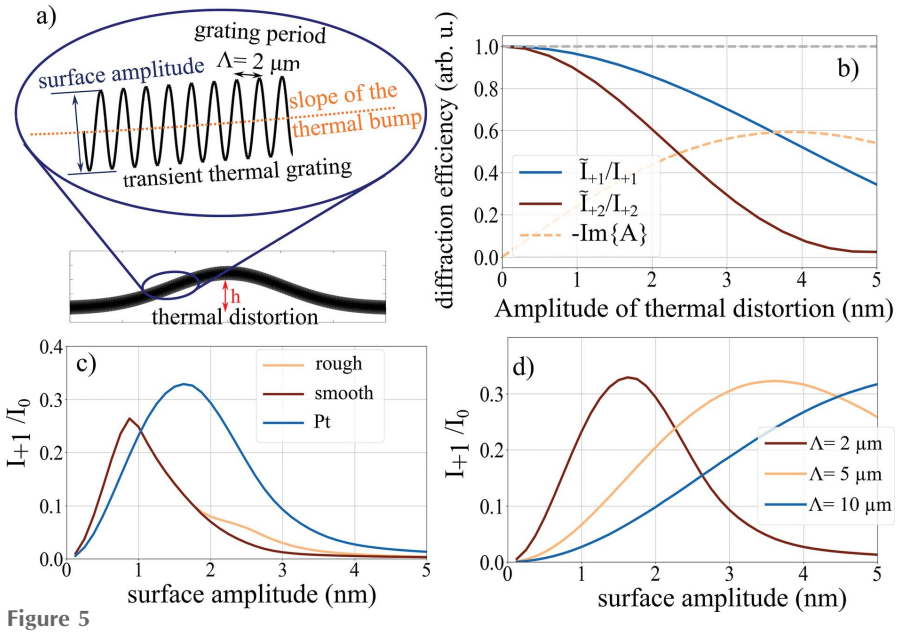

Figure 5
Optimization of the NanoGate performance. (*a*) Surface profile after TG excitation consisting of a long-range thermal distortion and a short-range thermal grating. (*b*) Theoretical diffraction efficiency from the surface profile shown in (*a*). (*c*) Diffracted intensity in the first order versus surface amplitude for different surface properties. (*d*) Diffraction efficiency versus surface amplitude for optimized structures at different TG periods.

6. Conclusion

In conclusion we have demonstrated a new method for selecting individual synchrotron X-ray pulses based on laser-induced thermal transient gratings. To achieve sufficient surface amplitudes, we employ nanosecond optical pump pulses. The optical excitation allows for controlling the surface deformation on timescales of the order of the excitation pulse. In first measurements we successfully demonstrated pulse gating although the theoretical limit of the diffraction efficiency was not reached. However, the switching contrast, which

is the more challenging parameter for a pulse picker, is similar to alternative pulse picking schemes, provided the diffraction efficiency can be increased in future experiments.

Our simulations outline a pathway to an improved performance of the pulse picking scheme. A major challenge for the implementation of this method is avoiding the long range thermal distortion. This could be achieved by a combination of sample cooling and use of different substrate materials. Further improvements consist of depositing a high-density coating on the sample surface. Pt seems to be an adequate material which has already been investigated in strong optical pumping conditions (Shayduk *et al.*, 2016). Under optimal conditions we expect a diffraction efficiency from the grating of up to 30%. The pulse picker especially suits conditions at fourth-generation synchrotrons due to the small beam size, high collimation and relatively narrow spectral width.

Acknowledgements

We gratefully acknowledge assistance from Matteo Levantino and Michael Wulff during measurements at ID09, ESRF. Open Access funding enabled and organized by Projekt DEAL.

Funding information

Funding for this research was provided by: Bundesministerium für Bildung und Forschung (grant No. FK05K16GU3 to Peter Gaal).

References

Berman, L. E. & Hart, M. (1991). *Nucl. Instrum. Methods Phys. Res. A*, **302**, 558–562.
Bojahr, A., Gohlke, M., Leitenberger, W., Pudell, J., Reinhardt, M., von Reppert, A., Roessle, M., Sander, M., Gaal, P. & Bargheer, M. (2015). *Phys. Rev. Lett.* **115**, 195502.
Chen, P., Jung, I. W., Walko, D. A., Li, Z., Gao, Y., Shenoy, G. K., López, D. & Wang, J. (2019). *Nat. Commun.* **10**, 1158.
Ejdrup, T., Lemke, H. T., Haldrup, K., Nielsen, T. N., Arms, D. A., Walko, D. A., Miceli, A., Landahl, E. C., Dufresne, E. M. & Nielsen, M. M. (2009). *J. Synchrotron Rad.* **16**, 387–390.
Förster, D. F., Lindenau, B., Leyendecker, M., Janssen, F., Winkler, C., Schumann, F. O., Kirschner, J., Holldack, K. & Föhlisch, A. (2015). *Opt. Lett.* **40**, 2265.
Gembicky, M. & Coppens, P. (2007). *J. Synchrotron Rad.* **14**, 133–137.
Goldshteyn, J., Bojahr, A., Gaal, P., Schick, D. & Bargheer, M. (2014). *Phys. Status Solidi B*, **251**, 821–828.
Goto, T., Nakamori, H., Kimura, T., Sano, Y., Kohmura, Y., Tamasaku, K., Yabashi, M., Ishikawa, T., Yamauchi, K. & Matsuyama, S. (2015). *Rev. Sci. Instrum.* **86**, 043102.
Grigoriev, A., Do, D., Kim, D. M., Eom, C., Evans, P. G., Adams, B. & Dufresne, E. M. (2006). *Appl. Phys. Lett.* **89**, 021109.
Hand, E. (2009). *Nature*, **461**, 708–709.
Holldack, K., Ovsyannikov, R., Kuske, P., Müller, R., Schälicke, A., Scheer, M., Gorgoi, M., Kühn, D., Leitner, T., Svensson, S., Mårtensson, N. & Föhlisch, A. (2014). *Nat. Commun.* **5**, 4010.
Husheer, S. L. G., Cole, J. M., d'Almeida, T. & Teat, S. J. (2012). *Rev. Sci. Instrum.* **81**, 043905.
Ito, K., Penent, F., Hikosaka, Y., Shigemasa, E., Suzuki, I. H., Eland, J. H. D. & Lablanquie, P. (2009). *Rev. Sci. Instrum.* **80**, 123101.
Jankowiak, A. & Wüstefeld, G. (2013). *Synchrotron Radiat. News*, **26**, 22–24.
Janušonis, J., Chang, C. L., Jansma, T., Gatilova, A., Vlasov, V. S., Lomonosov, A. M., Temnov, V. V. & Tobey, R. I. (2016). *Phys. Rev. B*, **94**, 024415.
Janušonis, J., Jansma, T., Chang, C. L., Liu, Q., Gatilova, A., Lomonosov, A. M., Shalagatskyi, V., Pezeril, T., Temnov, V. V. & Tobey, R. I. (2016). *Sci. Rep.* **6**, 29143.
Käding, O. W., Skurk, H., Maznev, A. A. & Matthias, E. (1995). *Appl. Phys. A*, **61**, 253–261.
Knoester, J. & Mukamel, S. (1991). *Phys. Rep.* **205**, 1–58.
Kudo, T., Hirono, T., Nagasono, M. & Yabashi, M. (2009). *Rev. Sci. Instrum.* **80**, 093301.
LeGrand, A. D., Schildkamp, W. & Blank, B. (1989). *Nucl. Instrum. Methods Phys. Res. A*, **275**, 442–446.
McPherson, A., Lee, W. & Mills, D. M. (2002). *Rev. Sci. Instrum.* **73**, 2852–2855.
Meents, A., Reime, B., Kaiser, M., Wang, X.-Y., Abela, R., Weckert, E. & Schulze-Briese, C. (2009). *J. Appl. Cryst.* **42**, 901–905.
Mukhopadhyay, D., Walko, D. A., Jung, I. W., Schwartz, C. P., Wang, J., López, D. & Shenoy, G. K. (2015). *Nat. Commun.* **6**, 7057.
Pennicard, D., Lange, S., Smoljanin, S., Hirsemann, H., Graafsma, H., Epple, M., Zuvic, M., Lampert, M., Fritzsch, T. & Rothermund, M. (2013). *J. Phys. Conf. Ser.* **425**, 062010.
Plogmaker, S., Linusson, P., Eland, J. H. D., Baker, N., Johansson, E. M. J., Rensmo, H., Feifel, R. & Siegbahn, H. (2012). *Rev. Sci. Instrum.* **83**, 013115.
Pudell, J., Sander, M., Bauer, R., Bargheer, M., Herzog, M. & Gaal, P. (2019). *Phys. Rev. Appl.* **12**, 024036.
Quintana, J. P., Hart, M., Bilderback, D., Henderson, C., Richter, D., Setterston, T., White, J., Hauserman, D., Krumrey, M. & Schulte-Schrepping, H. (1995). *J. Synchrotron Rad.* **2**, 1–5.
Reinhardt, M., Koc, A., Leitenberger, W., Gaal, P. & Bargheer, M. (2016). *J. Synchrotron Rad.* **23**, 474–479.
Rogers, J. A., Maznev, A. A., Banet, M. J. & Nelson, K. A. (2000). *Annu. Rev. Mater. Sci.* **30**, 117–157.
Roshchupkin, D. V., Irzhak, D. V., Tucoulou, R. & Buzanov, O. A. (2003). *J. Appl. Phys.* **94**, 6692–6696.
Sander, M., Bauer, R., Kabanova, V., Levantino, M., Wulff, M., Pfuetzenreuter, D., Schwarzkopf, J. & Gaal, P. (2019). *J. Synchrotron Rad.* **26**, 1253–1259.
Sander, M., Herzog, M., Pudell, J. E., Bargheer, M., Weinkauf, N., Pedersen, M., Newby, G., Sellmann, J., Schwarzkopf, J., Besse, V., Temnov, V. V. & Gaal, P. (2017*a*). *Phys. Rev. Lett.* **119**, 075901.
Sander, M., Koc, A., Kwamen, C. T., Michaels, H., Reppert, A., Pudell, J., Zamponi, F., Bargheer, M., Sellmann, J., Schwarzkopf, J. & Gaal, P. (2016). *J. Appl. Phys.* **120**, 193101.
Sander, M., Pudell, J., Herzog, M., Bargheer, M., Bauer, R., Besse, V., Temnov, V. & Gaal, P. (2017*b*). *Appl. Phys. Lett.* **111**, 261903.
Schoenlein, R. W., Chattopadhyay, S., Chong, H. H., Glover, T. E., Heimann, P. A., Shank, C. V., Zholents, A. A. & Zolotorev, M. S. (2000). *Science*, **287**, 2237–2240.
Schroer, C. G., Agapov, I., Brefeld, W., Brinkmann, R., Chae, Y.-C., Chao, H.-C., Eriksson, M., Keil, J., Nuel Gavaldà, X., Röhlsberger, R., Seeck, O. H., Sprung, M., Tischer, M., Wanzenberg, R. & Weckert, E. (2018). *J. Synchrotron Rad.* **25**, 1277–1290.
Shayduk, R. & Gaal, P. (2020). *J. Appl. Phys.* **127**, 073101.
Shayduk, R., Pennicard, D., Krausert, K., Gaal, P., Volkov, S., Vonk, V., Hejral, U., Jankowski, M., Reinhardt, M., Leitenberger, W. & Stierle, A. (2017). *J. Synchrotron Rad.* **24**, 1082–1085.
Shayduk, R., Vonk, V., Arndt, B., Franz, D., Strempfer, J., Francoual, S., Keller, T. F., Spitzbart, T. & Stierle, A. (2016). *Appl. Phys. Lett.* **109**, 043107.
Stoupin, S., Lenkszus, F., Laird, R., Goetze, K., Kim, K. & Shvyd'ko, Y. (2010). *Proc. SPIE*, **7803**, 780307.

Tucoulou, R., Roshchupkin, D. V., Schelokov, I. A., Brunel, M., Ortega, L., Ziegler, E., Lingham, M., Mouget, C. & Douillet, S. (1997). *Nucl. Instrum. Methods Phys. Res. B*, **132**, 207–213.
Vadilonga, S., Zizak, I., Roshchupkin, D., Evgenii, E., Petsiuk, A., Leitenberger, W. & Erko, A. (2017*a*). *J. Appl. Cryst.* **50**, 525–530.
Vadilonga, S., Zizak, I., Roshchupkin, D., Petsiuk, A., Dolbnya, I., Sawhney, K. & Erko, A. (2017*b*). *Opt. Lett.* **42**, 1915.
Waldrop, M. M. (2014). *Nature*, **505**, 604–606.
Wang, S., Wendt, A. E., Boffard, J. B. & Lin, C. C. (2015). *Rev. Sci. Instrum.* **86**, 013111.
Weckert, E. (2015). *IUCrJ*, **2**, 230–245.
Wulff, M., Plech, A., Eybert, L., Randler, R., Schotte, F. & Anfinrud, P. (2002). *Faraday Disc.* **122**, 13–26.
Yashchuk, V. V., Morrison, G. Y., Marcus, M. A., Domning, E. E., Merthe, D. J., Salmassi, F. & Smith, B. V. (2015). *J. Synchrotron Rad.* **22**, 666–674.

Strain induced magnetization precession in Pt/Co/Pt multilayers

R. Bauer,[1] J. Wagner,[1]
H.P. Oepen,[1] and P. Gaal[1, 2]

[1] *Institute for Solid State and Nanostructure Physics, Universität Hamburg, Luruper Chaussee 149, 22607 Hamburg, Germany*
[2] *Leibniz-Institut fr Kristallzchtung, Max-Born-Strae 2, 12489 Berlin, Germany**

(Dated: October 31, 2022)

We investigate the influence of coherent and thermal strain on the generation of a magnetization precession in ferromagnetic Co/Pt multilayers by performing two experiments, namely conventional optical pump probe and optical transient grating (TG) excitation. In both cases we detect the perpendicular magnetization component M_z. In our experimental geometry, laser heating and subsequent demagnetization do not result in a torque on the magnetization vector. While the single pulse excitation induces only weak precession of the magnetization vector, the TG results in strong dynamics when the acoustic waves are in ferromagnetic resonance. We also observe parametric frequency generation and a deviation of the ferromagnetic resonance frequency from values predicted for an unperturbed system. Both observations point towards a strong influence of a thermal strain on the magnetic anisotropy in the sample which is rarely taken into account for optically induced magnetization precession.

PACS numbers:

I. INTRODUCTION

Ultrafast demagnetization is the generic process to induced magnetization dynamics in ferro and antiferromagnetic systems. Although being studied for over 20 years since the groundbreaking discovery of sub-100 fs optical demagnetization[1] in nickel, there is still ongoing controversy of the physical mechanisms involved. Never the less, optically induced magnetization dynamics has boosted our understanding of magnetic systems, in particular on the nanoscale. The large interest stems from the many applications of magnetic materials, especially in information technology. The applications are based on the ability to orient and freeze the magnetic polarization. Alternatives to the optical demagnetization mechanism are magnetic field-induced[2,3] and acoustic magnetization switching[4]. The latter gained significant attention recently due to the ability to generate high-frequency bulk and surface acoustic waves (BAWs and SAWs, respectively) in solids. The effect of picosecond strain pulses on the magnetization was first shown in the magnetic semiconductor (Ga,Mn)As[5] and several other systems where investigated since then. By generating optical transient gratings, the coupling of SAWs with the ferromagnetic polarization in nickel has been studied in detail recently[6,7]. In summary, optical strain generation gives access to ultrafast timescales[8,9] and provides high flexibility and control of the induced deformation[10]. However, optical strain generation also induces sharp temperature changes and subsequent demagnetization effects.

In this article we disentangle the effects of optical excitation of ferromagnetic materials in respect to temperature driven and deformation driven magnetization dynamics. It should be noted that temperature effects not exclusively act on the magnetic polarization amplitude, as suggested by a simple demagnetization process. We present and analyze two experiments employing different optical excitation schemes, namely a single pulse optical excitation and a Transient Grating (TG) excitation. In the single pulse experiment the optical excitation leads to a fast temperature jump and subsequent cooling. Coherent sound waves generated in the magnetic film propagate into the substrate within few picoseconds. In the TG experiment we generate a periodic thermal TG and additional SAWs that can be observed in the magnetic system for several nanoseconds. We present detailed calculations of the time and temperature dependent effective anisotropy that explain our observations.

The article is organized as follows: our theoretical model is derived in Section II. The sample system and the experimental method is explained in section III. The influence of temperature on the magnetic system is outlined in section IV and experimental results are presented and discussed in section V.

II. FREE ENERGY DENSITY AND FERROMAGNETIC RESONANCE FREQUENCY

In this section, we summarize the basic theory of the magnetoelastic interaction that leads to dynamic changes of the magnetic anisotropy. The sample in the laboratory coordinate system exposed to an external magnetic field is depicted in Fig. 1 a). The z-axis is normal to the sample surface and an external magnetic field $\vec{B}_{ext}$ points along the y-axis. The optical excitation, which will be introduced in sec. III, generates either a uniaxial deformation parallel to the z-axis [cf. 1 b)] or a periodic deformation in the z-y-plane [cf. 1 c)]. We denote the polar angle from the z-axis to the sample plane and the azimuthal angle within the sample plane by θ and φ, respectively. The magnetization $\vec{M}$ is marked by a thick

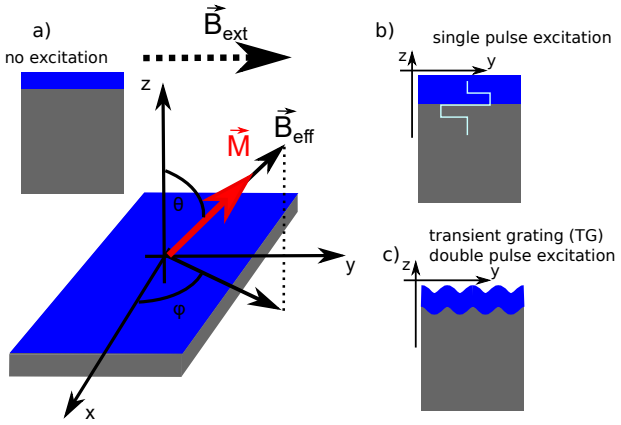

FIG. 1: a) Geometry of the experiment: The sample surface lies in the x-y- plane of the laboratory coordinate system. An external magnetic field is applied in y-direction. b) and c) optically induced deformations with a single pump pulse and with two interfering pump pulses, respectively. A single optical excitation pulse [(b)] generates a uniaxial thermal expansion and a longitudinal sound wave in z-direction. Interference of two light pulses [c) and Fig. 2] generates a periodic thermal deformation and surface acoustic modes that propagate in the z-y-plane.

red arrow in Fig. 1 a) and is directed parallel to the effective magnetic field $\vec{B}_{eff}$.

The magnetic properties can be fully derived from the magnetic part of free energy density f:

$$f = f_Z + K_{1,eff}\sin^2\theta + f_{me} \tag{1}$$

where $f_Z = -\vec{B}_{ext}\cdot\vec{M}$ is the Zeeman energy density. $K_{1,eff}$ is the effective first-order anisotropy constant that includes crystal field, shape and surface anisotropy K_{1V}, K_{shape} and K_{1S}, respectively:

$$K_{1,eff} = K_{1V} - K_{shape} + \frac{2K_{1S}}{d_{Co}} \tag{2}$$

The last term of the Eq. 1 is the magneto-elastic free energy contribution

$$\begin{aligned} f_{me} &= B_1(\epsilon_1' m_1'^2 + \epsilon_2' m_2'^2 + \epsilon_3' m_3'^2) \\ &+ B_2(\epsilon_4' m_2' m_3' + \epsilon_5' m_1' m_3' + \epsilon_6' m_1' m_2') \end{aligned} \tag{3}$$

where ϵ_i' are strain tensor components in the crystal coordinate system. B_1 and B_2 are the magnetoelastic coupling constants and $m_i' = M_i'/M_S$ are components of the magnetization direction with respect to crystal axes. M_S denotes the saturation magnetization.

The direction of the effective field $\vec{B}_{eff}$ is derived from the gradient of the free energy density

$$\vec{B}_{eff} = -\nabla_M f \tag{4}$$

Time-dependent changes of the orientation of the effective magnetic field act as a source term for magnetization precession as described by the Landau-Lifschitz-Gilbert (LLG) equation

$$\frac{d\vec{M}}{dt} = -\gamma\vec{M}\times\vec{B}_{eff} \tag{5}$$

Assuming single-domain behaviour and constant magnitude of the magnetization ($|\vec{M}(t)| = \text{constant}$), we convert Eq. 5 in spherical coordinates:

$$\frac{\partial\varphi}{\partial t} = \frac{\gamma}{M_S\sin\theta}\frac{\partial f}{\partial\theta}\,, \quad \frac{\partial\theta}{\partial t} = -\frac{\gamma}{M_S\sin\theta}\frac{\partial f}{\partial\varphi}\,. \tag{6}$$

The resonance frequency can be calculated assuming $\vec{M}(t) = \vec{M}(0)e^{i\omega t}$ by linearizing the torque with respect to magnetization components and expressing them as second derivatives of free energy density.[11]

$$\omega_0 = \frac{\gamma}{M_S\sin\theta}\sqrt{f_{\theta\theta}f_{\varphi\varphi} - f_{\theta\varphi}^2} \tag{7}$$

where $f_{ij} = \frac{\partial^2 f}{\partial i\partial j}$ with $i,j\in\{\theta,\varphi\}$. Application of Eq. 7 to our system with an effective anisotropy given by Eq. 2 yields

$$\omega_0 = \gamma\sqrt{B_y^2 - \frac{2K_{1,eff}}{M_S}B_y} \tag{8}$$

which is the equivalent to the Kittel formula for the in-plane geometry.

III. SAMPLE SYSTEM AND EXPERIMENTAL METHOD

The sample is a ferromagnetic Pt/Co multilayer which was grown by magnetron and ECR sputtering at high temperatures on a glass substrate.[12,13] The bottom Pt layer (6 nm) provides a texture that leads to fcc-growth of the Co/Pt doublelayer with the [111]-axis parallel to the surface normal, i.e., along the z-axis of the laboratory frame. In the sample plane, the metal films have no preferred orientation and consist of individual grains with polycrystalline order.[14] The thickness of the Co and Pt layer is 2 nm and 1 nm, respectively. The sample contains six periodes of Co/Pt doublelayers and is capped with 3 nm thick Pt to protects the stack from oxidation. The sample structure is depicted in Fig. 2 a).

In order to calculate the magnetoelastic contribution to the free energy density in each individual grain, we have to transform components of the strain and of the magnetization, which are defined in the laboratory frame, into the crystalline coordinate system. This can be accomplished by the linear transformation

$$\begin{aligned} \epsilon' &= P\epsilon P^T \\ \vec{m}' &= P\vec{m}, \end{aligned} \tag{9}$$

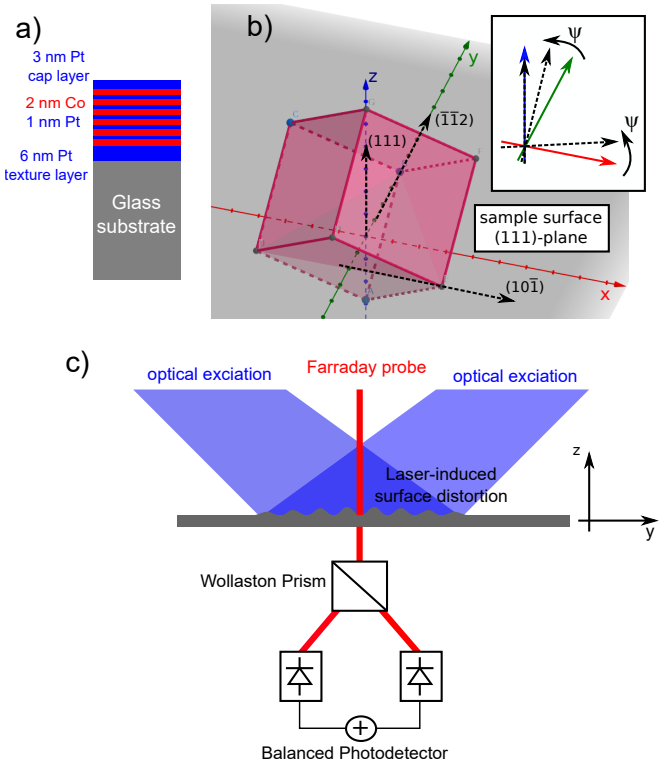

FIG. 2: a) Sketch of the sample layout (see text for details). b) Orientation of the crystal coordinate system (black dashed arrows) in the laboratory frame (colored axes). Due to the [111] texture of Co, the [111] crystal axes is aligned with the z-axes of the laboratory frame, independent of the orientation of the particular grain. The inset shows the in-plane rotation of the grain around the z-axis by the angle ψ. c) schematic of the optical setup: two interfering optical excitation pulses generate a transient grating (TG), that launches coherent acoustic surface waves. Changes of the magnetization component M_z are detected by recording the polarization change of an optical probe pulse.

where

$$P = \begin{pmatrix} -\frac{1}{\sqrt{2}} & -\frac{1}{\sqrt{6}} & \frac{1}{\sqrt{3}} \\ \frac{1}{\sqrt{2}} & -\frac{1}{\sqrt{6}} & \frac{1}{\sqrt{3}} \\ 0 & \sqrt{\frac{2}{3}} & \frac{1}{\sqrt{3}} \end{pmatrix} \tag{10}$$

denotes the change of basis matrix[15] and the primed and unprimed variables denote quantities in the crystalline and the laboratory coordinate system, respectively. The transformation is depicted in Fig. 2 b).

Since the in-plane orientation of the individual grains is random, we need to calculate an average value of ϵ' and $\vec{m}'$ by rotating the crystal in the x-y-plane of the laboratory frame. The rotation is given by:

$$\begin{aligned} \epsilon' &= PR(\psi)\epsilon R^T(\psi)P^T \\ \vec{m}' &= PR(\psi)\vec{m}, \end{aligned} \tag{11}$$

where $R(\psi)$ denotes the rotation matrix. The rotation of the grain is sketched in the inset of Fig. 2 b). We want to stress that ψ and φ are both angles in the xy-plane. However, ψ represents the orientation of a grain while φ denotes the orientation of the magnetization.

Having performed the necessary transformation [cf. Eq. 11] of the crystalline grains, we finally calculate the average magnetoelastic energy density for our samples by integrating over the polycrystalline ensemble of grains:

$$\bar{f}_{me}(\theta,\varphi) = \frac{1}{2\pi}\int_0^{2\pi} f_{me}(\theta,\varphi,\psi)\, d\psi \tag{12}$$

We use $\bar{f}_{me}$ to calculate the dynamic response of our sample after optical excitation using Eq. 5 and 6.

The experimental setup is schematically depicted in Fig. 2 c) and discussed in detail elsewhere[6,7]. We use a commercial Ti:sapphire laser system (Coherent Legend Elite) which delivers optical pulses at λ=800 nm wavelength with a duration of 120 fs at a repetition rate of 1 kHz. The excitation pulses are frequency doubled to λ=400 nm, the probe pulse is kept at the fundamental wavelength. Interference of two replica of the optical pump pulse leads to a modulation of the optical intensity in the sample surface plane. Absorption of such an optical excitation pattern generates periodic thermal surface expansion and launch coherent acoustic modes which propagate in y-direction in the laboratory frame[10,16,17]. This is the so-called transient grating (TG) excitation.

We monitor the perpendicular component M_z of the magnetization vector by detecting changes of the polarization vector of the optical probe pulse using a Wollaston prism and a pair of balanced photodiodes. The accessible delay range in our setup was 8 ns.

IV. TEMPERATURE-INDUCED CHANGES OF THE FREE ENERGY DENSITY

Absorption of ultrashort optical pulse in a metal film leads to a fast temperature increase which is accompanied by thermal expansion and impulsive generation of coherent phonons. The rise of the temperature results in reduction of the saturation magnetization, effective anisotropy and magnetoelastic constants. The temperature dependence of the saturation magnetization over a wide range of temperatures for fcc Co was described by Kuzmin et al.[18] and leads to the change of the shape anisotropy $\mu_0\frac{M_S(T)^2}{2}$. The theory of the temperature dependence of other components of $K_{1,eff}$ and magnetoelastic constants was derived by Akulov and Callen[19,20] and can be written as:

$$\frac{K(T)}{K(0)} = \left(\frac{M_S(T)}{M_S(0)}\right)^n, \quad \frac{B_{1,2}(T)}{B_{1,2}(0)} = \left(\frac{M_S(T)}{M_S(0)}\right)^n \tag{13}$$

where $n = 3$ for uniaxial anisotropy.. Temperature dependence of magnetization and components of the effective anisotropy constant are shown in Fig. 3.

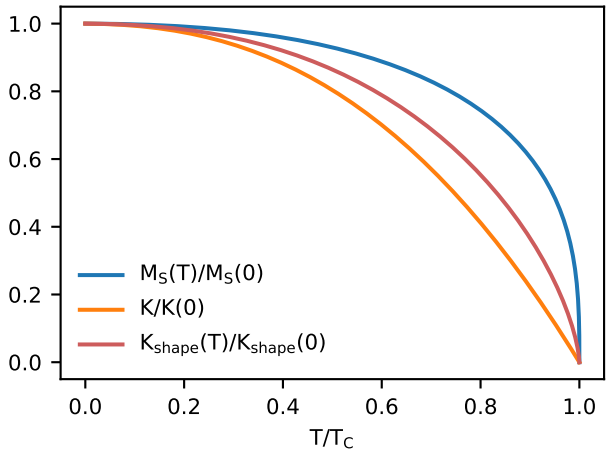

FIG. 3: Temperature dependence of magnetization, shape, volume and surface anisotropy. For rising temperature shape anisotropy is reduced according to $M_S(T)^2$ while surface and volume anisotropies are reduces with $M_S(T)^n$, where n is assumed to be 3 for uniaxial anisotropy.

In order to determine the transient demagnetization of the sample, we solve the one-dimensional heat diffusion equation in our sample after impulsive optical excitation[21] and find phonon and electron temperatures T_{el} and T_{ph}, respectively, using a two-temperature model of coupled rate equations[22,23]:

$$\begin{aligned} c_{el}(T_{el})\frac{\partial T_{el}}{\partial t} &= \frac{\partial}{\partial z}\left[k_{el}\frac{\partial T_{el}}{\partial z}\right] + G_{e-p}(T_{ph}-T_{el}) + S \\ c_{ph}(T_{ph})\frac{\partial T_{ph}}{\partial t} &= \frac{\partial}{\partial z}\left[k_{ph}\frac{\partial T_{ph}}{\partial z}\right] + G_{e-p}(T_{el}-T_{ph}) \end{aligned} \tag{14}$$

The optical pump pulse is initially absorbed by conduction band electrons in Co and Pt. The kinetic energy of the electrons is subsequently transferred to the lattice via electron-phonon coupling, thus increasing the phonon temperature T_{ph}. Parameters for the simulation are given in Table I. Our results match previous measurements and simulations of the perpendicular magnetization of Co nanostructures[24].

	α_L [1/K]	δ [nm]	c_p [J/(kg·K)]	k [$\frac{W}{m \cdot K}$]	G_{e-p} [1/s]
Co	$1.3 \cdot 10^{-5}$	11.4	$c_{el} = 0.08 \cdot T_{el}$ $c_{ph} = 419.1 \cdot T_{ph}$	100	$9.3 \cdot 10^{17}$
Pt	$8.8 \cdot 10^{-6}$	11.2	$c_{el} = 0.0345 \cdot T_{el}$ $c_{ph} = 129.6 \cdot T_{ph}$	72	$2.5 \cdot 10^{17}$

TABLE I: Parameters used for two-temperature model simulation of laser-induced heating of Pt/Co multilayer samples. α_L, δ , c_p, k and G_{e-p} denote the linear thermal expansion coefficient, optical penetration depth, specific heat capacity, thermal conductivity and the electron-phonon coupling time constant, respectively.

V. EXPERIMENTAL DATA

We performed two conceptually different series of measurements using the setup outlined in sec. III. In all experiments, the sample was exposed to an external magnetic field in y-direction $\vec{B}_{ext} = B_y$ with variable amplitude. For each field amplitude we probe the transient Faraday rotation of the optical probe pulse, which is proportional to the M_z-component of the magnetization vector. The setup is not sensitive to in-plane components of the magnetization. A Fast-Fourier Transform (FFT) is performed on the transient magnetization $M(f) = |\mathcal{F}\{M_z(t)\}|$.

The first series is measured with only one optical pump pulse exciting the sample. This excitation leads to the generation of coherent longitudinal acoustic phonons[25–28] propagating parallel to the surface normal into the sample and to a thermal expansion[29,30] as shown in Fig. 5 c).

In the second experiment the sample is excited by two interfering optical pump pulses. This transient grating (TG) excitation leads to a periodic thermal expansion at the sample surface and launches coherent surface acoustic waves (SAW) and surface skimming longitudinal waves (SSLW) which propagate in y-direction parallel to the external magnetic field along the surface[7,16,17].

Fig. 4 a) shows results of the single pulse excitation. The magnitude $|M(f)|$ is depicted for different external magnetic field amplitudes. The absorbed optical excitation fluence was 6.2 mJ/cm^2. For comparison, we calculate and show the ferromagnetic resonance (FMR) in the solid lines. The green curve depicts the FMR frequency calculated with the Kittel formula [cf. Eq. 8][31,32]. The blue solid line was calculated using Eq. 7 and including the magnetoelastic term f_{me} of the free energy density. The optically induced precession is weak but clearly overlaps with the predicted FMR frequencies. However, a quantitative comparison of both FMR models is not possible due to the high noise.

Fig. 4 b) shows $|M(f)|$ as a function of the external magnetic field amplitude after generation of TG. Again we also show the calculated field-dependent FMR calculated with the Kittel formula and with the full free energy density including the magnetoelastic interaction [cf. Eq. 7]. The data show a strong coupling of two acoustic modes to the precession of the magnetization vector. These mode have previously[7] been identified as the Rayleigh mode at a frequency $f_{SAW} = 2.4$ GHz and the SSLW mode at $f_{SSLW} = 4.5$ GHz. Comparison of the calculated FMR dependence yields a better agreement if the magnetoelastic term f_{me} is included in the calculation (blue line) compared. We also observe an off-resonant precession of the magnetization, e.g., at the energy of the SSLW-mode at an external field amplitude of 5 mT. Similar off-resonant precessions were observed in similar experiments in Ni films[33].

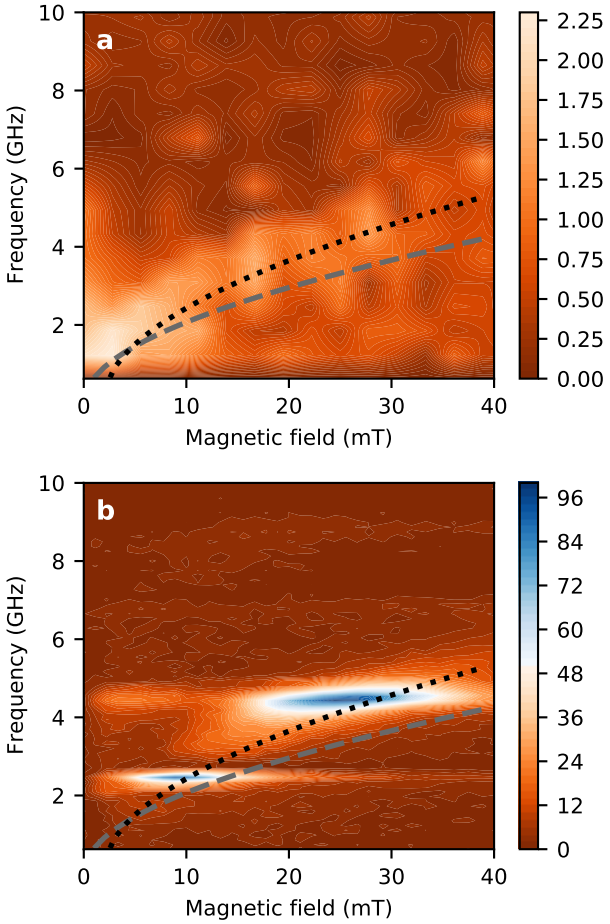

FIG. 4: Oscillation of the M_z component of the magnetization vector for different amplitudes of the external magnetic field $\vec{B}_{ext} = B_y$. a) Single pulse excitation. b) Transient Grating excitation with two interfering optical pump pulses. Single pulse excitation is multiple orders of magnitude weaker then the TG excitation. The dotted and dashed lines depict the FMR frequency with and without magnetostrictive coupling, respectively.

VI. DISCUSSION

A. Effects of transient heating on the anisotropy

To analyze the effect of the optical excitation on the magnetization, we simulated temperature-induced changes on the free energy as described in section IV. Results of our simulations are depicted in Fig. 5. After excitation with a short laser pulse electrons thermalize by electron-phonon scattering within few picoseconds, resulting in energy transfer and subsequent heating of the crystal lattice. The average transient electron and lattice temperatures are shown in Fig. 5 a). The optical excitation fluence absorbed in the sample is sufficient for raising the electron temperature in Co above the Curie temperature T_c. This results in complete demagnetization of the sample on the timescale of the optical excitation pulse length, as show in Fig. 5 b). A few picoseconds after the excitation, the electronic temperature of the sample has dropped below the T_c and an equilibrium between electron and lattice temperatures is reached. The magnetization is restored to about 80% of the initial value, followed by a slow increase of magnetization on the timescales of hundreds of picoseconds to nanoseconds. It is instructive to monitor the temperature difference of Pt and Co as well as the strain in Pt and Co in the multilayer. This is depicted by the blue, orange and black dashed lines in Fig. 5 c), respectively. A difference between the out-of-plane strain of Co and Pt persists even after almost complete thermal equilibration within the multilayer. Although our model does not comprise the in-plane strain, we assume that the strain difference along one direction leads also to in-plane deformations. Finally, we also calculate the transient effective anisotropy [c.f. Equ. 13 and Fig. 3] which is depicted in the black solid line in Fig. 5 d). Following laser-induced thermal demagnetization, contributions to the effective anisotropy, namely the volume and surface anisotropy (orange line) and the shape anisotropy (blue line) are reduced and subsequently restored to different fractions of their equilibrium level. As a result, the transient effective anisotropy is always at or below zero, i.e., $K_{1,eff} \leq 0$, and the easy magnetic axis always lies in the sample plane. Thus, in our configuration where the external magnetic field $\vec{B} = B_y$ is parallel to the sample plane, heat-induced demagnetization cannot result in a torque on the magnetization vector. Note that the Faraday probe is only sensitive to out-of-plane contributions of $\vec{M}$. Thus, we conclude that the magnetic precession in our sample system is not generated by a heat induced change of an effective anisotropy constant. This is in sharp contrast to the generally accepted model of optically induced magnetization precession upon laser heating[36]. We also point out that the magnetostriction constants $B_{1,2}$ have the same temperature dependence as the anisotropy constants K_V and K_S, respectively [c.f. Eq. 13]. In consequence, the magnetostrictive coupling is also reduced after absorption of the excitation laser pulse.

B. Single pulse excitation

In order to determine the excitation of the transient magnetic signal, we first discuss the data shown in Fig. 4 a). The sample is excited by a single excitation pulse, thus generating coherent longitudinal acoustic phonons and thermal expansion of the excited structure. The coherent phonon wave packet propagates with the speed of sound of 4.72 nm/ps and 2.8 nm/ps in Co and Pt, respectively, i.e., much faster than the measured frequencies in Fig. 4 a)[28,37,38]. Therefore, propagating coherent phonons have only negligible influence on the magnetization dynamics. However, transient strain that persists

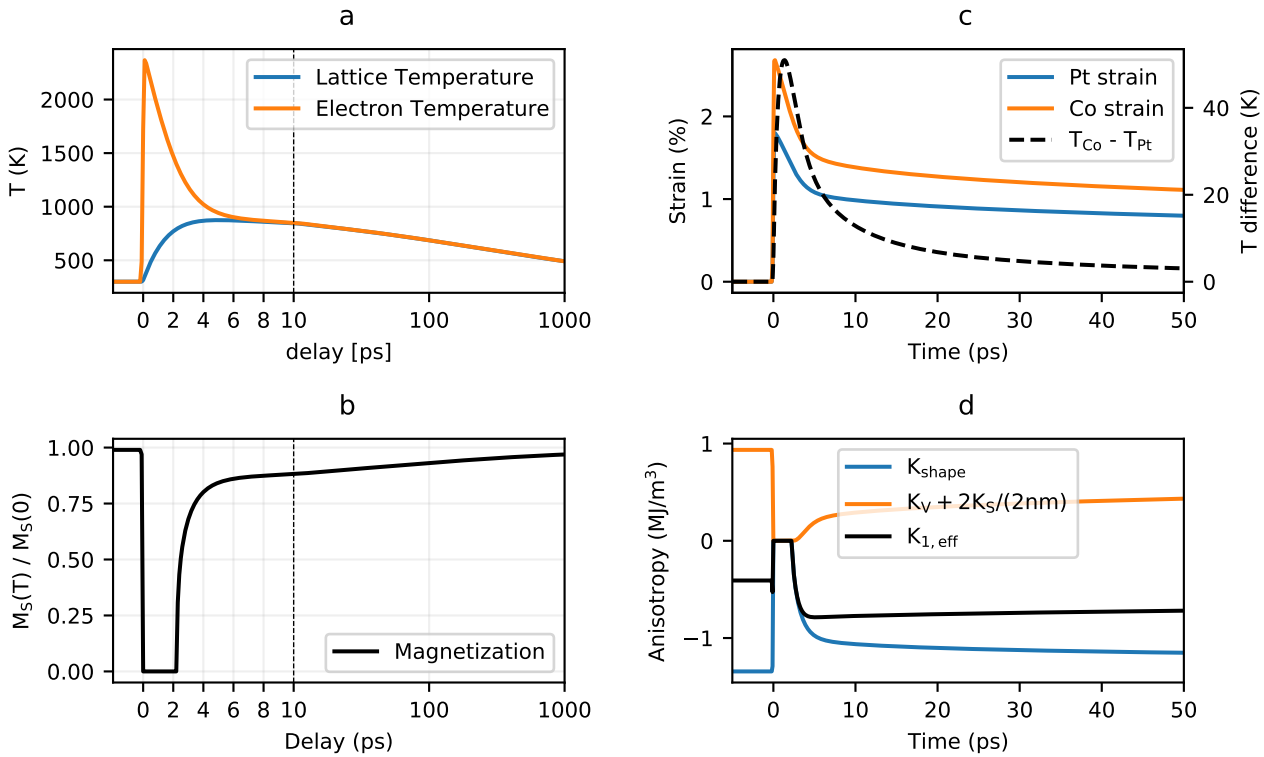

FIG. 5: a) Electron and lattice temperature in Co/Pt multilayer sample after excitation with a laser pulse with fluence of 6.2 mJ/cm^2. Temperatures of both subsystems equalize after a few picoseconds. b) Change of the saturation magnetization of fcc Co due to temperature change after an excitation with a laser pulse. c) Temperature induced strain and temperature difference of Pt and Co layers. d) Temperature dependence of anisotropy constant. Effective anisotropy constant stays negative after an excitation. Anisotropy constants were measured by Stillrich el al.[34] and J. Wagner[35]

long after optical excitation as shown in Fig. 5 c), could tilt the magnetization vector $\vec{M}$ away from its equilibrium position. In order to determine relevant components of the strain tensor that act on the magnetization, we calculate the torque on $\vec{M}$ using Eq. 6 with the full expression for the free energy density Eq. 1 including the magnetoelastic term given by Eq. 3: At the equilibrium position $\vec{M}(\theta = 90°, \varphi = 90°)$ most components of the strain tensor exert no torque on $\vec{M}$. Only strain components ϵ_1 and ϵ_2 for $\epsilon_1 \neq \epsilon_2$ induce torque τ_θ that can rotate the magnetization vector out of plane. Similarly, only the a shear strain in the y-z-plane ϵ_4 and x-z-plane ϵ_5 exerts a torque τ_ϕ on $\vec{M}$. Our interpretation is consistent with previously observed purely strain-induced magnetization precession[39].

Hence, a tensile strain, that is excited by thermal deformation of the multilayer system, could trigger precession of the magnetization vector. Even though the signal-to-noise level in Fig. 4 a) is low, we assume that the magnetostrictive interaction is the main driving force for the precession of the magnetization. A second indicator for this mechanism is the field-dependence of the precession frequency. Fig. 4 a) compares the observed magnetic field-dependent precession frequency (blue solid line) with a calculation that neglects the magnetostrictive interaction. Even at the low signal-to-noise level of our experiment the model that includes magnetostriction yields a better representation of the measured data.

C. Double pulse TG excitation

In order to investigate the magnetostrictive interaction in more detail, we generate coherent acoustic waves with frequencies close to the ferromagnetic resonance of the ferromagnet. In particular, by using the optical TG excitation[6,7], we launch Rayleigh and SSLW modes which propagate at least partially in the ferromagnetic multilayer. The free energy density of the multilayer sample including the optically excited acoustic waves reads:

$$f(\theta, \varphi, t) = -B_y M_S \sin\theta \sin\varphi + K_{1,eff} \sin^2\theta + \bar{f}_{me}(\theta, \varphi, \epsilon_2(t), \epsilon_3(t), \epsilon_4(t)). \quad (15)$$

Note that the acoustic waves propagate in-plane in y-direction. The strain tensor in the sample coordinate

system reads

$$\epsilon(t) = \begin{bmatrix} 0 & 0 & 0 \\ 0 & \epsilon_2(t) & \frac{1}{2}\epsilon_4(t) \\ 0 & \frac{1}{2}\epsilon_4(t) & \epsilon_3(t) \end{bmatrix} \tag{16}$$

with the time-dependence of the in-plane component

$$\begin{aligned} \epsilon_2(t) = \epsilon_{th} + A\cos(2\pi f_{saw} t)\exp\left(-\frac{t}{\tau_{saw}}\right) \\ + B\cos(2\pi f_{sslw} t + \delta)\exp\left(-\frac{t}{\tau_{sslw}}\right) \end{aligned} \tag{17}$$

Given a TG period of 1.7 μm we generate acoustic frequencies of 2.4 GHz and 4.5 GHz for the Rayleigh and SSLW mode, respectively. Resonant magnetostrictive coupling of the acoustic modes with the magnetization is clearly observed in the measurement depicted in Fig. 4 b). Again, the blue and green solid lines denote the calculated field-dependent ferromagnetic resonance frequency with and without magnetostrictive component f_{me} of the free energy density. With the high signal-to-noise ratio in this data it is now evident that the magnetostrictive term must be included in the free energy to obtain a good agreement of theory and experiment. We want to point out that the blue and green lines in Fig. 4 a) and b) are identical.

Now we interpret the off-resonant precession observed in Fig. 4 b), e.g., at a frequency of 4.5 GHz and a magnetic field of 5 mT. For that, we derive the ferromagnetic resonance frequency [c.f. Equ. 7] at the equilibrium point $\theta = 90°$ and $\varphi = 90°$. Note that we also incorporate the magnetostrictive interaction by incorporation of the time-dependent strain $\epsilon(t)$:

$$\omega_0 = \gamma g \sqrt{B_y^2 - B_y \frac{2K_{1,eff}}{M_S} + A\,\epsilon_2(t) + C\,\epsilon_3(t) + D\,\epsilon_2(t)\epsilon_3(t) + E\,\epsilon_2(t)^2 + F\,\epsilon_4(t)^2} \tag{18}$$

We discuss Eq. 18 only qualitatively: The first two terms denote contributions from anisotropy and Zeeman energy terms, respectively. The factors A and $C-F$ result from magnetostrictive interaction with different components of the strain tensor. Note that Eq. 18 becomes time-dependent for a time-dependent strain tensor $\epsilon(t)$: $\omega_0 \rightarrow \omega_0(t)$. This time-dependence of the resonance frequency is called a parametric modulation. A similar effect was already observed in Ni after TG excitation[33].

To compare our model with the experimental result we depict the precession frequency calculated using Eq. 18 in Fig. 6 a) together with the precession amplitude measured in the TG experiment on a logarithmic scale in Fig. 6 b). We observe a good qualitative agreement. In particular, the model reproduces the off-resonant precession at 4.5 GHz, 7 GHz and at 8.5 GHz.

We now analyze Eq. 18 in order to derive the relevant contributions of the strain tensor that couple to the precession of the magnetization vector. Table II summarizes the amplitude of terms A and $C-F$ assuming an equal strain components contribution of 1% in units of [T^2]. These terms compete with the combined amplitude of the strain-independent terms, i.e., the first two terms in Eq. 18, with a value of $\approx 30 \times 10^{-3}$ T^2.

The dominating magnetostrictive interaction terms are A and C which means that longitudinal (ϵ_3) and transverse (ϵ_2) strain are dominantly responsible for the observed parametric frequency modulation in the precession of $\vec{M}$. Shear and mixed strain terms depend quadratically on the strain and may be neglected. The A and C term reads:

Term	**A**	**C**	D	E	F
Value	**0.43**	**0.53**	7.2	0.23	-1.03
Strain	ϵ_2	ϵ_3	$\epsilon_2\epsilon_3$	ϵ_2^2	ϵ_4^2
Total	**4.3** $\times\mathbf{10}^{-3}$	**5.3** $\times\mathbf{10}^{-3}$	7.2 $\times 10^{-4}$	2.3 $\times 10^{-5}$	-1.03 $\times 10^{-4}$

TABLE II: Amplitude of the magnetostrictive coupling terms A and $C-F$ of Eq. 18. The total amplitude is calculated for an isotropic strain of 1%. The dominant terms A and C are printed in bold letters.

$$\begin{aligned} A &= \frac{4(B_1+B_2)K_{1,eff}}{3M_S^2} - \frac{(B_1+B_2)B_y}{M_S} \\ C &= \frac{2B_2 B_y}{M_S} \end{aligned} \tag{19}$$

As derived in Sec. VI A, both the effective anisotropy $K_{1,eff}$ and the magnetostriction constants $B_{1,2}$ depend on the sample temperature and are reduced by the optical excitation. At low external magnetic fields B_y the A-term dominates the parametric frequency mixing. At elevated B_y it is mainly the C-term which drives the magnetostrictive frequency modulation.

VII. CONCLUSION

In conclusion, we have studied the effect of lattice strain on the magnetization dynamics in thin ferromag-

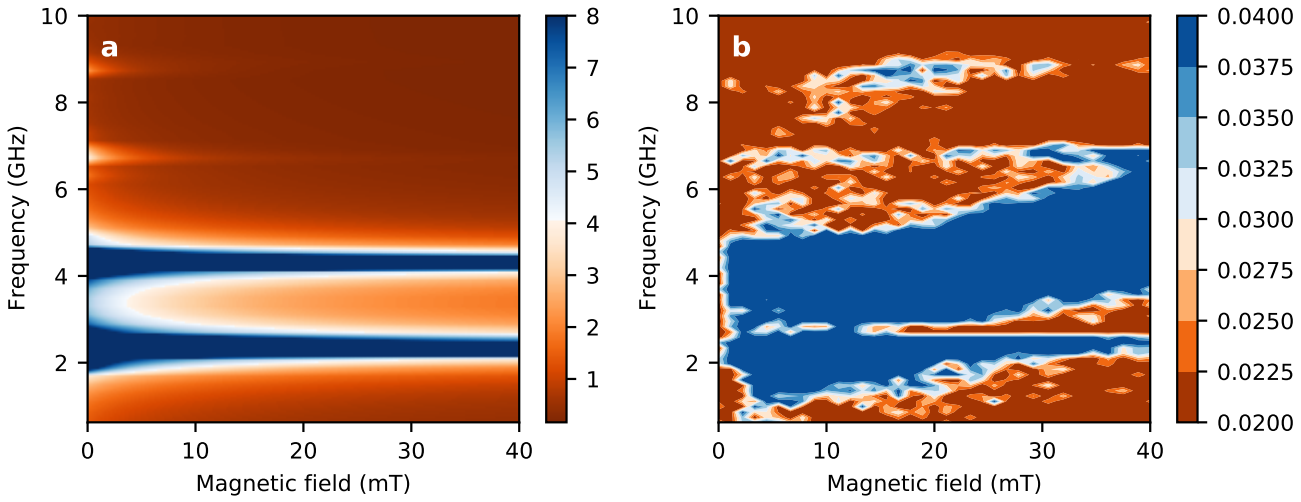

FIG. 6: a) Calculated precession frequency using Eq. 18. b) Average of the M_z component of the magnetization measured using Faraday rotation for TG excitation. Higher values are clipped for better contrast.

netic Co/Pt multilayers. Due to the in-plane direction of the external magnetic field in our experiment, laser-induced demagnetization of our sample does not exert a torque on the magnetization vector. Thus, the measured precession stems from a magentostrictive coupling. In a typical optical pump-probe measurement which uses a single optical excitation pulse we observe only weak precession of the magnetization vector. We attribute this signal to thermal strain within the multilayer which persists well after thermal equilibration of the excited film. In contrast, after optical TG excitation we observe a strong coupling of the acoustic mode to the ferromagnetic resonance. We also observe parametric harmonic frequency generation due to the modulation of the transient anisotropy by the acoustic strain wave. Our model calculations qualitatively reproduce the magnetization dynamics in both experiments.

* Electronic address: peter.gaal@ikz-berlin.de

[1] E. Beaurepaire, J.-C. Merle, A. Daunois, and J.-Y. Bigot, Phys. Rev. Lett. **76**, 4250 (1996), URL https://link.aps.org/doi/10.1103/PhysRevLett.76.4250.

[2] I. Tudosa, C. Stamm, A. B. Kashuba, F. King, H. C. Siegmann, J. Stöhr, G. Ju, B. Lu, and D. Weller, Nature **428**, 831 (2004), ISSN 1476-4687, URL https://doi.org/10.1038/nature02438.

[3] S. Pathak, C. Youm, and J. Hong, Scientific Reports **10**, 2799 (2020), ISSN 2045-2322, URL https://doi.org/10.1038/s41598-020-59533-y.

[4] O. Kovalenko, T. Pezeril, and V. V. Temnov, Phys. Rev. Lett. **110**, 266602 (2013), URL https://link.aps.org/doi/10.1103/PhysRevLett.110.266602.

[5] A. V. Scherbakov, A. S. Salasyuk, A. V. Akimov, X. Liu, M. Bombeck, C. Brüggemann, D. R. Yakovlev, V. F. Sapega, J. K. Furdyna, and M. Bayer, Phys. Rev. Lett. **105**, 117204 (2010), URL https://link.aps.org/doi/10.1103/PhysRevLett.105.117204.

[6] J. Janusonis, T. Jansma, C. L. Chang, Q. Liu, A. Gatilova, A. M. Lomonosov, V. Shalagatskyi, T. Pezeril, V. V. Temnov, and R. Tobey, Scientific Reports **6**, 29143 (2016).

[7] J. Janušonis, C. L. Chang, T. Jansma, A. Gatilova, V. S. Vlasov, A. M. Lomonosov, V. V. Temnov, and R. I. Tobey, Phys. Rev. B **94**, 024415 (2016), URL http://link.aps.org/doi/10.1103/PhysRevB.94.024415.

[8] M. Herzog, A. Bojahr, J. Goldshteyn, W. Leitenberger, I. Vrejoiu, D. Khakhulin, M. Wulff, R. Shayduk, P. Gaal, and M. Bargheer, Appl. Phys. Lett. **100**, 094101 (2012), URL http://link.aip.org/link/?APL/100/094101/1.

[9] R. Shayduk, M. Herzog, A. Bojahr, D. Schick, P. Gaal, W. Leitenberger, H. Navirian, M. Sander, J. Goldshteyn, I. Vrejoiu, et al., Phys. Rev. B **87**, 184301 (2013), URL http://link.aps.org/doi/10.1103/PhysRevB.87.184301.

[10] J.-E. Pudell, M. Sander, R. Bauer, M. Bargheer, M. Herzog, and P. Gaal, Phys. Rev. Applied **12**, 024036 (2019), URL https://link.aps.org/doi/10.1103/PhysRevApplied.12.024036.

[11] L. Baselgia, M. Warden, F. Waldner, S. L. Hutton, J. E. Drumheller, Y. Q. He, P. E. Wigen, and M. Maryško, Phys. Rev. B **38**, 2237 (1988), URL https://link.aps.org/doi/10.1103/PhysRevB.38.2237.

[12] M. Wellhfer, M. Weienborn, R. Anton, S. Ptter, and H. Oepen, Journal of Magnetism and Magnetic Materials **292**, 345 (2005).

[13] H. Stillrich, C. Menk, R. Frmter, and H. P. Oepen, Journal of Magnetism and Magnetic Materials **322**, 1353 (2010), ISSN 0304-8853, proceedings of the Joint European Magnetic Symposia, URL http://www.sciencedirect.com/

science/article/pii/S0304885309009366.
[14] G. Winkler, A. Philippi-Kobs, A. Chuvilin, D. Lott, A. Schreyer, and H. Oepen, Journal of Applied Physics **117** (2015).
[15] D. Sander, Reports on Progress in Physics **62**, 809 (1999), URL http://stacks.iop.org/0034-4885/62/i=5/a=204.
[16] M. Sander, M. Herzog, J. E. Pudell, M. Bargheer, N. Weinkauf, M. Pedersen, G. Newby, J. Sellmann, J. Schwarzkopf, V. Besse, et al., Physical Review Letters **119**, 075901 (2017), ISSN 0031-9007, URL https://link.aps.org/doi/10.1103/PhysRevLett.119.075901.
[17] M. Sander, J.-E. Pudell, M. Herzog, M. Bargheer, R. Bauer, V. Besse, V. Temnov, and P. Gaal, Applied Physics Letters **111**, 261903 (2017), ISSN 0003-6951, URL http://aip.scitation.org/doi/10.1063/1.5004522.
[18] M. D. Kuz'min, Phys. Rev. Lett. **94**, 107204 (2005).
[19] N. Akulov, Z. Phys. **100**, 197 (1936).
[20] E. R. Callen and H. B. Callen, Phys. Rev. **129**, 578 (1963), URL https://link.aps.org/doi/10.1103/PhysRev.129.578.
[21] D. Schick, A. Bojahr, M. Herzog, R. Shayduk, C. von Korff Schmising, and M. Bargheer, Computer Physics Communications **185**, 651 (2014), ISSN 0010-4655, URL https://www.sciencedirect.com/science/article/pii/S0010465513003378?via{\%}3Dihub.
[22] B. L. K. S. I. Anisimov and T. L. Perelman, Sov. Phys. JETP **39**, 375 (1974).
[23] D. Schick, A. Bojahr, M. Herzog, C. von Korff Schmising, R. Shayduk, and M. Bargheer, Comput. Phys. Commun. **185**, 651 (2014), ISSN 0010-4655, URL http://www.sciencedirect.com/science/article/pii/S0010465513003378.
[24] C. von Korff Schmising, M. Giovannella, D. Weder, S. Schaffert, J. L. Webb, and S. Eisebitt, New Journal of Physics **17**, 033047 (2015), URL http://stacks.iop.org/1367-2630/17/i=3/a=033047.
[25] C. Thomsen, H. T. Grahn, H. J. Maris, and J. Tauc, Phys. Rev. B **34**, 4129 (1986), URL https://link.aps.org/doi/10.1103/PhysRevB.34.4129.
[26] G. L. Eesley, B. M. Clemens, and C. A. Paddock, Applied Physics Letters **50**, 717 (1987), https://doi.org/10.1063/1.98077, URL https://doi.org/10.1063/1.98077.
[27] P. Ruello and V. E. Gusev, Ultrasonics **56**, 21 (2015), ISSN 0041-624X, URL http://www.sciencedirect.com/science/article/pii/S0041624X1400153X.
[28] M. Sander, R. Bauer, V. Kabanova, M. Levantino, M. Wulff, D. Pfuetzenreuter, J. Schwarzkopf, and P. Gaal, Journal of Synchrotron Radiation **26**, 1253 (2019), URL https://doi.org/10.1107/S1600577519005356.
[29] R. Shayduk, H. Navirian, W. Leitenberger, J. Goldshteyn, I. Vrejoiu, M. Weinelt, P. Gaal, M. Herzog, C. von Korff Schmising, and M. Bargheer, New Journal of Physics **13**, 093032 (2011), URL https://doi.org/10.1088%2F1367-2630%2F13%2F9%2F093032.
[30] H. A. Navirian, D. Schick, P. Gaal, W. Leitenberger, R. Shayduk, and M. Bargheer, Applied Physics Letters **104**, 021906 (2014), https://doi.org/10.1063/1.4861873, URL https://doi.org/10.1063/1.4861873.
[31] M. Farle, Reports on Progress in Physics **61**, 755 (1998), URL https://doi.org/10.1088%2F0034-4885%2F61%2F7%2F001.
[32] R. C. O'Handley, Modern magnetic materials : principles and applications (Wiley, New York, 2000), ISBN 0471155667.
[33] C. L. Chang, A. M. Lomonosov, J. Janusonis, V. S. Vlasov, V. V. Temnov, and R. I. Tobey, Phys. Rev. B **95**, 060409 (2017), URL https://link.aps.org/doi/10.1103/PhysRevB.95.060409.
[34] H. Stillrich, C. Menk, R. Fromter, and H. Oepen, Journal of Applied Physics **105**, 07C308 (2009).
[35] J. Wagner (2019).
[36] M. van Kampen, C. Jozsa, J. T. Kohlhepp, P. LeClair, L. Lagae, W. J. M. de Jonge, and B. Koopmans, Phys. Rev. Lett. **88**, 227201 (2002), URL https://link.aps.org/doi/10.1103/PhysRevLett.88.227201.
[37] P. Gaal, D. Schick, M. Herzog, A. Bojahr, R. Shayduk, J. Goldshteyn, H. A. Navirian, W. Leitenberger, I. Vrejoiu, D. Khakhulin, et al., Appl. Phys. Lett. **101**, 243106 (2012).
[38] M. Sander, A. Koc, C. T. Kwamen, H. Michaels, A. v. Reppert, J. Pudell, F. Zamponi, M. Bargheer, J. Sellmann, J. Schwarzkopf, et al., Journal of Applied Physics **120**, 193101 (2016), URL http://scitation.aip.org/content/aip/journal/jap/120/19/10.1063/1.4967835.
[39] T. L. Linnik, A. V. Scherbakov, D. R. Yakovlev, X. Liu, J. K. Furdyna, and M. Bayer, Phys. Rev. B **84**, 214432 (2011), URL https://link.aps.org/doi/10.1103/PhysRevB.84.214432.

Acknowledgments

I'm extremely grateful to Dr. Peter Gaal for supervision of my dissertation, the chance to be a part of the work group and invaluable experience I gained on this journey. This achievement would not be possible without his support and patience that cannot be underestimated.
I'm deeply indebted to Prof. Dr. Hans Peter Oepen for advice, opportunities and support he provided to me, all the way starting from my bachelor studies up to the promotion.
I would like to thank Prof. Dr. Nils Huse for supervision of my dissertation and access to crucial resources and infrastructure.
Special thanks to Prof. Dr. Robert Blick for his willingness to evaluate my dissertation.
Many thanks to all group members for an interesting time together and everyone who participated in beamline experiments.

Eidesstattliche Versicherung / Declaration on oath

Hiermit erkläre ich an Eides statt, dass ich die vorliegende Dissertationsschrift selbst verfasst und keine anderen als die angegebenen Quellen und Hilfsmittel benutzt habe.

I hereby declare upon oath that I have written the present dissertation independently and have not used further resources and aids than those stated.

Hamburg, den